Surface Interaction Effects on Exciton Photophysics in Two Dimensional Semiconductors

Wenjin Zhang

Abstract

Surface Interaction Effects on Exciton Photophysics in Two Dimensional Semiconductors

By

Wenjin Zhang

Advisor: Professor Kazunari Matsuda

Since the first isolation of a single-atom-thick carbon sheet, graphene, by mechanical exfoliation in 2004, layered materials such as transition metal dichalcogenides (TMDs) and other two dimensional (2D) materials have attracted much attention because of their potential usefulness in optical and electronic devices at reduced dimension. Atomically thin TMDs specifically, with the chemical composition of MX_2, where M is the transition metals (either Mo or W typically) and X is the chalcogens (S, Se, or Te), are regarded as a new class of 2D materials beyond graphene. They illustrate attractive electronic and optical properties originating from the thickness dependent electronic band structure. Different from their bulk counterparts, monolayer (1L) TMDs are direct gap semiconductors that show unique spin-valley coupling properties and strong Coulomb interactions. Hence, providing a new platform for future fast and energy-saving optoelectronic technologies.

The optical properties of atomically thin TMDs are dominated by bound electron-hole pairs (excitons) and/or three body bound state of electrons and holes, which are known also as charged excitons or trions. The strong Coulomb interaction and reduced

screening effect in atomically thin TMDs enable these excitons and trions to remain stable even at room temperature. Meanwhile, due to the large specific surface area, the excitonic properties of atomically thin TMDs are easily affected by various surface interaction effects. These include interface interactions with other materials or adsorbed molecules, and carrier modulation by electrical or chemical processing, which takes place in both wet and dry environments. While oxygen and water molecules are usually the main causes affecting the usefulness of such ultrathin TMD sheets in realistic condition full of air and humidity, surface adsorbed organic molecules or integrated materials may also play a critical role in modifying their physical properties.

In this thesis, by using two typical members of the TMD family, namely MoS_2 and WSe_2, I first describe the studies conducted on the optical properties of their monolayers in aqueous solution. A comparison was made between their photoluminescence (PL) responses observed in distilled water and ambient air to understand the effects of O_2 and H_2O. Meanwhile, their PL signals was monitored under different pH conditions. This offers not only an insight into the underlying mechanism to the O_2/H_2O and pH effects, but also an opportunity to utilize/control the PL properties of 1L TMDs in various conditions. In addition, the photostability of these two materials in ambient air and aqueous solutions was also studied. A distinct difference was found for MoS_2 and WSe_2 due to the effects of band alignment between 1L TMDs and H_2O redox potential.

Motivated by these findings, I explore further on the surface interaction effects on PL polarization of 1L TMDs in dry condition. This is crucial as it represent a significant feature for the application of these materials in future optoelectronics, called valleytronics. In this case, 1L MoS_2 was treated with *p*-type chemical dopant F_4TCNQ and the

polarization dependent PL property was investigated. A considerable increase of the exciton attribution was observed after treatment, revealing the electron extraction from the naturally *n*-doped 1L MoS_2 by the dopant molecules. However, despite the lowered electron density, an increased trions contribution was recorded when the sample was chilled to a cryogenic temperature. This increment is attributed to the extension of trion nonradiative lifetime based on the time-resolved PL measurements. The treated sample retained a high degree of polarization of more than 0.75 even with much improved PL intensity. An extremely long valley lifetime with an order of at least nanosecond was also deduced. These are very promising for the valleytronic application.

These systematic studies of surface interaction effects on the PL, photostability and valley polarization properties in this thesis provide us a useful insight into not only the surface electrochemical reaction of 1L TMDs in different environments, but also their impact on the exciton photophysical properties of 1L TMDs. The mechanism revealed sheds much lights on the development of new electronic, optoelectronic and valleytronic devices, facilitating the application of TMDs in a diverse range of next generation fast and energy saving information processing fields.

Acknowledgements

Soon, my PhD study will come to an end. I would like to take this opportunity to express my sincere appreciation to all those who have given me their unreserved support throughout these years.

First and foremost, I would like to thank Professor Kazunari Matsuda, for accepting me as a member to his lab. He has been helpful not only in the academic research, but also my daily life. His experience and background in optical physics have benefited me a lot. Thanks to his invaluable advice and comments, my studies can be constantly improved to a better state of completeness.

I am truly indebted to my direct mentor, Associate Professor Yuhei Miyauchi for his supervision along this period of doctoral study. I have learned a lot from him not only on the experimental and writing skills, but also his attitude and passion towards science. He is always encouraging and supportive, giving me courage to proceed further at times of difficulty.

Besides, I am feeling grateful to Assistant Professor Keisuke Shinokita and Taishi Nishihara, who have been sharing their knowledge in physics with me. I am thankful also to Dr. Shinichiro Mouri, who is now an assistant professor in Ritsumeikan University, for teaching me the fundamental experimental skills and the guidance given when I first entered this laboratory.

I would like to express my gratitude to the former lab members, including Dr. Feijiu Wang, Kazushi Hiraoka, Dr. Sandhaya Koirala, Dr. Dezhi Tan, Dr. Hong En Lim and Dr.

Nur Baizura Mohamed who had been sharing me their experience and knowledge in research and daily life. Thank all the former members, Shun Aota, Takashi Nakamura, Shohei Yanagawa, Yusuke Hasegawa, Takao Yamaoka, Saki Okudaira, Kengo Hachiya, Ken Kiyama, Dr. Takashi Someya, Dr. Fengjiu Yang, and the current members, Dr. Akira Takakura, Xiaofan Wang, Masafumi Shimasaki, Yan Zhang, Kenya Tanaka, Shotaro Yano and Mikio Kobayashi for their companionship, help and cooperation. Thank all the intern students, Dr. Amr Hessein Hassan, Alex Hwang and Sahil Patel. Their presence was short but meaningful. Thank all members from assistant Professor Tatsuya Hinoki's group. Not to forget, our secretary, Shiori Fujiwara for her great assistance in all these years. Thank all my friends who have helped me in any possible ways!

Special thanks to everyone who has had taken a great care of me when I was sick. Thank you Katsuhiro Watanabe, my Japanese language teacher, for helping me so much not only in language study itself, but also giving me a great exposure to Japanese culture!

Finally, I would like to thank my parents, sisters and all other family members for their never ending support and love! Last but not least, thank you He, my beloved fiancée, for the wonderful moments that we have spent together and every sweet little thing that you have done for me! My life is not complete until the day that I found you.

Wenjin Zhang

2019 in Uji, Kyoto

Dedication

To my late grandmother.

Table of Contents

List of Figures

Chapter 1. Introduction

1.1. Background

When the size of a material is significantly reduced, particles or quasi particles in the material become confined in a small range. This is when the quantum confinement effect takes place predominating the properties of the material, resulting in the emergence of new physical features unavailable in bulk. For that, continuous efforts have been spent attempting to reduce the dimension of the material. In the early 1980s, zero dimensional (0D) quantum dot was found after the realization of near two dimensional (2D) thin quantum well. Shortly afterwards, 0D fullerenes and 1D carbon nanotubes, the nanostructures of carbon, were discovered in 1985 and 1991, respectively. The success had triggered a tremendous interest among the material scientists, chemists and physicists to look for atomically thin, low dimensional materials.[1–3] At that time, atomically thin 2D material was still a theory prediction as it was considered thermodynamically unstable.[4–7]

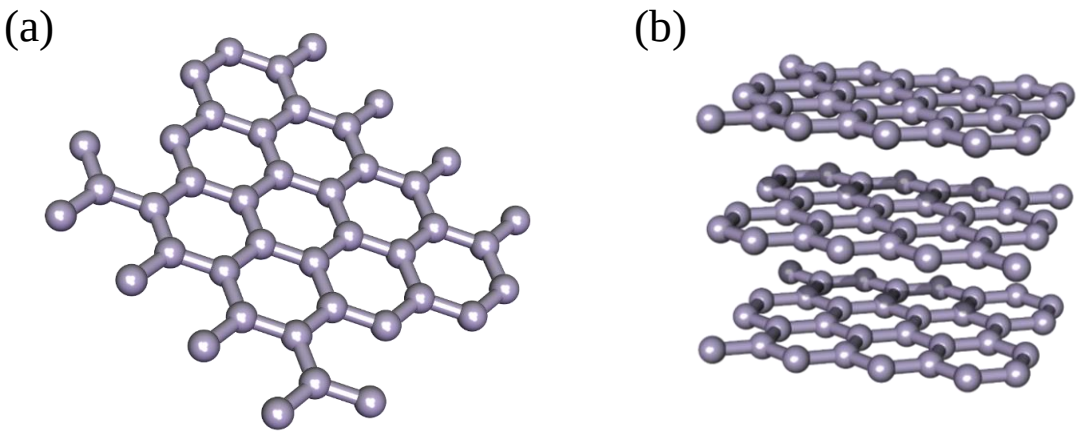

Figure 1.1 Structures of graphene and graphite.

It was not until 2004, the group led by Novoselov and Geim had first succeeded in peeling a single-layer carbon sheet from bulk graphite crystal (**Figure 1.1**) using a simple mechanical exfoliation method with Scotch tape.[8] Graphite, being a layered structure material, is composed of stacked layers of carbon sheets bonded through weak van der Waals force. When a single-layer sheet is picked up as an isolated layer, it generates a true 2D material that shows distinctive properties different from bulk due to the strong quantum effect.[9,10] This isolated carbon sheet of an atom thick is known as graphene. It has a 2D hexagonal lattice or the so-called honeycomb structure with sp^2 orbitals.[3,11]

Graphene shows a zero gap semimetallic property with massless Dirac valleys located at K and K´ corners of the Brillouin zone as shown in **Figure 1.2**.[11–13] Although it exhibits an extremely fast ballistic electronic transport with a high mobility of ~10^4 cm^2 V^{-1} s^{-1},[14,15] the absence of a finite electronic gap has limited its realistic application in electronics and optoelectronics. For example, the low on/off current ratio ($< 10^2$) of graphene based transistor is unfavorable for logic circuits and optical or optoelectronic devices usually require semiconductors.[14,16,17] Meanwhile, a sophisticated conceptual design for future electronics has been recently proposed. It is called valley-/spintronics, which makes use of the valley degree of freedom for electrons and spins generation, producing carriers that aid high speed information processing at great efficiency with low energy consumption.[18,19] However, it is difficult to realize this new concept in experiment for graphene because symmetry breaking of two carbon atoms in a unit cell for its monolayer (1L) or bilayer (2L) is hardly achieved with a simple device configuration.

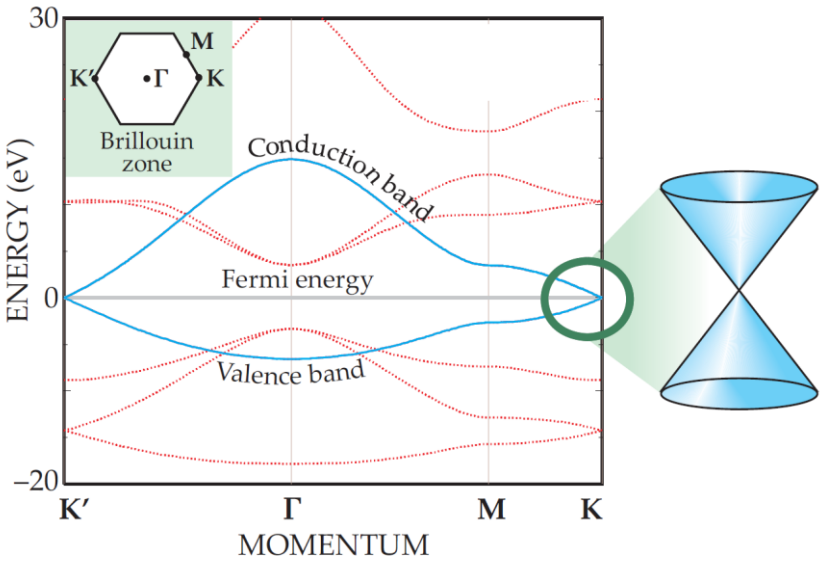

Figure 1.2 Electronic band structure of graphene. (Reprinted with the permission from Ref.[11]. © 2010 AIP)

Owing to the rising demand for highly efficient materials with low energy consumption in this era of increasing energy resource shortages, the progress in graphene research has stimulated a substantial effort to explore other layered materials for their potentials in next generation devices and energy related field.[8,20–25] For example, hexagonal boron nitride (*h*BN) is an insulator with a large band gap,[26,27] whereas atomically thin transition metal dichalcogenides (TMDs) have sizeable band gaps with thickness dependent band structures.[28,29] Black phosphorus (BP), on the other hand, has an in-plane anisotropy and demonstrates strong infrared photoresponsivity.[30,31] A diverse variety of members in the 2D family ranging from insulator, semiconductors, metals, semimetals to superconductors are shown in **Table 1-1**.[32–34]

Among these newly emerged 2D materials, TMDs represent a typical class, which displays layer-dependent electronic band structure.[28] They consist of MX_2, where *M* is the

transition metal atoms (either Mo or W typically); and *X* is the chalcogen atoms (S, Se, or Te), respectively. When thinned to a monolayer (1L) thick, they transform from an indirect gap semiconductor in bulk to a direct one. These 1L TMDs show rich electronic gaps from visible (MoS_2 or WSe_2) to near infrared ($MoTe_2$) regions, with tunable electronic and optical features by chemical and physical methods. They are, therefore, considered one of the promising materials for future applications in electronic and optoelectronic devices. In addition, the intrinsically broken spatial inversion symmetry in 1*H* 1L TMDs allows selective excitation of the inequivalent pairs of degenerated valleys in momentum space.[35,36] This unique property qualifies them as an excellent candidate for the valleytronic application in next generation (quantum) information processing technology, which is expected to enable a ultrafast operation with lower energy consumption than current devices.[37–40]

Table 1-1 Some typical members in 2D layered material.

2D Layered material	Insulator	hBN
	Semiconductor	TMDS (MoS_2,ReS_2,WSe_2, etc.), BP, III-VI group (InSe, GaS), etc.
	Metal	Mxenes (V_2C, Mo_2N, Cr_2TiC_2), VO_2, VS_2, etc.
	Semimetal	Graphene, Ge, Sn, etc.
	Superconductor	$NbSe_2$, $RbSe_2$, etc.

1.2. Motivation

As mentioned above, TMDs possess useful optical and electronic properties suitable for various conventional and future applications. These unique properties can be easily manipulated by different means, such as applying substrate strain,[41,42] magnetic field,[43–45] electrostatic gating[46,47] and chemical treatment.[48,49] To date, 1L TMDs have been used

to fabricate a diverse range of devices including phototransistors,[50–56] photodetectors,[57–59] light-emitting devices,[47,60] light modulators,[61] and solar cells.[62–64] Devices based on 2D materials are used in various environments such as ambient air, solvent, aqueous solutions or in combination with other materials, which can be divided into dry and wet (liquid) conditions mainly. Due to the large specific surface area of 1L TMDs, their physical properties can be easily modified. It is thus of utmost importance to understand the effects of their surface interactions with other materials or molecules, as this may give an important clue benefiting not only material selection, but also device fabrication and applications of TMDs.

1.3. Thesis outline

In this thesis, I systemically studied the surface interaction effects on the optical and photostability properties of 1L TMDs in ambient air and liquid (aqueous solutions), which resemble the typical environments for device operation. In addition, effect of the molecular dopant to the valley polarization property of trions in 1L TMD was also investigated in dry condition at low temperature, aiming to understand the dry surface effect on valleytronic property.

This chapter will be followed by Chapter 2, in which the fundamental properties of solids and TMDs are briefly introduced. Experimental methods used and the setups developed are described in Chapter 3. In Chapter 4, the optical properties of 1L TMDs (MoS_2 and WSe_2) in ambient air and aqueous solutions are studied. The results are illustrated showing differences between these conditions and the underlying mechanisms are explained. In Chapter 5, the stability of MoS_2 and WSe_2 in these conditions are studied. The differences observed between MoS_2 and WSe_2 are discussed, giving an insight into

the device application. In Chapter 6, the chemical dopant effect on the PL and trion valley polarization properties of 1L MoS_2 in dry condition at 15 K are studied, and the mechanism of the observed phenomena is explained. As a summary, the conclusion and outlook for future research work based on the studies in this thesis are provided in Chapter 7.

Chapter 2. Fundamental properties of atomically thin layered materials

Atomically thin TMDs, with thickness of ~0.5–0.7 nm, show unique physical properties dissimilar to their bulk 3D crystals due to the quantum confinement effect. In this chapter, the fundamental physics of solids will be introduced and the optical and electronic properties of the TMDs sheets will be briefly explained.

2.1. Basic optical properties of solids

As this thesis focus mainly on the various surface interaction effects on the optical properties of TMDs, related fundamentals on the optical behaviors of solids will first be introduced.

2.1.1. Atom, crystal structure and Brillouin zone

An atom is the smallest particle of an element that has the properties of the element. It consists of a nucleus and negatively charged electrons which follow a random pattern within defined energy shells from the Niels Bohr's theory. In bulk, atoms are arranged in a periodic 3D pattern to form a crystal structure.

Lattice and Wigner-Seitz unit cell

A lattice obtained from three primitive translation vectors $\overrightarrow{a_1}$, $\overrightarrow{a_2}$, $\overrightarrow{a_3}$ is an infinite array of points (atoms). Any points in the lattice can be given by $\vec{n}= n_1\overrightarrow{a_1}+n_2\overrightarrow{a_2}+n_3\overrightarrow{a_3}$. A point group is formed by a set of translations of lattice. There are 5 different types of 2D lattices (square, hexagonal, oblique, rectangular primitive, and rectangular centered) and 14 different types of 3D lattices (cubic, orthorhombic, hexagonal and *etc.*). From the

lattice point (0, 0, 0), a set of translation vectors can be drawn to neighboring lattice points. Some planes that are perpendicular bisectors of these translation vectors can be drawn. The interior of these intersection planes is called the Wigner-Seitz unit cell as shown in **Figure 2.1.**[65]

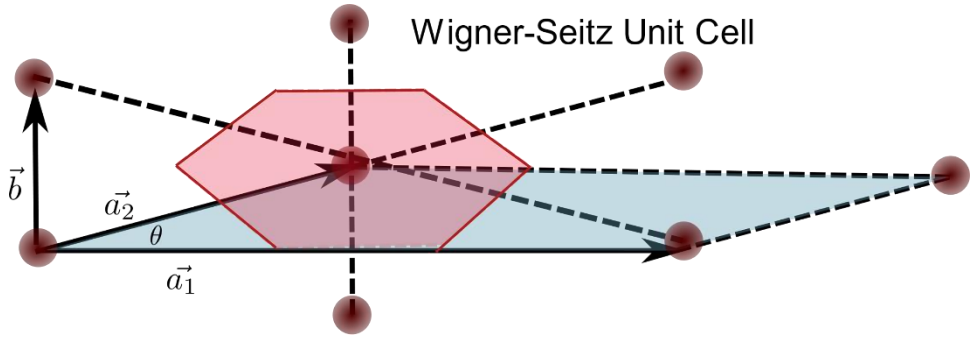

Figure 2.1 Schematic of a Wigner-Seitz cell of a two dimensional centered rectangular lattice.

Common crystal structures

In a crystal, atoms are located at specific lattice points forming the different types of conformation such as cubic, hexagonal, and graphite structures. **Figure 2.2** shows the simple cubic, simple hexagonal and graphite structures.[65]

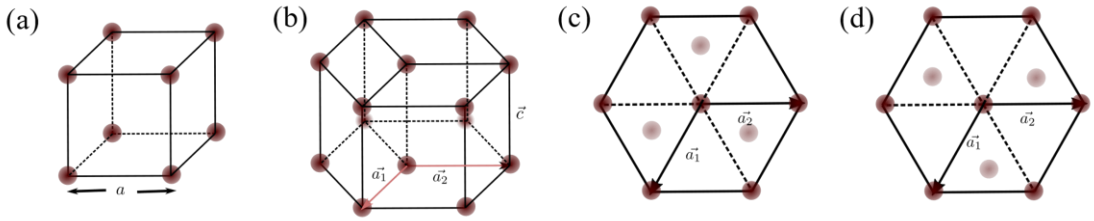

Figure 2.2 Crystallographic unit cell of a simple cubic crystal (a), simple hexagonal crystal (b) and graphite structure with a stacking A (c) and B layers (d)

Reciprocal lattice

If the vectors $\overrightarrow{b_1}$, $\overrightarrow{b_2}$, $\overrightarrow{b_3}$ satisfy

$$\overrightarrow{a_i} \cdot \overrightarrow{b_j} = 2\pi\delta_{ij} \qquad 2.1$$

where $\overrightarrow{a_i}$ is primitive transition vectors, and $\delta_{ij} = 0$ if i ≠ j; $\delta_{ij} = 1$ if i = j. The lattice formed by the primitive translation vectors $\overrightarrow{b_1}$, $\overrightarrow{b_2}$, $\overrightarrow{b_3}$ is called reciprocal lattice, and reciprocal lattice vector is $\vec{G} = h_1\overrightarrow{b_1} + h_2\overrightarrow{b_2} + h_3\overrightarrow{b_3}$.

Brillouin zone

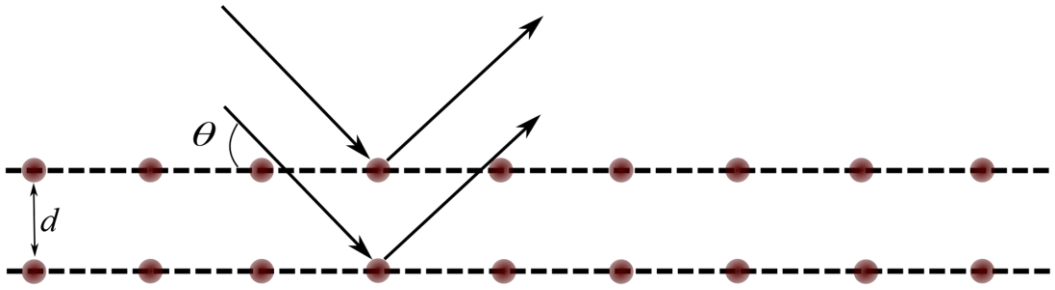

Figure 2.3 Reflection of X-rays with an indecent angle of θ by a set of crystal planes separated by a distance *d*.

In a reciprocal lattice, the Wigner-Seitz cell is called Brillouin zone, which is the interior of perpendicular bisector planes of the reciprocal lattice vectors. The central cell is called first Brillouin zone. The Bloch waves (which will be described further in Section 2.1.2) with a wave vector $\overrightarrow{k}$ that terminate on any of these planes satisfy Bragg's diffraction condition, where $2d\sin\theta = n\lambda$ as shown in **Figure 2.3**.[65] Here, λ is the

incident wavelength and *n* is the integer value. If $\theta = \frac{\pi}{2}$, $d = a$ (lattice constant), $k = \frac{n\pi}{a}$, the region of wave vector *k* between $-\frac{\pi}{a}$ and $+\frac{\pi}{a}$ is the first Brillouin zone, which has the smallest volume enclosed by the planes. Brillouin zone is a basic essential part in analyzing the electronic energy band structure of crystals, which dictates the optical properties of solids. The first Brillouin zone of a hexagonal lattice structure is shown in **Figure 2.4**.[66]

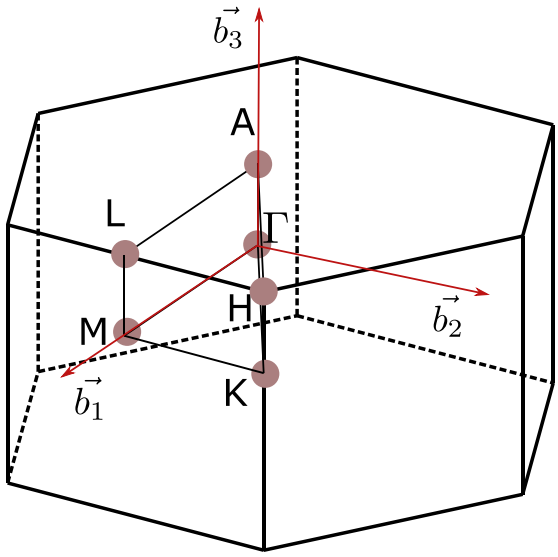

Figure 2.4 Brillouin zone of Hexagonal lattice.

2.1.2. Electronic band structure and density of state

Electronic band, *k* space and momentum space

In free atom, electrons are located in discrete quantum energy levels. Meanwhile, atoms in a crystal are packed closely according to the different types of lattice structures and the interatomic separation is approximately equal to the atoms' size. The outer orbitals of these atoms thus overlap and interact strongly with each other, converting the

discrete energy levels into broad bands as shown in **Figure 2.5**.[67] The state of a single electron within a periodic crystalline potential $V(\vec{r}) = V(\vec{r} + \vec{R})$ can be stated using the wave function via the Bloch's theorem:

$$\varphi(\vec{r}) = \mathrm{e}^{\mathrm{i}kr} u(\vec{r}) \qquad 2.2$$

where $u(\vec{r} + \vec{R}) = u(\vec{r})$, $u(\vec{r})$ is the envelope function that is dependent on the electronic band which retains some of the atomic character. From the Schrödinger equation of a single electron in a periodic crystalline potential:

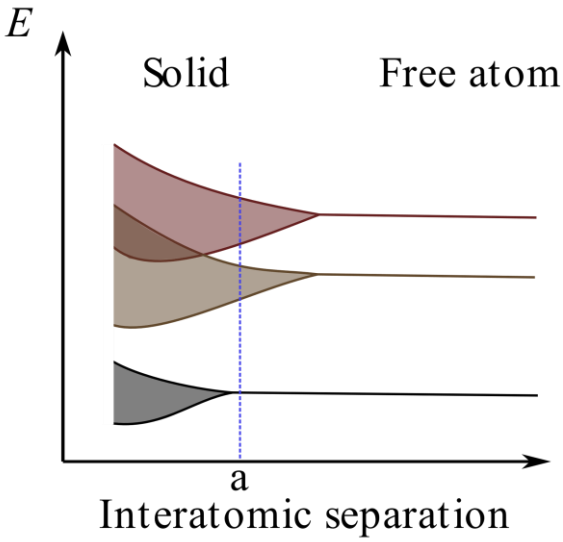

Figure 2.5 Schematic diagram showing the transformation of discrete energy levels in a free atom into the electronic bands of a solid.

$$\hat{H}\varphi = E\varphi \qquad 2.3$$

$$\left[-\frac{\hbar^2}{2m}\nabla^2 + V(r)\right]\varphi_k(r) = E(k)\varphi_k(r) \qquad 2.4$$

an infinite solution can be obtained:

$$E_1(k), E_2(k), E_3(k), E_4(k), \ldots..$$

$$\varphi_{1k}(r), \varphi_{2k}(r), \varphi_{3k}(r), \varphi_{4k}(r) \ldots.$$

with a set of *k* values, and the continuous $E_n(k)$ formed a band which is called energy band. Here, Hamiltonian $\widehat{H}$ is composed of two parts, namely the kinetic energy, $E = \frac{\hbar^2 k^2}{2m}$ and potential energy, *U*. The position vectors $\vec{r}$ correspond to the wave vectors $\vec{k}$, which are similar with position space (real space or coordinate space). A set of these wave vectors $\vec{k}$, is called the *k* space. Similarly, momentum space is another conceptual entity that has a set of momentum vectors $\vec{p}$ in a physical system. **Figure 2.6** shows the electronic band of free electrons and bulk MoS_2 in a *k* space.[68]

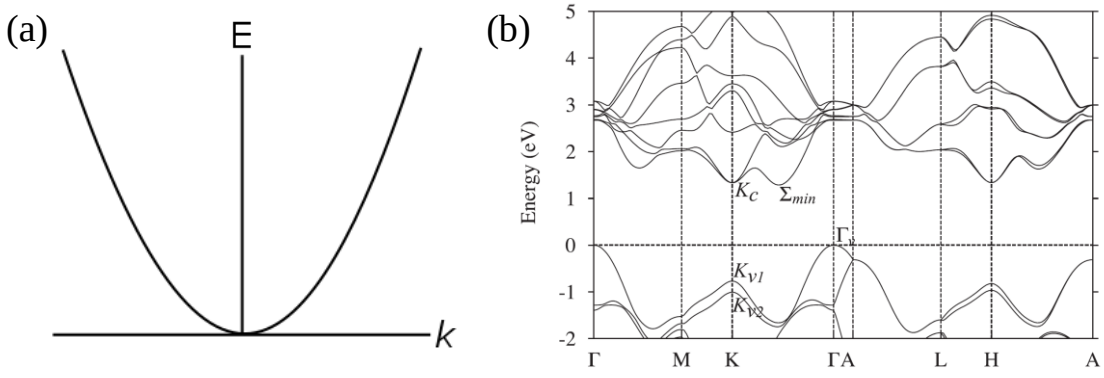

Figure 2.6 A plot of energy versus wave vector for free electrons, known also as *E*-*k* diagram (a). Electronic band diagram of bulk MoS_2 (b). (Figure b is reprinted with the permission from Ref.[68]. © 2012 APS.)

Density of state

Within an energy range in a continuous band, the number of states directly affects the absorption and emission properties of solids. The density of state, *g*(*E*) means: energy

from $E \rightarrow (E + dE)$, the total state is $g(E)dE$. $g(E)$ is usually obtained from $g(k)$ using the following relationship:

$$g(E) = g(k)\frac{dk}{dE} \qquad 2.5$$

, where $g(k)$ is the density of states in momentum space. It can be calculated from the E-k relationship stated above and it is strongly size dependent as described later in section 2.1.4.

2.1.3. Energy gap, metal, semiconductor and insulator

Energy gap

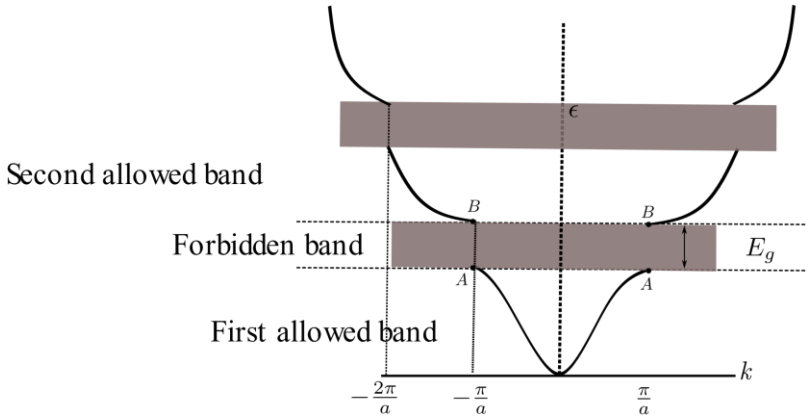

Figure 2.7 A plot of energy, E versus wave vector, k of a monatomic linear lattice. Energy gap, E_g is associated with the first Bragg reflection in the first Brillouin zone. Note: Other gaps exist at higher energies at $\pm n\pi/a$.

As mentioned above, waves are Bragg reflected at the edge of the Brillouin zone. Standing waves are thus formed within the Brillouin zone. The incident and Bragg reflected standing waves are described as:[69]

$$\psi(+) = \exp(i\pi x/a) + \exp(-i\pi x/a) = 2\cos(\pi x/a) \quad 2.6$$

$$\psi(-) = \exp(i\pi x/a) - \exp(-i\pi x/a) = 2i\sin(\pi x/a) \quad 2.7$$

The two standing waves pile up at different regions with separate values of potential energy, and hence the origin of the energy gap. A typical energy-wave vector diagram of a monatomic linear lattice with the lattice constant, a is shown in **Figure 2.7**.[69] The energy gap (band gap) is determined the Bragg reflection at the Brillouin zone edge where $k = \pm n\pi/a$.

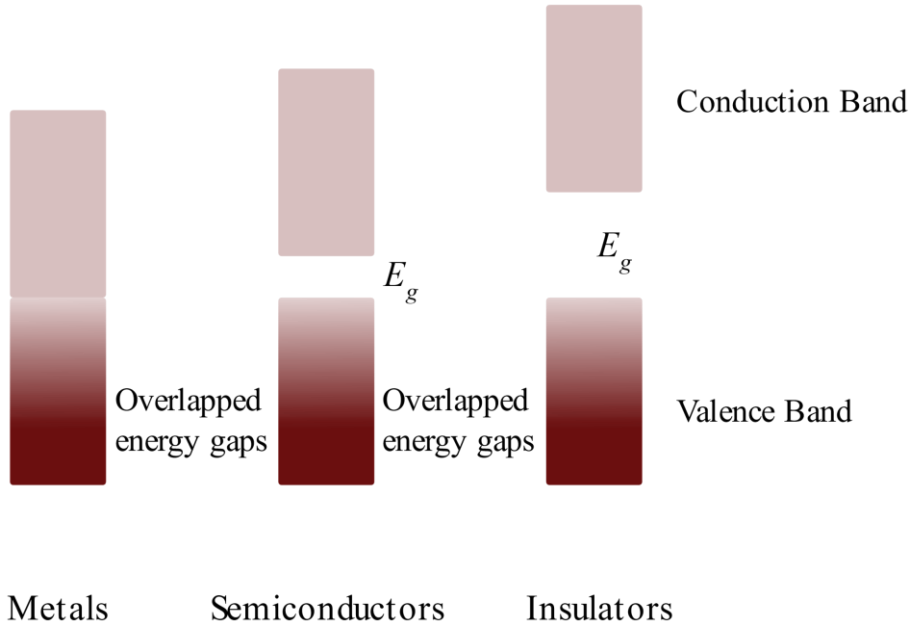

Figure 2.8 Metal, semiconductor and insulator with different bandgaps.

Metal, semiconductor and insulator

As shown in **Figure 2.7**, for a crystal with more than one dimension, there remains some empty states in the lower energy band even when the low energy states of the upper

band has started to be filled according to the Pauli's exclusion principle. The lower filled and higher empty band in solid are known also as the valence and conduction band, respectively. The highest filled orbital at 0 K is called the Fermi level. Overlapping between these bands can be large or nonexistent depending on the magnitude of energy gap,[65,69] by which solids are divided into three main categories shown in **Figure 2.8**.[70]

The energy gap in metal is extremely small or equivalent to zero. There is a huge overlapping between neighboring bands. Semiconductor refers to a material with a small band gap between 0.1 to 2.0 eV typically. Its electron concentration in the conduction band varies with temperature: $n_e = -E_g/2k_BT$, and the conductivity increases with increasing temperature. Insulator generally has a large energy gap of $\geq$ 4 eV between the highest filled and the lowest empty states.

2.1.4. **Heisenberg uncertainty principle and quantum confinement**

Heisenberg Uncertainty Principle

As discussed above, the wave function can be used to describe the wave-like property of electrons. In quantum mechanics understanding, an observed quantity is usually associated with a corresponding operator, which is a rule for building one function from another. For instance, the position operator, $\hat{x}$ is

$$\hat{x} = x \qquad 2.8$$

the momentum operator, $\hat{p}$ is

$$\hat{p} = -i\hbar\frac{\partial}{\partial x} \quad 2.9$$

the energy operator, $\hat{E}$ is

$$\hat{E} = \frac{\hat{p}^2}{2m} + V(\hat{x}) = -\frac{\hbar^2}{2m}\frac{\partial^2}{\partial x^2} + V(x) \quad 2.10$$

Mathematically, the position operator, $\hat{x}$ and momentum operator, $\hat{p}$ do not commute with each other, $[\hat{x}, \hat{p}_x] = i\hbar$, which means that simultaneous precise measurement of both position and momentum are unlikely. This leads to an uncertainty relationship between the position and momentum, which is simplified as:

$$\Delta x \Delta p_x \gg \hbar/2 \quad 2.11$$

It quantifies the way in which a precise measurement of the position increases the uncertainty in the measurement of momentum and *vice versa*.[71]

Quantum Confinement

If a free particle with a mass, *m* is confined within a range of Δx, the confinement energy, $E_{\text{confinement}}$ is:[67]

$$E_{\text{confinement}} = \frac{(\Delta p_x)^2}{2m} \sim \frac{\hbar^2}{2m(\Delta x)^2} \quad 2.12$$

When Δx is very small, $E_{\text{confinement}}$ will be significant, comparable or greater than the thermal motion induced kinetic energy:[67]

$$E_{\text{confinement}} \sim \frac{\hbar^2}{2m(\Delta x)^2} \geq \frac{1}{2}k_{\text{B}}T \quad 2.13$$

$$\Delta x \ll \sqrt{\frac{\hbar^2}{mk_B T}} \qquad 2.14$$

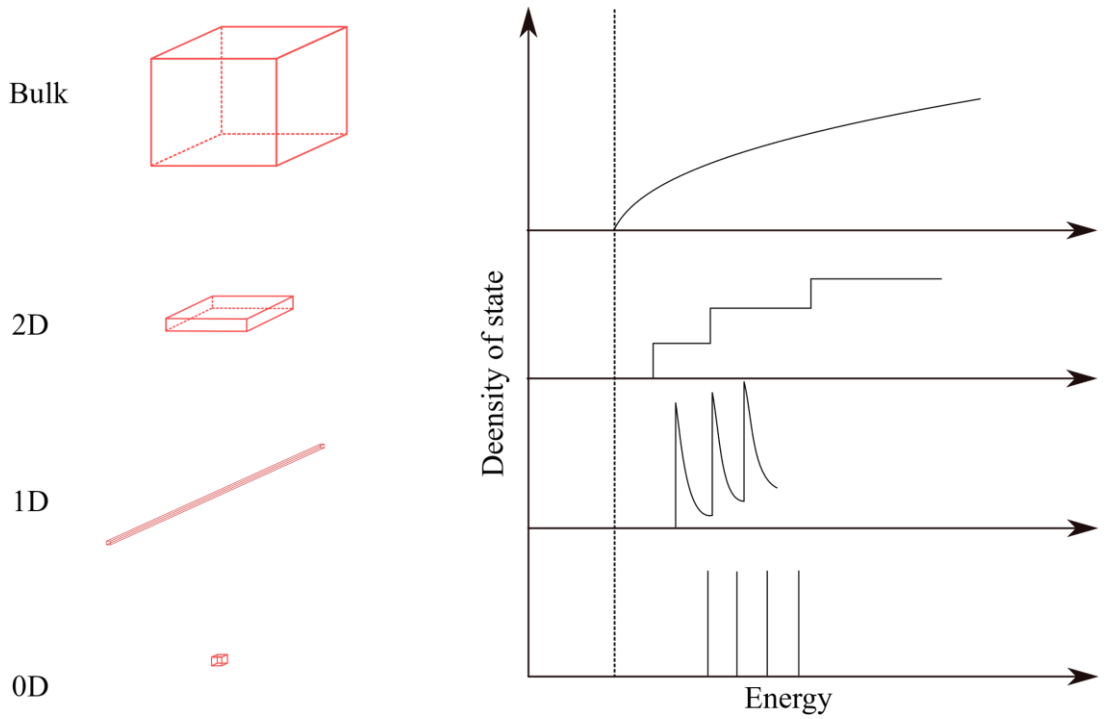

Figure 2.9 The representation of 3D, 2D, 1D and 0D with their corresponding density of states for electrons in the conduction bands.

This means, for an electron with an effective mass $m_e^* \sim 0.1m_0$ (m_0 is the free electron mass) at room temperature, the confinement effect is strong only when $\Delta x \ll 5$ nm. Generally, the quantum confinement effect is defined by the dimensionality of the materials. As shown in **Figure 2.9**, the electron and holes freely move freely in a 3D bulk semiconductor with a 3 degrees of freedom; whereas in the 2D quantum well they can move only within the *xy* direction, thus having 2 degrees of freedom. Similarly, electrons and holes in the quantum wire have 1 degree of freedom, while they are quantized in all directions in quantum dot, giving 0 dimensional property.

The electrons in conduction band have energy above the band gap energy, E_g, and density of state in 3D semiconductors is given as: $g(E) = \frac{1}{2\pi^2}(\frac{2m_e^*}{\hbar^2})^{3/2}\left(E - E_{\mathrm{g}}\right)^{1/2}$; whereas in 2D: $g(E) = \frac{m_e^*}{\pi\hbar^2}$; and 1D: $g(E) = \frac{1}{\hbar\pi}\sqrt{\frac{m_e^*}{2(E-E_{\mathrm{g}})}}$. For 0D quantum dot, the electrons have discrete energies and the delta function is used to describe their density of state, where $g(E) = 2\delta(E - E_{\mathrm{g}})$. The density of states for 3D to 0D structures are shown in **Figure 2.9**.[67]

2.1.5. Interband absorption, emission and quasiparticles

If electrons are provided with sufficient energy, they can be promoted to the unfilled upper band and this is called interband absorption. The opposite process is called interband emission, where these excited electrons relax to the ground state by releasing the extra energy gained either as light emission or in other forms of energy. The excited electron leaves its initial state at the lower band, creating of a hole.[67] Tightly bound electron and hole pair, generated as a consequence of interband absorption, is called exciton. There are several ways by which the interband absorption and emission may take place, but here we will focus mainly on those involving optical means.

Interband Absorption

As shown in **Figure 2.10**, the incident photon with an energy, $E = \hbar\omega > E_{\mathrm{g}}$ is absorbed and the electrons are excited from the initial ground state, E_{i} to the final state, E_{f}:

$$E_{\mathrm{f}} = E_{\mathrm{i}} + \hbar\omega \qquad 2.15$$

Continuous absorption occurs within the band when the photon energy, $E = \hbar\omega > E_g$.

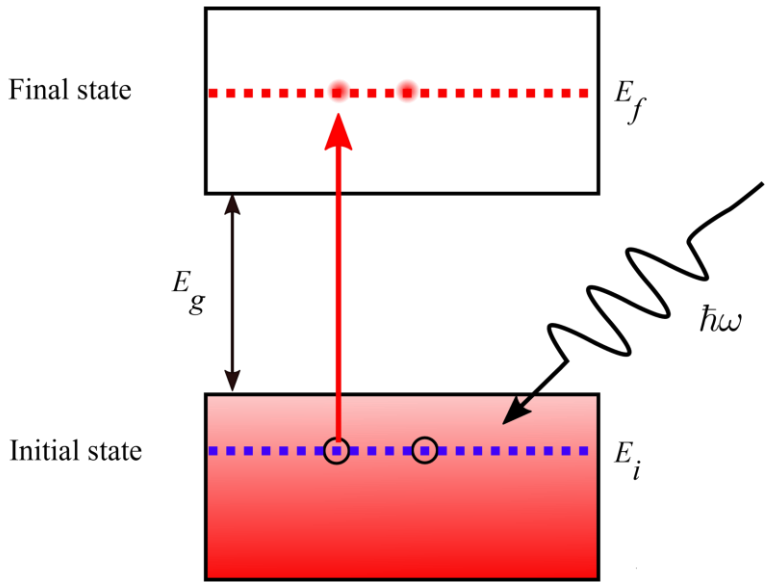

Figure 2.10 Excitation of electrons from ground initial state, E_i to the final state, E_f during an event of interband absorption.

Direct Band and Indirect Band

The interband absorption efficiency depends strongly on the band structure of the solid. As shown in **Figure 2.11**, the valence band maximum (VBM) and conduction band minimum (CBM) for a direct band gap material are located at the Brillouin center, where k = 0. The absorption or emission process involves energy and momentum conservation as shown in **Figure 2.11**, where:

$$E_f = E_i + \hbar\omega \quad (2.15)$$

$$k_f = k_i = k \quad (2.16)$$

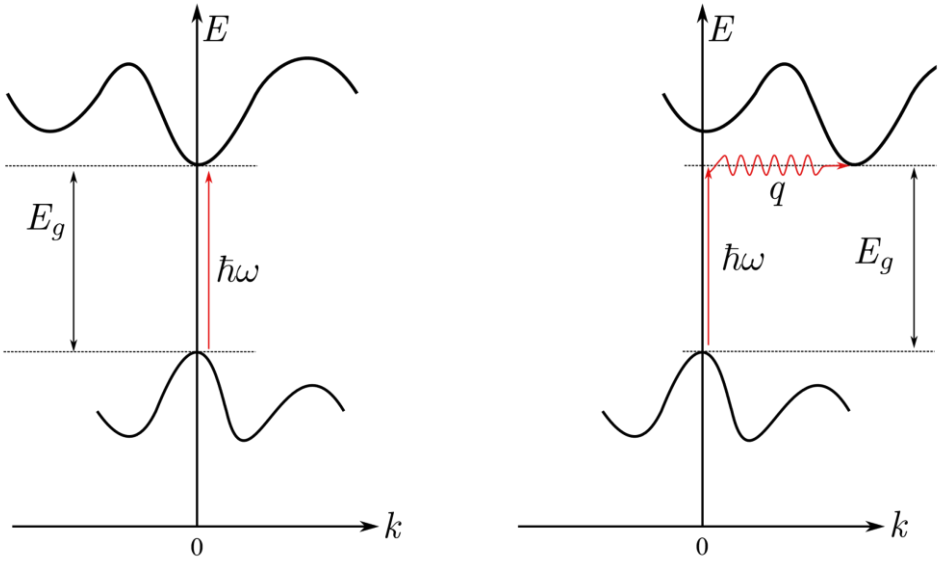

Figure 2.11 Interband transition for a solid with (a) direct and (b) indirect band gap. The red solid lines indicate the electron excitation from the valence to conduction bands. The wiggly arrow corresponds to the absorption or emission of phonon process.

On the other hand, the CBM of an indirect band material is usually found at/near the edge instead of the zone center. The wave vector or momentum of the electrons must be changed from the VBM to the CBM, where a phonon-assisted process is involved:

$$E_{\mathrm{f}} = E_{\mathrm{i}} + \hbar\omega \pm E_{\mathrm{ph}} \qquad 2.17$$

$$k_{\mathrm{f}} = k_{\mathrm{i}} + k_{\mathrm{ph}} \qquad 2.18$$

E_{i} and E_{f} are the electron energy at initial and final states, respectively. E_{ph} is the phonon energy. k_{i} and k_{f} are the momentum of electron at intimal and final states, whereas k_{ph} is the momentum of phonon. Because of the additional phonon process, the

optical absorption efficiency in the indirect band gap material is much lower than the direct one. The typical direct band gap semiconductors are GaAs, InP, and InAs, while indirect band gap semiconductors are Si, Ge and AlAs.

Interband Emission

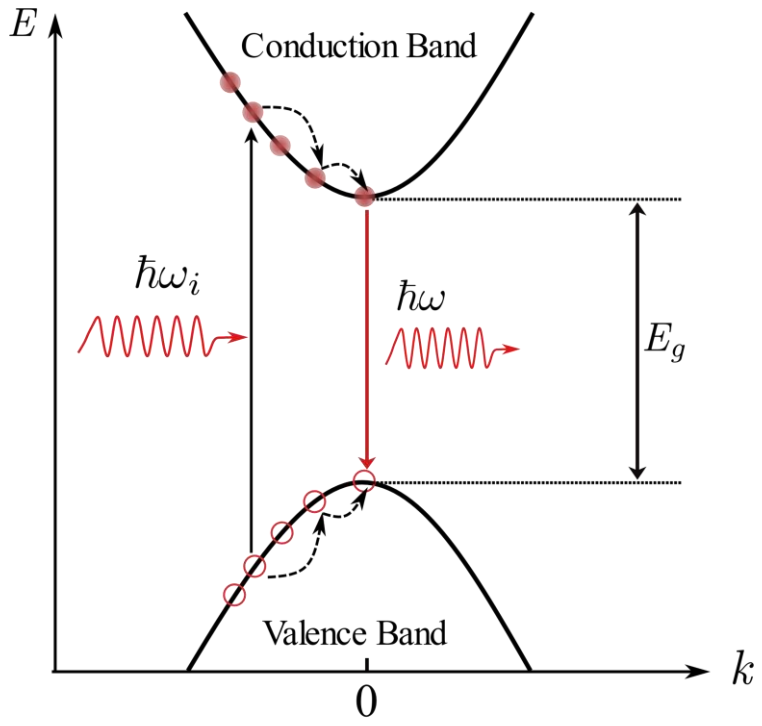

Figure 2.12 Schematic diagram showing the relaxation of electrons from excited to ground state *via* the emission of thermal energy and light.

As shown in **Figure 2.12** optically excited electrons or holes relax to the band edge with the release of thermal energy within a very fast time scale of femtosecond. The electrons move down and combine with holes in the valence band edge *via* a light emission process, called luminescence, with the most common ones being photoluminescence (after absorbing a photon) and electroluminescence (after running an electrical current). Meanwhile, the combination of electrons with holes may occur

through radiative and nonradiative recombinations (involving trapped state or Auger recombination) as shown in **Figure 2.13**. Rate equation for the radiative recombination is:[67]

$$\left(\frac{dN}{dt}\right)_{\mathrm{r}} = -AN \qquad 2.19$$

$$N(t) = N(0)\exp(-At) = N(0)\exp(-t/\tau_{\mathrm{r}}) \qquad 2.20$$

where $\tau_{\mathrm{r}} = A^{-1}$ is the radiative lifetime and A is the Einstein A coefficient. Taking nonradiative recombination into consideration, the total rate equation is given as:[67]

$$\left(\frac{dN}{dt}\right)_{\mathrm{Total}} = -\frac{N}{\tau_{\mathrm{r}}} - \frac{N}{\tau_{\mathrm{nr}}} = -N\left(\frac{1}{\tau_{\mathrm{r}}} + \frac{1}{\tau_{\mathrm{nr}}}\right) \qquad 2.21$$

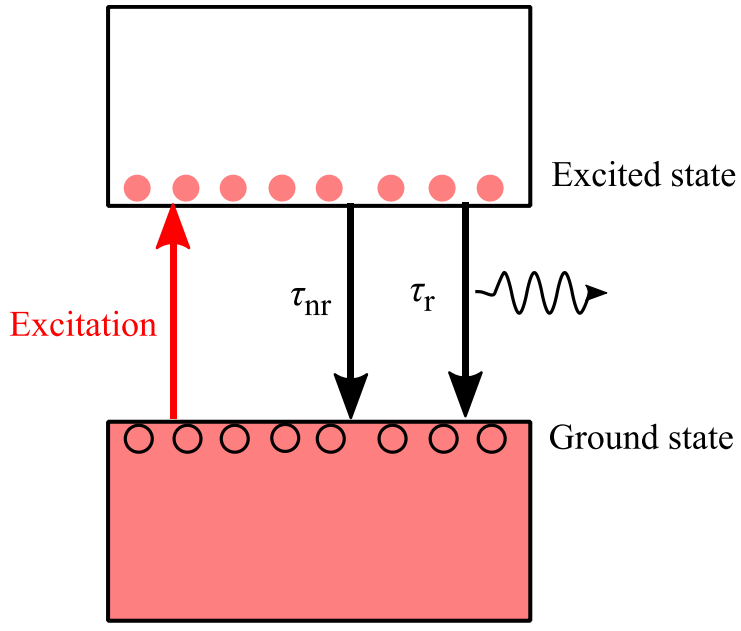

Figure 2.13 General schematic of photoluminescence in a semiconductor. τ_{r} and τ_{nr} are the radiative decay/relaxation and nonradiative decay time, respectively.

$\frac{1}{\tau_r}$ and $\frac{1}{\tau_{nr}}$ correspond to the radiative and nonradiative decay/relaxation rates, respectively. Since quantum efficiency or quantum yield, η is defined as the ratio between the populations of radiated excitons and the total created excitons, therefore:[67]

$$\eta = \frac{AN}{N(1/\tau_r + 1/\tau_{nr})} = \frac{1}{1+\tau_r/\tau_{nr}} \qquad 2.22$$

Here, we see that the quantum yield, η is proportional to the nonradiative lifetime, τ_{nr} and the PL intensity, *I* as $AN \propto I$.

Quasiparticles

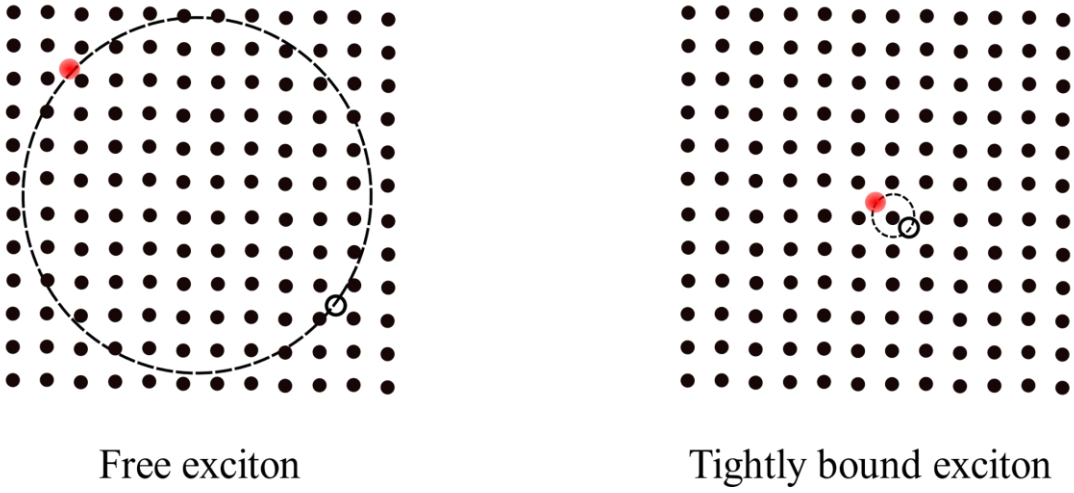

Figure 2.14 Schematic diagrams of a free exciton and a tightly bound exciton. The red dots represent an electron and the empty black circles are a hole.

Absorption of a photon excites the electrons to the conduction band, creating holes in the valence band. Due to the mutual coulomb attraction, an electron and a hole are bound together forming a neutral quasiparticle called exciton. As displayed in **Figure 2.14**, there are two main kinds of excitons, namely the free

exciton (Wannier-Mott exciton) and the tightly bound exciton (Frenkel exciton). The free exciton has a very large radius with a small binding energy of approximately 0.01 eV. It can move freely throughout the crystal. The tightly bound exciton, on the contrary, is bound to a specific atom in a localized state with a larger binding energy of 0.1 to 1 eV. Since the thermally excited phonon energy, $k_B T$ is ~0.025 eV at room temperature, the free exciton can usually be observed only at a cryogenic temperature. From the Bohr's model, the exciton energy, $E(n)$ can be given by:[67]

$$E(n) = -\frac{\mu}{m_0}\frac{1}{\varepsilon_r^2}\frac{R_H}{n^2} = -\frac{R_X}{n^2} \qquad 2.23$$

where R_H is Rydberg energy of the hydrogen atom (13.6 eV), $R_X = \frac{\mu}{m_0}\frac{1}{\varepsilon_r^2}R_H$ is the exciton Rydberg energy, and *n* is the principle quantum number. Meanwhile, radius of the exciton is given by:[67]

$$r_n = \frac{m_0}{\mu}\epsilon_r n^2 a_H H = n^2 a_X \qquad 2.24$$

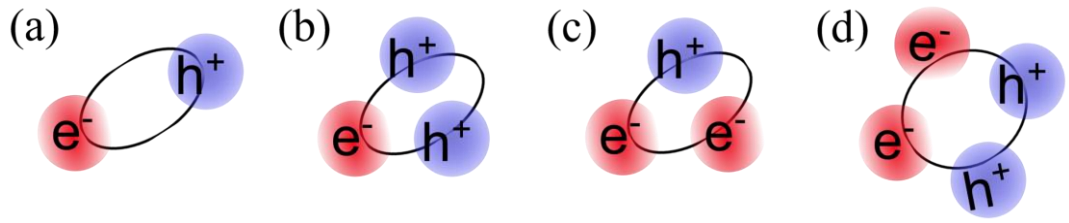

Figure 2.15 Models of the (a) neutral exciton (X), (b) positively charged trion (X^+), (c) negatively charged trion (X^-) and (d) biexciton (XX), respectively.

where a_{H} (5.29×10^{-11} m) is the radius of hydrogen atom and $a_{\mathrm{X}}=\frac{m_0\epsilon_r}{\mu}a_{\mathrm{H}}$ is the exciton Bohr radius.

In heavily doped (*n* or *p)* semiconductors, the exciton can combine with an electron or a hole to form a new quasiparticle, called trion, of either negatively or positively charged. Two excitons can also interact with each other to form biexciton as showed in **Figure 2.15**. In order to differentiate the excitons generated under different formation mechanism, they are also referred as A, B and C excitons in low dimensional materials, in which the coulomb interaction and spin orbital interaction become much stronger.

Effective Mass

Although the excited electrons in conduction band and holes in valence band behave like free particles, but their masses are different from the genuinely free electrons.[67] The modified mass is called an effective mass, which is usually different for electrons and holes and the value varies depending on the materials.

2.1.6. **Basics of Raman scattering**

When an incident light strikes on surface of a medium, it will be scattered either elastically or inelastically. While its frequency is conserved in the former, the inelastic scattering results in a change of frequency, by which C. V. Raman came up with the renowned Raman scattering shown in **Figure 2.16**. The change of incident light frequency in Raman scattering is due to the molecular vibrations and phonons in a crystal.

As illustrated in **Figure 2.17**, he scattered light shares similar angular frequency, ω and wave vector, *k* with the incident light in **Figure 2.17**. Rayleigh scattering. However,

this is not the case for Stokes and anti-Stokes Raman scatterings. The ω and k of the incident light are changed and the relationships are described below for Stokes and anti-Stokes, respectively. The change of ω and k in Stokes scattering and Anti Stokes scattering is given by:

$$\omega_1 = \omega_2 + \Omega \quad (2.25)$$

$$k_1 = k_2 + q \quad (2.26)$$

$$\omega_1 = \omega_3 - \Omega \quad (2.27)$$

$$k_1 = k_3 - q \quad (2.28)$$

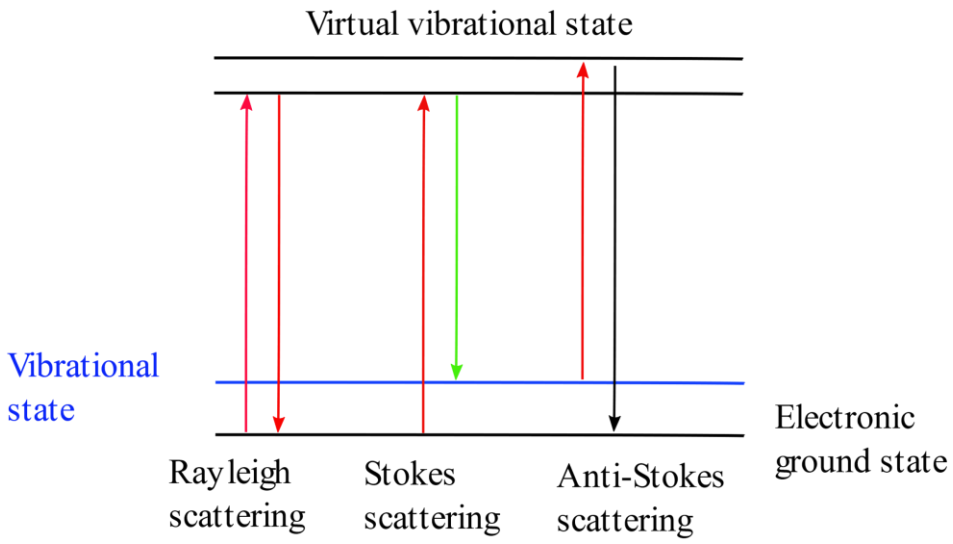

Figure 2.16 Schematic diagram showing the principles of Rayleigh and Raman (Stokes and anti-Stokes) scatterings.

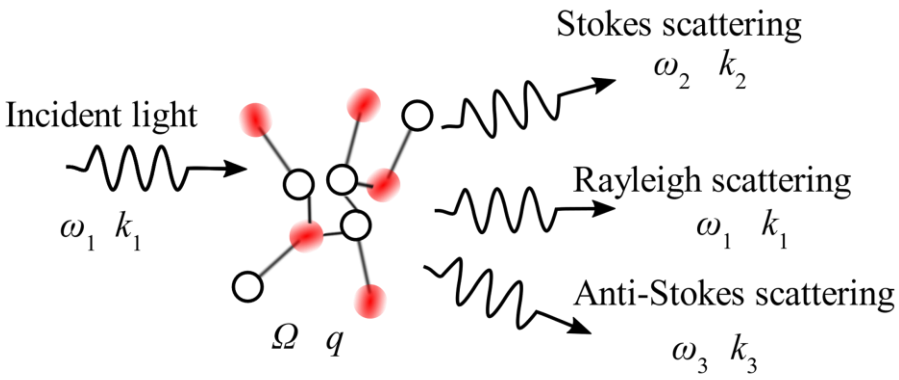

Figure 2.17 A simple representation of the Rayleigh and Raman scatterings. ω and Ω are frequencies; k and q are wave vectors.

2.1.7. **Optical anisotropy and polarization**

For liquid, gas, glasses and amorphous materials, their optical properties are same in all directions. However, whereas some crystals may have a proffered preferred physical axis, resulting which is the origin of optical anisotropy. Although Such anisotropic behavior can also be induced by an applying strain or electric field in some cases can also induce optical anisotropy, but we will only introduce focus only on the natural anisotropy here. The most common manifestation of the natural anisotropy is the birefringence. This property can be understood through a relationship between the polarization, $\boldsymbol{P}$ and the electric field, $\boldsymbol{\varepsilon}$:[67]

$$\boldsymbol{P} = \epsilon_0 \boldsymbol{\chi} \boldsymbol{\varepsilon} \qquad 2.29$$

where $\boldsymbol{\chi}$ is the susceptibility tensor. In the matrices:[67]

$$\begin{pmatrix} P_x \\ P_y \\ P_z \end{pmatrix} = \epsilon_0 \begin{pmatrix} \chi_{11} & \chi_{12} & \chi_{13} \\ \chi_{21} & \chi_{22} & \chi_{23} \\ \chi_{31} & \chi_{32} & \chi_{33} \end{pmatrix} \begin{pmatrix} \varepsilon_x \\ \varepsilon_y \\ \varepsilon_z \end{pmatrix} \quad 2.30$$

By choosing *x*, *y* and *z* to correspond to the principle axes of the crystal, and $\boldsymbol{\chi}$ is given by:[67]

$$\boldsymbol{\chi} = \begin{pmatrix} \chi_{11} & 0 & 0 \\ 0 & \chi_{22} & 0 \\ 0 & 0 & \chi_{33} \end{pmatrix} \quad 2.31$$

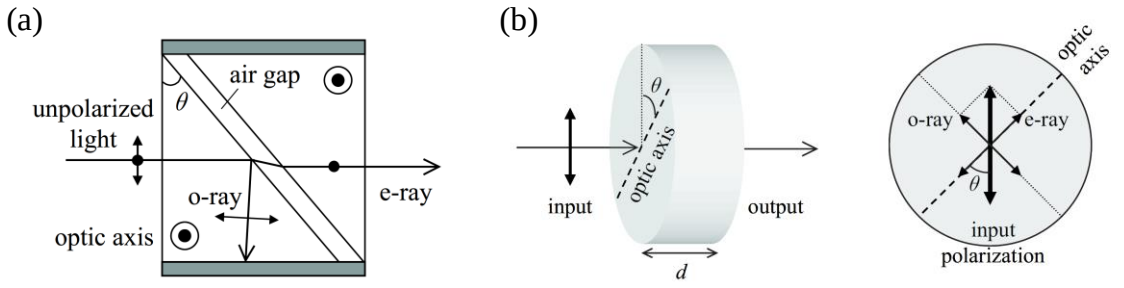

Figure 2.18 Schematic representations of a Glan-Foucault polarizing prism (a) and a retarder plate (b). (Reprinted from Ref.[67] with the permission of the Licensor through PLSclear.)

Since $\chi_{11} = \chi_{22} = \chi_{33}$ for cubic crystals, and their optical properties are hence isotropic. Meanwhile, tetragonal, hexagonal, and trigonal crystals such as quartz, calcite, and sapphire are uniaxial crystals in which there is only a single optic axis. Orthorhombic, monoclinic, and triclinic crystals such as mica are biaxial crystals.[67]

Double refraction is the demonstration of birefringence in a uniaxial crystal. The crystal separates an unpolarized light into two orthogonally polarized rays, the ordinary *o*-ray (one that obeys Snell's law) and extraordinary *e*-ray (one that does not obey Snell's

law), because the refractive indices, n_o and n_e are different for these rays. The crystals with this property are widely used in optical components to control the polarization states of light, such as Glan–Foucault or Glan–Thompson polarizing prisms and retarder plates (quarter or half wave plate) shown in **Figure 2.18**.[67] The name of half and quarter wave plates originates from the phase difference, $\Delta\phi$ between the *o*- and *e*-rays, which is given by:

$$\Delta\phi = \frac{2\pi|n_e - n_o|d}{\lambda} = \frac{2\pi|\Delta n|d}{\lambda} \qquad 2.32$$

where d is the thickness of the plate. A quarter wave plate has $\Delta\phi = \pi/2$, where the phase difference between *o*- and *e*-rays is $\lambda/4$. It turns a linearly polarized light into a circularly polarized one and vice versa. In contrast, when $\Delta\phi = \pi$, it is the half wave plate which rotates the polarization direction of a linearly polarized light.

2.1.8. **Spin injection**

The electrons are of either spin up (m_s = +1/2) or down (m_s = -1/2) under a magnetic field. When they absorb a $\sigma^+(\sigma^-)$ circularly polarized light whose photons carry a $+\hbar(-\hbar)$ angular momentum, it creates a net electron spin and this is called optical spin injection. **Figure 2.19** shows a typical band diagram of the narrow gap III-V semiconductors with cubic zinc blende structure. The conduction band is the *s* like anti-bonding states with an orbital angular momentum quantum number, L = 0. In contrast, the valence band is the *p* like states with L = 1. It comprises the degenerated heavy (hh) and light hole (lh) bands, and the spin orbit (SO) splitting band at k = 0 as shown in **Figure 2.20**. Because the electrons and holes have a spin quantum number, S = 1/2, the total angular momentum, J in the conduction band is 1/2 ($J = L + S$); whereas, J = 3/2 or 1/2

in the valence band at k = 0. The energy difference Δ is from the spin orbit splitting as shown in **Figure 2.20**.[67] As displayed in **Figure 2.20** (b), the transition from the valence to conduction band by the $\sigma^+(\sigma^-)$-polarized light with $+\hbar(-\hbar)$ photon momentum occurs only when $\Delta M_J = +1$ or -1.

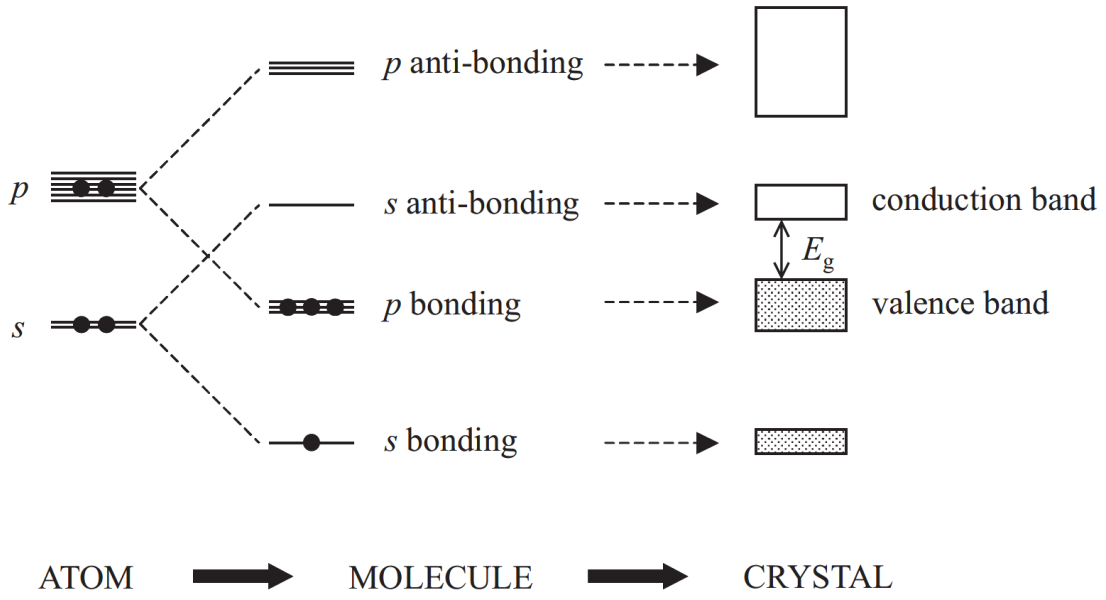

Figure 2.19 Schematic diagram of the electron levels in a III-V semiconductor with four valent atoms (GaAs). The valence band is the *p* bonding state, while the conduction band is the *s* anti-bonding state. (Reprinted from Ref.[67] with the permission of the Licensor through PLSclear.)

The electron spin polarization, Π can be obtained as follows:

$$\Pi = \frac{N(+1/2)-N(-1/2)}{N(+1/2)+N(-1/2)} \qquad 2.33$$

In bulk III-V semiconductors, Π is -50% (50%) under the σ^+ (σ^-) excitation. Meanwhile, because of the spin orbit coupling interaction, hole spins are usually

randomized within an extremely short period of time. Hole spin polarization is thus considered negligible in general.[67]

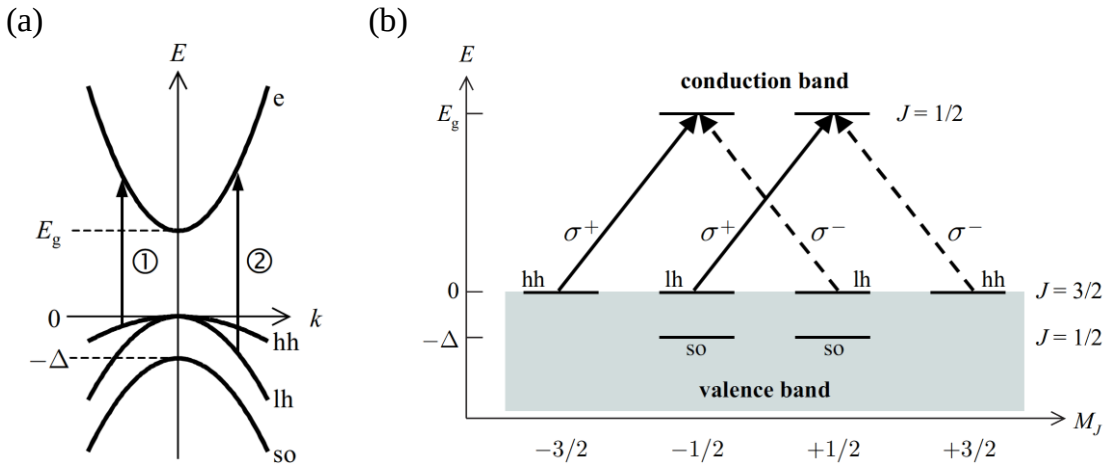

Figure 2.20 Band structure of III-V semiconductor (GaAs) with heavy hole (hh), light hole (lh), split off (so) hole band and electron bands (a). Circularly polarized photon transitions from the valence to conduction band under 0 T magnetic field (b). (Reprinted from Ref.[67] with the permission of the Licensor through PLSclear.)

Nonetheless, the spin polarization is somehow different in low dimensional materials. **Figure 2.21** illustrates the optical transitions for the 2D quantum well of GaAs with a cubic zinc blende structure. As the material reduces in size, the degenerated heavy and light hole states are split due to the quantum confinement effect induced difference of confinement energy. For an incident light with a photon energy of $\hbar\omega$, where

$$E_g + E_{e1} + E_{hh1} \leq \hbar\omega < E_g + E_{e1} + E_{lh1} \qquad 2.34$$

it is hence possible to generate a 100% electron spin polarization. Since the fully spin polarized heavy hole can also be created at the same time, rather than the individual electron or hole state, the exciton state should be considered instead in the analysis of spin relaxation under this circumstance.[67]

During relaxation of the excited electrons and holes, the PL emitted is consisted of the I^+ and I^- components, which correspond to the σ^+ and σ^- circularly polarized light transitions, respectively. Similar to the aforementioned spin polarization, the degree of PL polarization, ρ is given by:

$$\rho = \frac{I^+ - I^-}{I^+ + I^-} \qquad 2.35$$

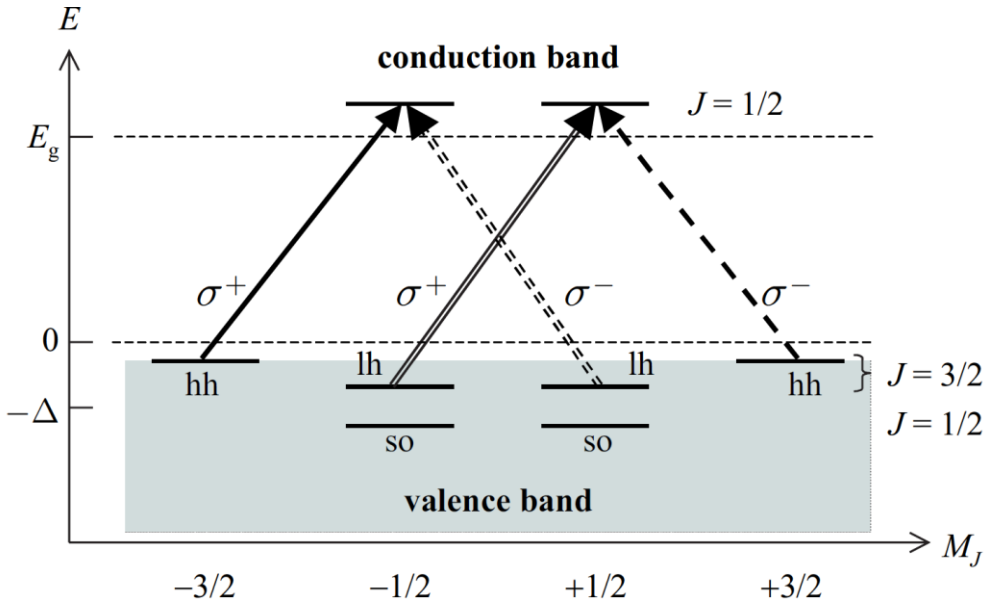

Figure 2.21 Selection rules for the circularly polarized light in a quantum well of the III-V semiconductor with zinc blende structure. (Reprinted from Ref.[67] with the permission of the Licensor through PLSclear.)

2.2. Basic properties of atomic layered 2D TMDs

TMDs are not new materials. MoS_2, for instance, was known almost a century ago. It is a naturally found crystal, which has been widely used as a dry lubricant because of its low friction and robustness. Since 2004, the success in graphene isolation has brought this type of layered materials into attention as they demonstrate useful physical properties for energy related applications when thinned. The optical properties of atomically thin, layered 2D TMDs will be introduced in this section starting from their crystal and band structures.

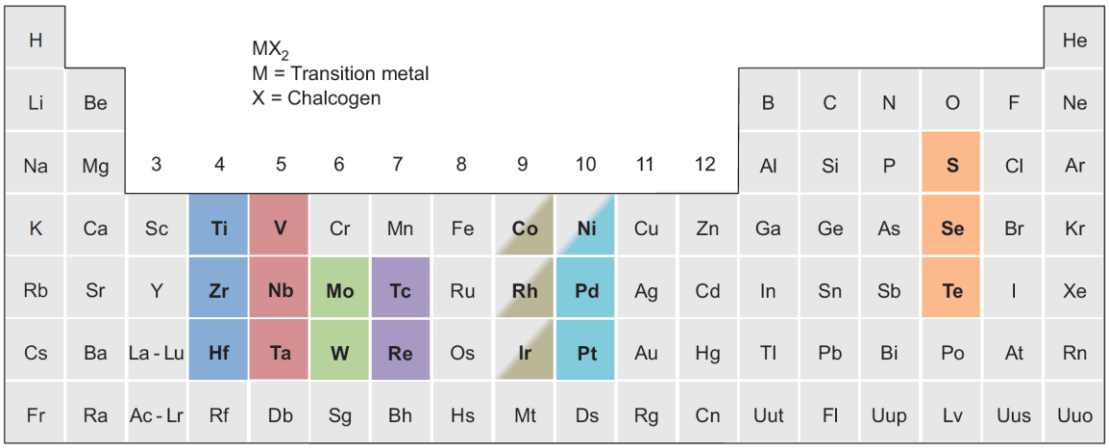

Figure 2.22 Periodic table showing possible combinations of different elements that form layered MX_2. (Reprinted with the permission from Ref.[72]. © 2013 Springer Nature.)

2.2.1. Crystal and electronic band structures of TMDs

Layered TMDs are composed of MX_2, where M is the transition metals and X is the chalcogens as shown in **Figure 2.22**.[72] The metal atoms are sandwiched between the chalcogen atoms, forming a layer thickness of approximately 0.6~0.7 nm as shown in **Figure 2.23**[73] With the intra layer M-X bonds being predominantly covalent, these layers

are stacked and held together by the van der Waals (vdW) forces. This vdW force is stronger for the tellurides than that in sulphides. As illustrated in **Figure 2.23**, bulk TMDs exhibit a wide variety of polymorphs and stacking polytypes, such as 1*T* (tetragonal symmetry, one layer per repeat unit, octahedral coordination), 2*H* (hexagonal symmetry, two layers per repeat unit, trigonal prismatic coordination), and 3*R* (rhombohedral symmetry, three layers per repeat unit, trigonal prismatic coordination) stackings.[74] For MoS_2, the naturally found polymorph is the 2*H* phase, which has an AB stacking. Monolayer (1L) TMDs usually exhibit only the hexagonal or tetragonal symmetry structure, which belongs to the D_{3h} and D_{3d} point groups, respectively.[72,74]

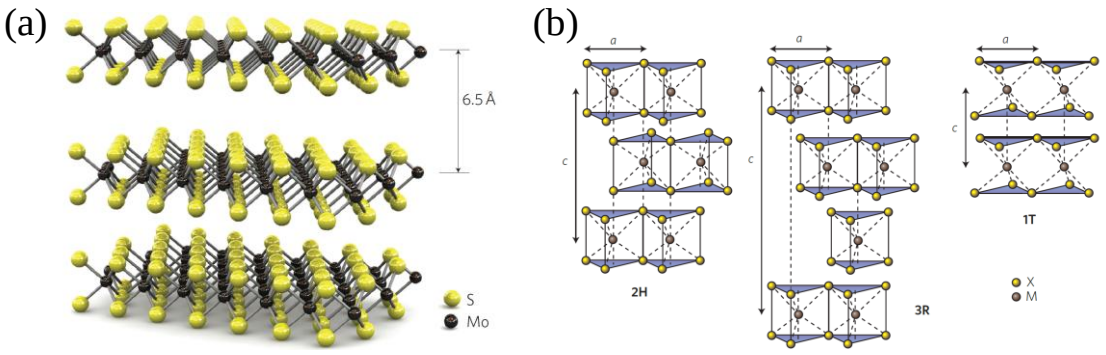

Figure 2.23 Schematic representations of the layered TMD MX_2 structure (a), and its polytypes with 2*H*, 3*R* and 1*T* stackings (b). The stacking index, *c* indicates the number of layers in each stacking order. The lattice constant, *a* ranges from 0.31 to 0.37 nm depending on the compound. (Figure a is reprinted with the permission from Ref.[73]. © 2011 Springer Nature. Figure b is reprinted with the permission from Ref.[74]. © 2012 Springer Nature.)

The electronic structure of the TMDs is determined by the number of *d* electron counts and the coordination of transition metal,[72], rendering a rich variety in their physical

properties. For example, MoS_2 with a 2*H* phase stacking is semiconducting, whilst its 1*T* phase shows a metallic property. As shown in **Figure 2.24**, the TMDs also show a thickness dependent electronic structure, which arose from the confinement effect as they are being thinned. While the bulk materials have an indirect bandgap of approximately 1.0 eV, 1L TMDs are direct bandgap semiconductors. The CBM and VBM of these 1L TMDs are located at the same *K* point in the Brillouin zone, with an energy difference of 1.1-1.9 eV. This pair of CBM and VBM is also referred to as the *K* valley because of their valley-like energy dispersion bands.[28,75]

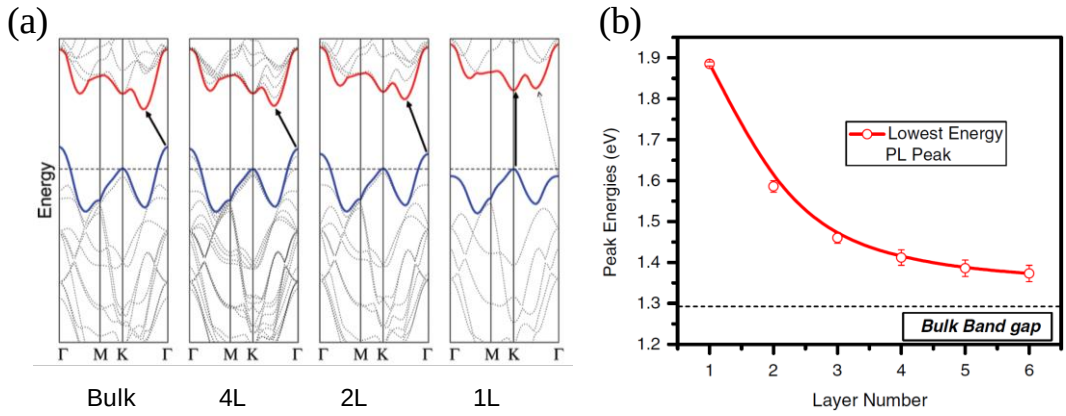

Figure 2.24 Calculated electronic band structures of MoS_2 from bulk to quadrilayer (4L), bilayer (2L), and monolayer (1L) (a). The experimental PL peak energies in different layers of MoS_2 (b). (Figure a is reprinted with the permission from Ref.[75]. © 2010 ACS. Figure b is reprinted with the permission from Ref.[28]. © 2010 APS.)

One of the reasons for the indirect (bulk) to direct (1L) gap transition is due to the lack of inversion symmetry in 1L hexagonal lattice (**Figure 2.23** and **Figure 2.25** (a)) Because of this broken inversion symmetry, the strong spin-orbit coupling effect splits the valence band with an engergy of ~160 to 450 meV.[35,76] Electrons in these two split

bands have different spins aligning downward ($E_{\downarrow}$) or upward ($E_{\uparrow}$) as shown in **Figure 2.25** (c). Since $E_{\downarrow}(k) = E_{\uparrow}(-k)$ in time reversal symmetry, the valley and spin of the valence band are thus coupled. The degenerated *K* and *K'* valleys of opposite spins located at corners of the Brillouin zone shown in **Figure 2.25** (c) can be selectively excited by a circularly polarized light. Ideally, the spin or valley polarization (as spin and valley are coupled) in TMDs is expected to reach 100%. This is an important feature for the next generation optotronics, the so-called valleytronics or optovalleytronics.

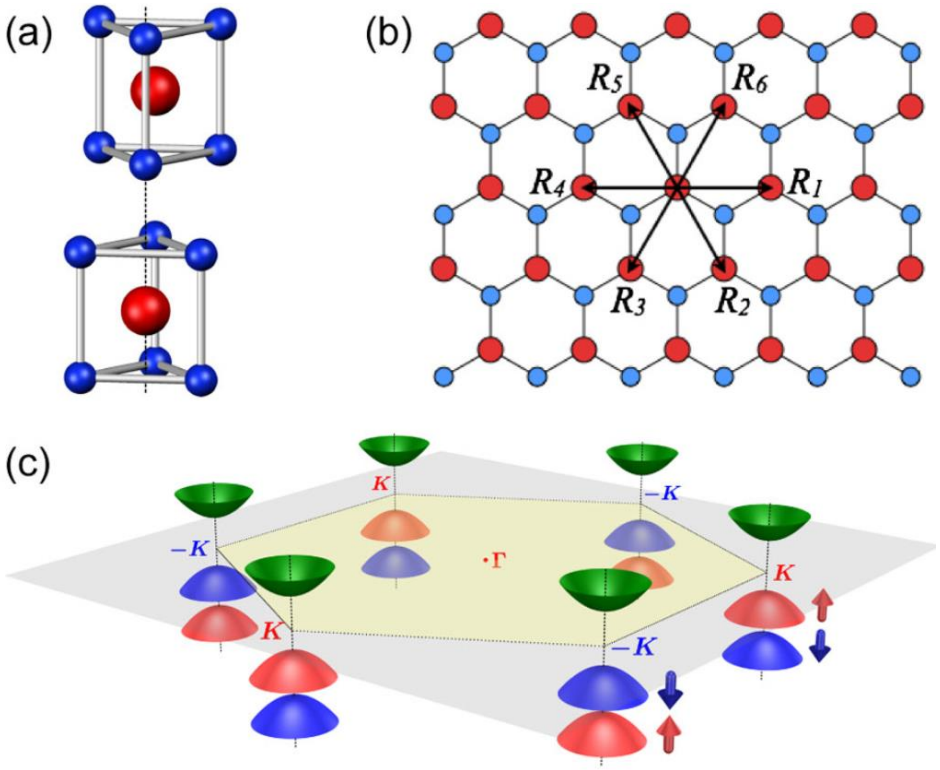

Figure 2.25 The unit cell of a 2*H*-MoS_2 (a) and the top view of 1L MoS_2 (b). Schematic drawing of the Brillouin zone with degenerated but inequivalent K points (c). (Reprinted with the permission from Ref.[76]. © 2012 APS.)

2.2.2. Fundamental optical properties of monolayer TMDs

The fundamental optical properties of 1L TMDs will be introduced in this subchapter by using MoS_2 and WSe_2, the widely studied members of the TMD family, as examples.

Fundamental PL property

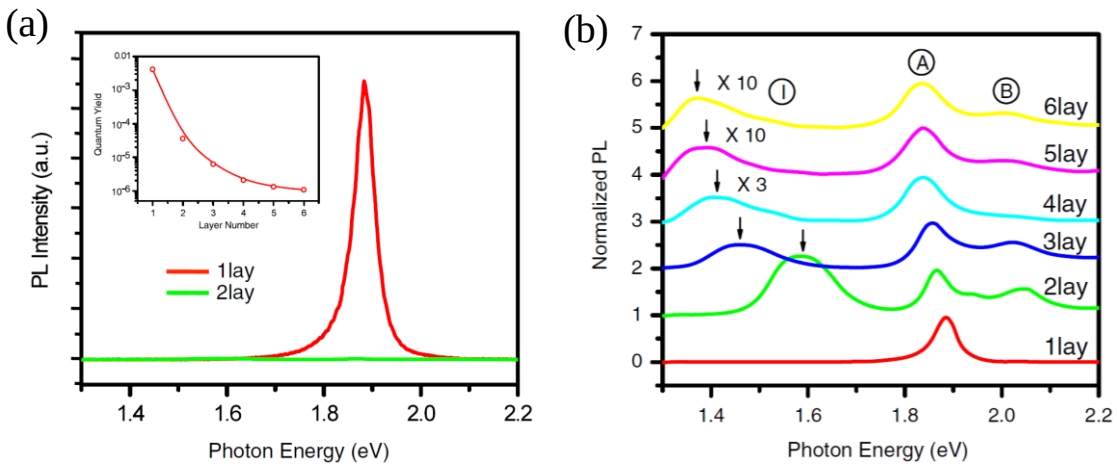

Figure 2.26 PL (a) and normalized PL spectra (b) of 1L to 6L MoS_2. Arrows indicate the indirect band transition. (Reprinted with the permission from Ref.[28]. © 2010 APS.)

The PL and quantum yield in TMDs change gradually with thickness due to their layer dependent electronic structures. As illustrated in **Figure 2.26**, 1L MoS_2 lacks an indirect peak and it has the strongest PL emission among all its other few layer counterparts. Compared to other direct gap semiconductors, 1L TMDs however, suffer low quantum yield (~10^{-3} – ~10^{-2}) in general due to the defects in natural crystals. In order to overcome this, many methods have been developed to improve the quantum yield, which we will discuss later.

Reduced dielectric effect and bound excitons in monolayer TMDs

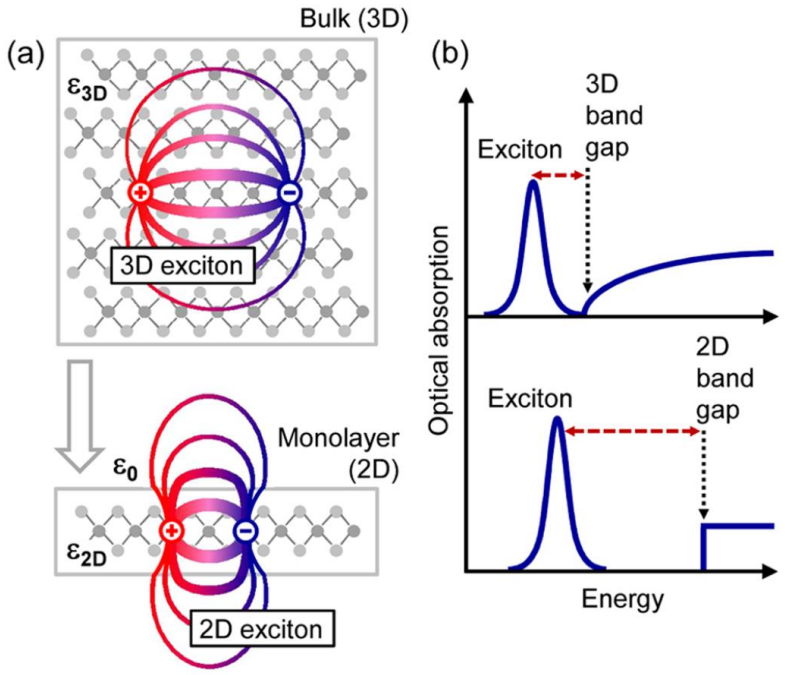

Figure 2.27 Schematic illustrations of the excitons in bulk 3D and 2D TMDs (a). Optical absorption diagram showing the electronic and exciton properties of 3D and 2D TMDs (b). (Reprinted with the permission from Ref.[77]. © 2010 APS.)

Because of the size effect, the dielectric environment is changed considerably in 2D TMDs. The electric field generated from the excitons confined in a 2D plane extends out of the crystal as shown in **Figure 2.27** (a). This results in an increased exciton binding energy with larger bandgap in 1L TMDs as compared to the bulk crystal (F**igure 2.27** (b)).[77] The electric field results from the electron hole pairs which are confined in a 2D plane extends out of the plane as shown in **Figure 2.27** (a), and this further increase the exciton binding energy. Consequently, both the bandgap and exciton binding energy increase in monolayer TMDs compared with bulk crystal as shown in **Figure 2.27.**[77] The

excitons in 2D TMDs, with a large Bohr radius of ~1 nm and the binding energy of 0.2-0.4 eV, hence have the properties of both free and localized excitons.[77]

Raman spectra

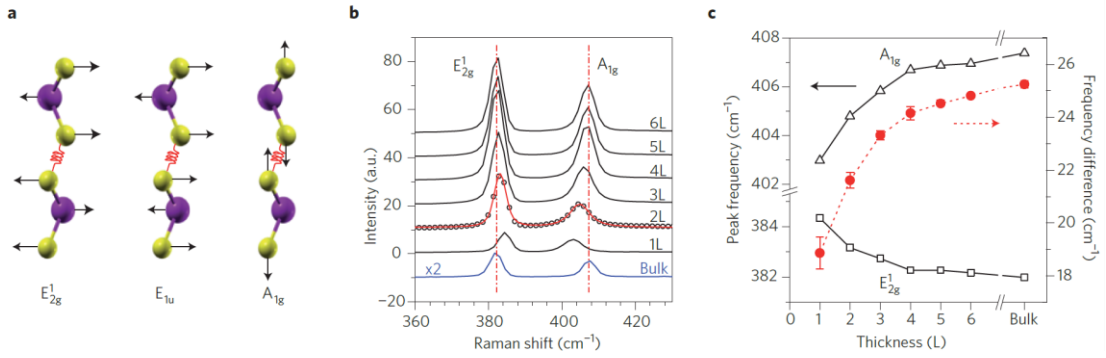

Figure 2.28 Schematic representation of the in-plane (E^1_{2g} and E_{1u}) and out-of-plane (A_{1g}) phonon vibration modes (a). Thickness-dependent Raman spectra of MoS_2 (b) and the corresponding peak position shifts and peak difference for the E^1_{2g} and A_{1g} vibrations as a function of thickness (c). (Reprinted with the permission from Ref.[78]. © 2010 ACS.)

Raman scattering, which correlates to the phonon vibration, has been commonly applied to confirm the identity of TMDs.[78] Two main Raman modes that correspond to the out-of-plane (A_{1g}) and in-plane (E^1_{2g}) phonon vibrations of the MoS_2 are shown in **Figure 2.28** (a).[78,79] They are located at the vicinity of ~402 and ~380 cm^{-1}, respectively in **Figure 2.28** (b). With the decreasing of layer thickness, the A_{1g} peak shows a blue shift, whereas an opposite trend is observed for the E^1_{2g} peak. This may be due to the stacking induced structural change or long range interlayer coulomb interaction. The correlation between the difference of these two modes and the number of layers is shown in **Figure**

2.28 (c). A difference of approximately ~19 cm^{-1} is usually registered for 1L MoS_2 on SiO_2.

Valley polarization property

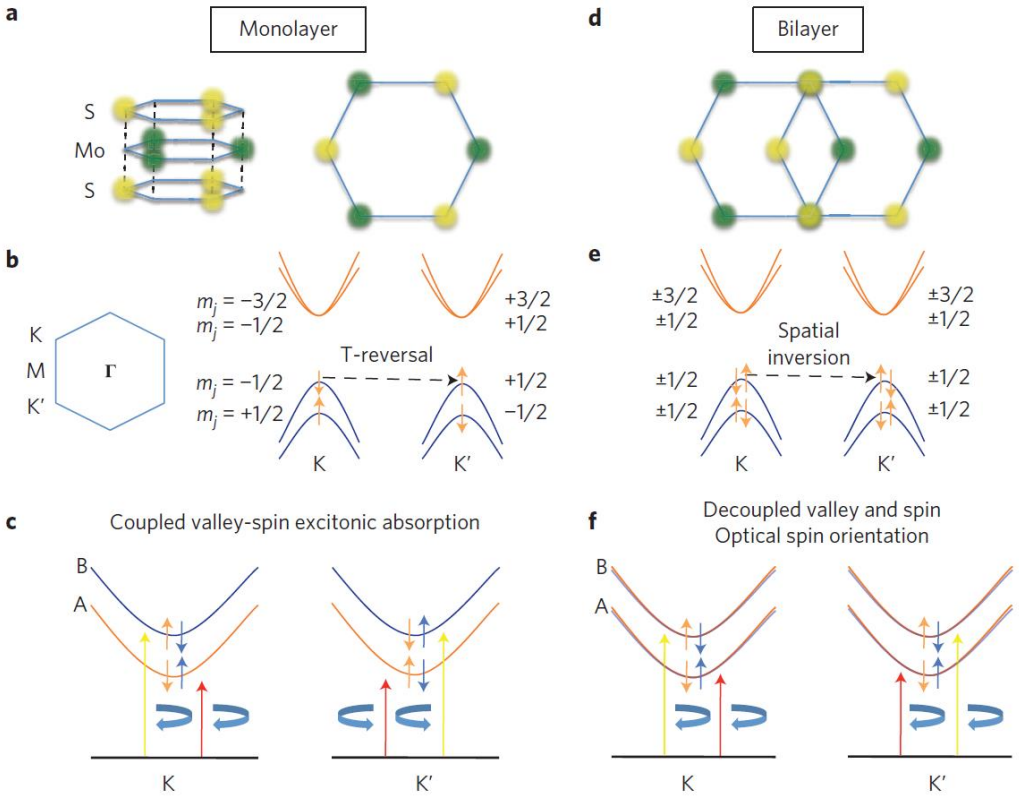

Figure 2.29 Atomic and electronic structures of 1L(a-c) and 2L (d-f) MoS_2, respectively. The inversion symmetry of 2L MoS_2 is broken in 1L MoS_2 (a, d). The valence band edge is lifted. Spin-valley is coupled in 1L but not in 2L MoS_2 (b, e). The A and B excitons at K and K' valleys are excited equally in 2L MoS_2 (c, f). However, the excitation is selective in 1L MoS_2 under circularly polarized light of an appropriate wavelength. (Reprinted with the permission from Ref.[35]. © 2012 Springer Nature.)

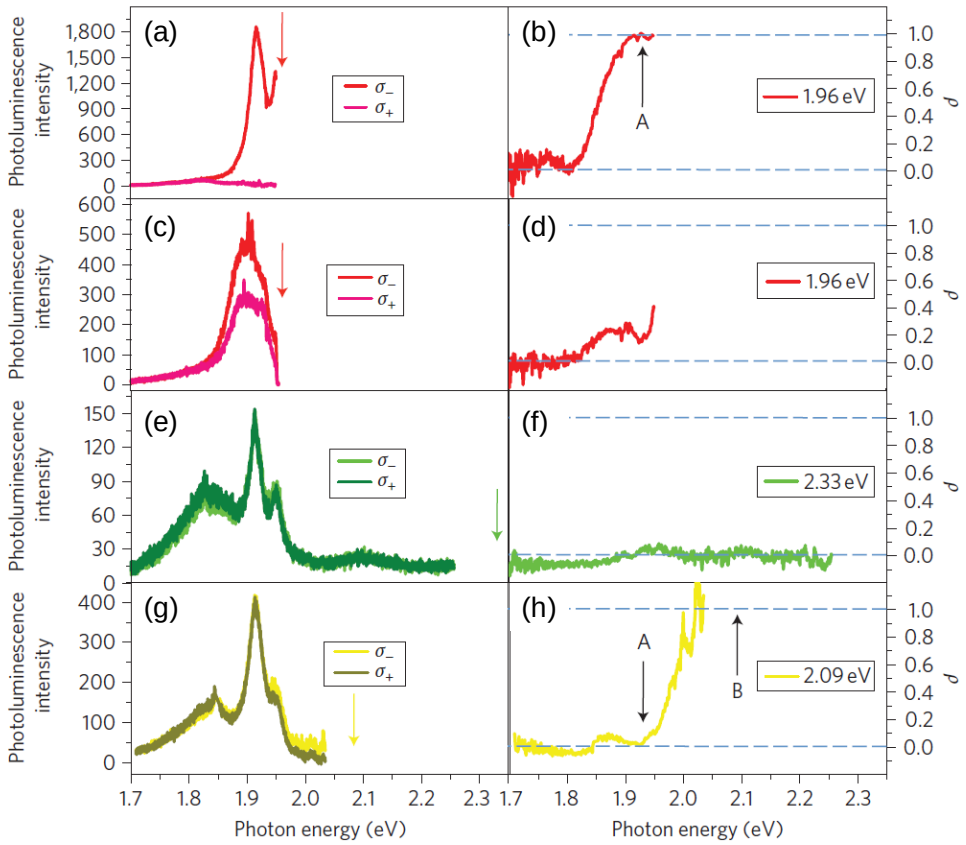

Figure 2.30 PL and valley polarization properties of 1L and 2L MoS_2 under circularly polarized light excitation at different photon energies: 1.96 (a, b), 2.33 (e, f), and 2.09 eV (g, h) for 1L MoS_2; 1.96 eV (c, d) for 2L MoS_2. (Reprinted with the permission from Ref.[35]. © 2012 Springer Nature.)

Because of the AB stacking for 2*H* MoS_2, the inversion symmetry is broken in 1L MoS_2. Besides, the strong spin-orbit coupling induces a large valence band splitting. 1L MoS_2 thus demonstrates spin-valley coupling **Figure 2.29**, whereas otherwise in 2L MoS_2 due to the presence of spatial inversion symmetry. The two inequivalent valleys (K and K') in 1L MoS_2 can be selectively excited using a circularly polarized light of an appropriate photon energy. A near unity valley polarization for A exciton is achieved at

1.96 eV (**Figure 2.30**). This is not the case for bilayer (2L) MoS_2 since the spin and valley are decoupled in 2LTMDs because of the spatial inversion symmetry (**Figure 2.29**).[35]

Since the large spin-orbit splitting has also resulted in the generation of spin polarized holes upon excitation, the electron-hole pairs (excitons) should be considered instead during relaxation. There are many possible channels or mechanisms for the relaxation of polarized excitons such as Elliot-yafet (EY) mechanism, Dyakonov-perel (DP) mechanism and Bir-Aronov-Pikus (BAP) mechanism.[67]

Meanwhile, the polarization property of 1L TMDs is greatly affected by many other effects, which include phonon effect, temperature dependent band edge shift, carrier density and long range coulomb interaction.

2.2.3. **Internal and external effects on the optical properties of monolayer TMDs**

As discussed, 1L TMDs have unique optical properties that are beneficial to the various fields of application. Nonetheless, because of their intrinsic structures and the large specific surface area, these properties could be easily modified by either the internal or external effects described below.

Internal effects on the optical properties

Defects

Naturally found TMD crystals inevitably have many defects and impurities. These defects and impurities become the possible trap states, which reduce the population of radiative excitons, converting them into non-radiative ones. From the equation:

$$\eta = \frac{AN}{N(1/\tau_r + 1/\tau_{nr})} = \frac{1}{1+\tau_r/\tau_{nr}} \qquad 2.36$$

the quantum yield, η is hence extremely low for the natural crystals, which usually on the order of ~10^{-3}.[80,81] In addition, due to the presence of these defects, the 1L TMDs are either *n*- or *p*-doped. The optically excited excitons can easily combine with another electron or hole to form trions in a heavily doped condition. Consequently, the PL of 1L TMDs at room temperature always contains both exciton and trion components. 1L MoS_2 commonly has a trion dominant PL emission at room temperature.[48]

Dark states

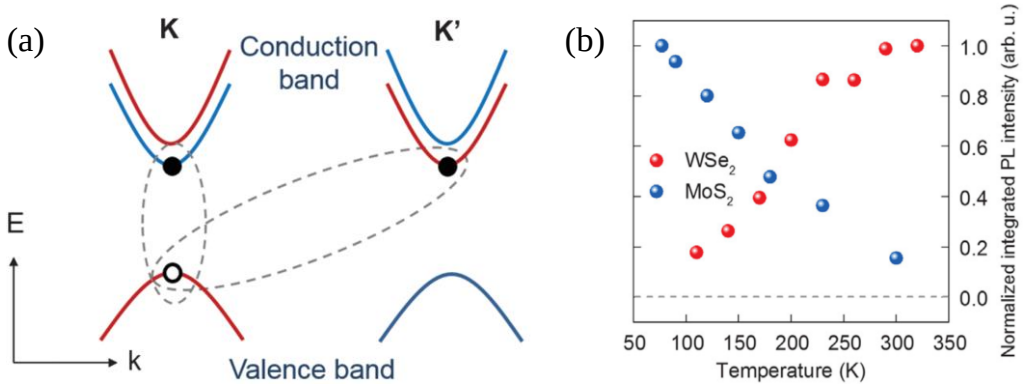

Figure 2.31 Schematic of the intravalley and intervalley dark states in 1L WSe_2 (dashed lines) (a). Temperature dependent normalized integrated PL intensity profile of the 1L WSe_2 and 1L MoS_2 (b). (Reprinted with the permission from Ref.[82]. © 2010 APS.)

Optical dark states, which lie above or below the bright states, are another internal reason for the quenching of light emission from TMDs. As shown in **Figure 2.31** (a), the dark state lying ~30 meV below the conduction band in 1L WSe_2 will trap the excited bright excitons to the ground state. The dark states can be identified using a temperature

dependent PL intensity measurement. In contrast to the 1L WSe_2, the PL intensity in 1L MoS_2 shows an opposite trend with temperature change in **Figure 2.31** (b). This implies that the dark state of 1L MoS_2 is located above the conduction band (about 2~3 meV).[82]

External effects on the optical properties

Substrate effects

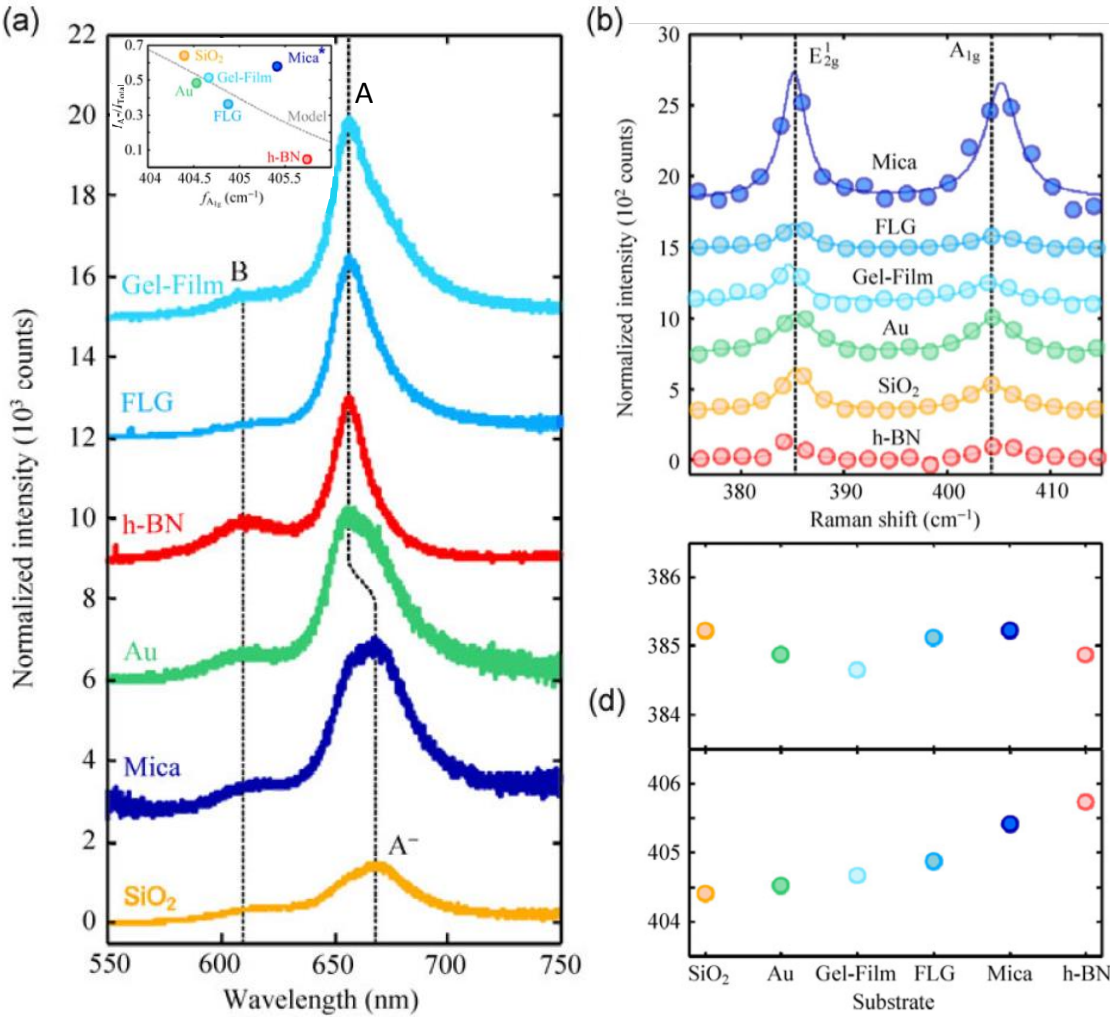

Figure 2.32 Substrate effects on the PL (a) and Raman signals (b) of 1L MoS_2. (Reprinted with the permission from Ref.[41]. © 2012 Springer Nature.)

Because the thickness of 1L TMD samples is only ~0.7 nm, the substrate effects acting upon the material are thus significant. As shown in **Figure 2.32** (a), the PL intensity and peak energy, and the exciton-trion weight ratio are dependent strongly on the substrate. The Raman peak positon is also affected by the different substrates used as shown in **Figure 2.32** (b). This kind of substrate dependent optical properties is mainly arose from the surface interference, dielectric environment and local substrate doping.[41] For the investigation of their intrinsic optical properties, suspended TMD specimens are often prepared to eliminate the influence caused by the supporting substrate.[83]

Strain effects

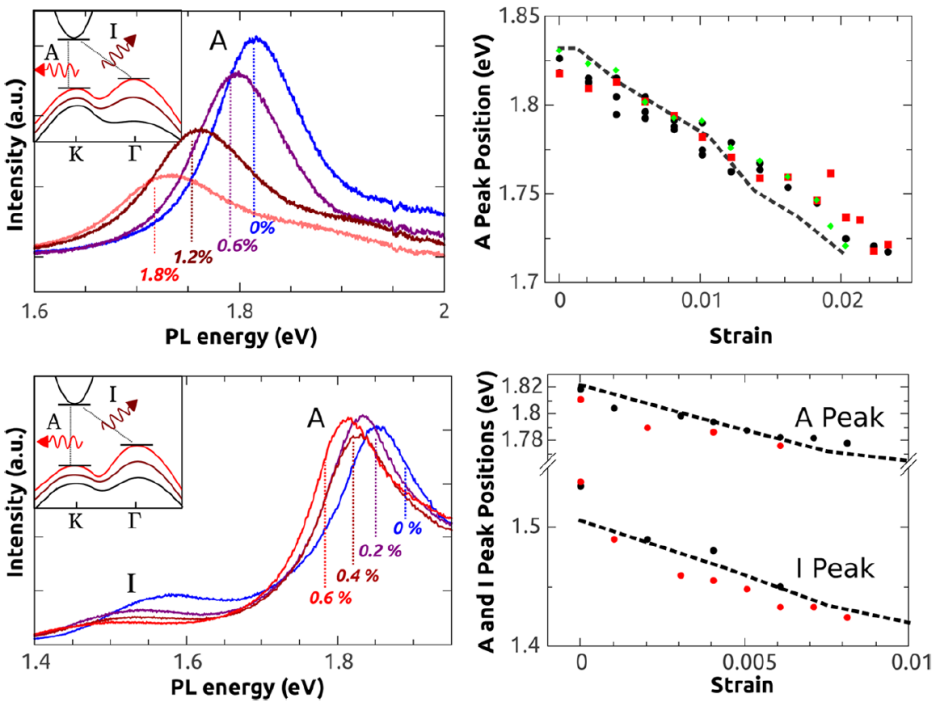

Figure 2.33 Strain induced changes in the PL intensity and peak position of the 1L (a, b) and 2L MoS_2 (c and d). (Reprinted with the permission from Ref.[84]. © 2013 ACS.)

Interface strain is another effect affecting the optical properties of ultrathin TMDs. The PL intensity and peak position of 1L and 2L MoS_2 in **Figure 2.33** are greatly modified due to the strain induced band gap change.[84] Based on this strain induced effect, an artificial atom method has been developed to control the PL property of MoS_2.[85]

Electrical effects

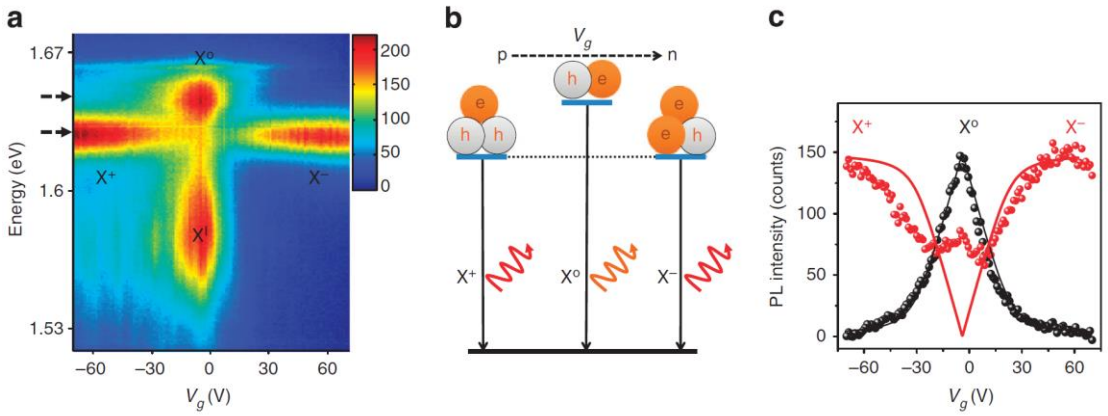

Figure 2.34 PL map of 1L $MoSe_2$ under gating (a). Schematic of positively charged (X^+), negatively charged (X^-) and neutral excitons (X) (b). PL intensities of charged and neutral excitons versus gate voltage (c). (Reprinted with the permission from Ref. [86]. © 2013 Springer Nature.)

Meanwhile, the PL and valley polarization of 1L TMDs can also be modified through the electrical approach.[86,87] **Figure 2.34** shows how carrier density modulation affects the PL of 1L $MoSe_2$. By changing the applied gate voltage, holes or electrons are injected selectively into the 1L $MoSe_2$. The PL intensities from the neutral (X) and charged (positive, X^+ or negative, X^-) excitons can be modulated. This method has also

been used to control the orbital magnetic moments, Zeeman-type spin splitting and valley-Hall effect in 1L TMDs.[88–90]

Magnetic Effects

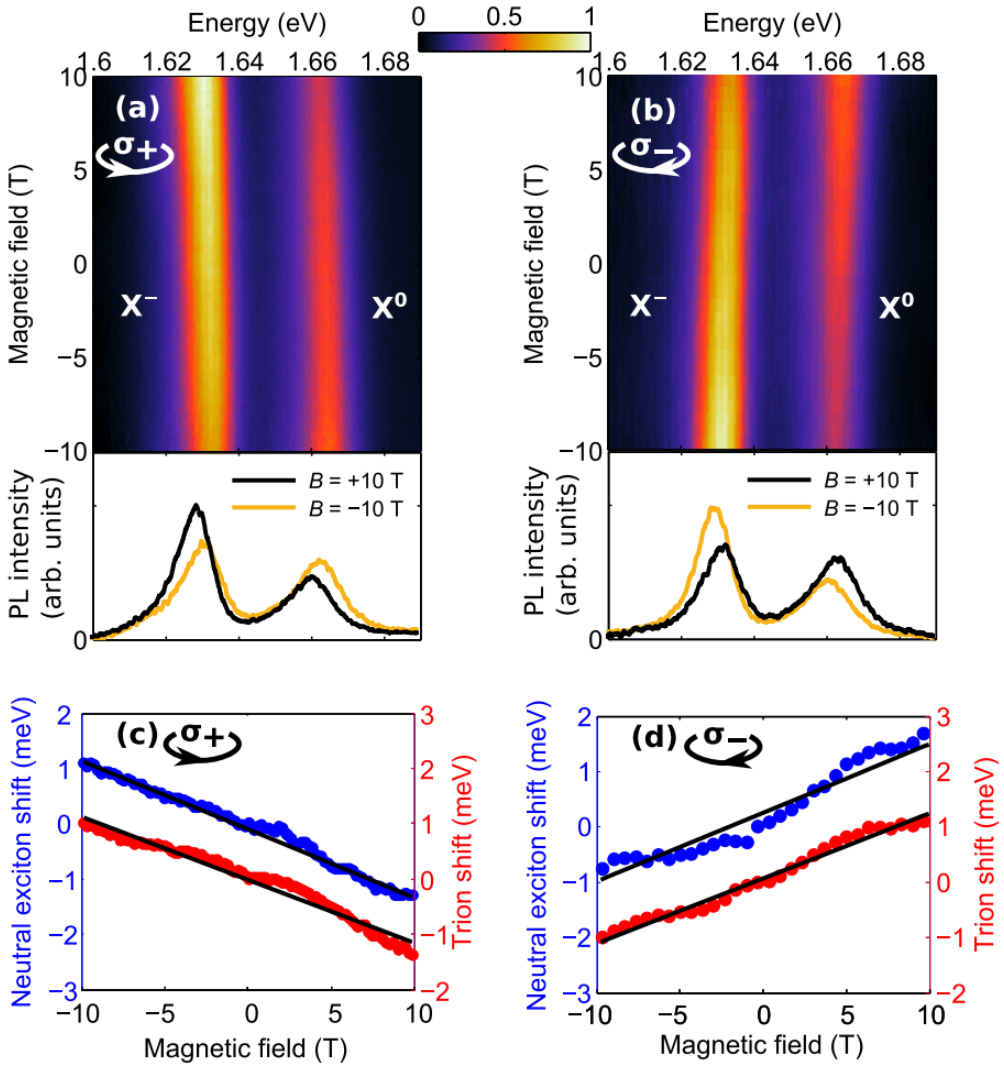

Figure 2.35 Valley polarization maps and PL spectra of 1L $MoSe_2$ under σ^+ (a) and σ^- (b) excitations. Zeeman shift for the exciton and trion under σ^+ (c) and σ^- (d) excitations. (Reprinted with the permission from Ref.[91]. © 2010 APS.)

Magnetic field can be used to couple with the valley magnetic moments and break the valley degeneracy in 1L TMDs. As shown in **Figure 2.35**, the conduction and valence bands in the inequivalent valleys are lifted oppositely by the magnetic field. The PL intensity of both the exciton and trion changes to a different extent and their peak energies are shifted linearly with a *g* factor of 0.12~0.18 meV depending on the doping level.[91]

Chemical Effects

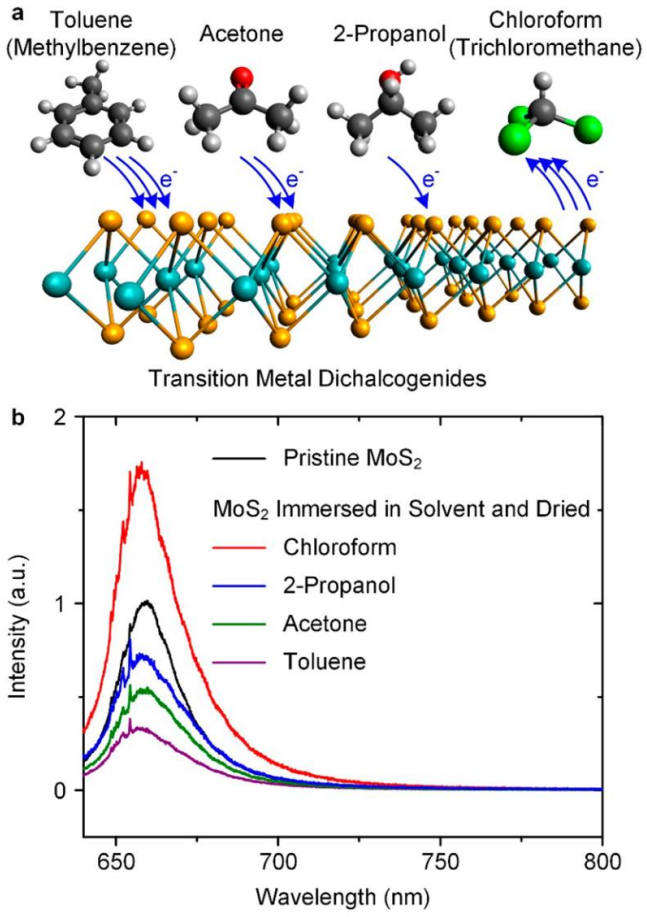

Figure 2.36 Schematic of surface carrier transfer between the different chemicals and 1L MoS_2 (a). PL spectra of the treated 1L MoS_2 (b). (Reprinted with the permission from Ref.[92]. © 2016 ACS.)

Solvent or chemical treatment is one of the easiest and efficient means to modify the optical properties of 1L TMDs. As shown in **Figure 2.36**, the PL intensity of 1L MoS_2 is strongly affected by various types of chemicals. Toluene, acetone and 2-propanol act as the donor molecules transferring electrons to the 1L MoS_2, whereas chloroform is an acceptor to which electrons are donated.[92] Depending on the electronegativity of the chemical used, it results in an overall increase or decrease of the PL intensity.

In a nutshell, because of the confinement effects and large specific surface area, the optical properties of atomically thin materials is succumbed to the influence of various environmental effects. Ultrathin TMDs, with their unique optical characters, have been demonstrating great potentials in photodetectors, transistors, sensors, solar cells and catalysis. For realistic application, understanding the surface interaction between the TMD sheets and environment is crucial as devices will eventually work under diverse conditions consisting of various molecules, gases or solutions.[92] It provides an important key to modulate the fundamental properties of 1L TMDs in such situation, leading to the controllable physical features with long term device stability.

Chapter 3. Experimental methods and setup

In this chapter, experimental method and optical setup for the measurements in this thesis will be introduced.

3.1. Sample preparation

Sample exfoliation and transfer

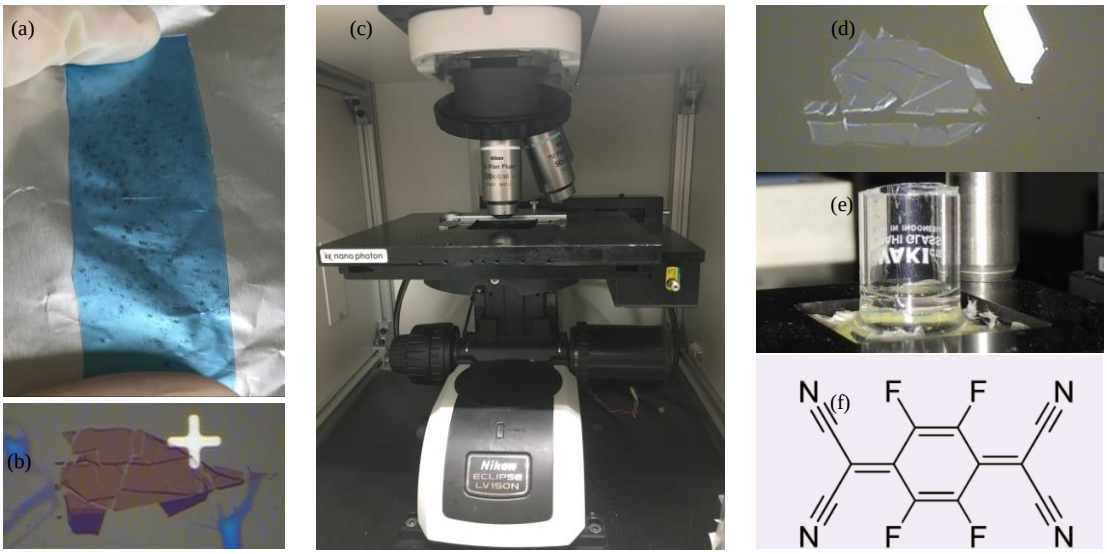

Figure 3.1 Exfoliated MoS_2 using a blue tape (a). 1L WSe_2 on a SiO_2 substrate (b). Raman microscope system (c). 1L MoS_2 on a glass substrate (d). Glass substrate bonded with a glass tube as a liquid reservoir (e). Chemical structure of F_4TCNQ (f).

Monolayer (1L) TMDs (mainly MoS_2 and WSe_2 in this thesis) were mechanically exfoliated from bulk crystal (from hq graphene or SPI) using a blue tape (Nitto) as shown in **Figure 3.1** (a). The exfoliated sample was transferred onto SiO_2/Si substrate (with SiO_2 thickness of 270nm) or Polydimethylsiloxane (PDMS). 1L MoS_2 on the substrate was

identified through optical contrast using an optical microscope equipped in a micro Raman spectroscopy system (Nanophoton) as shown in **Figure 3.1** (c). A 532 nm laser was used to excite the sample, and Peltier cooled CCD equipped with a spectrometer in the Raman spectroscopy system was used to record the Raman and PL spectra.

The samples used in the following chapters 4 and 5 (MoS_2 and WSe_2) were first exfoliated using the Nitto blue tape, and then were transferred on PDMS. The transferred TMDs were identified using optical contrast and confirmed using Raman and PL spectra. The confirmed 1L MoS_2 (WSe_2) flake was transferred on a transparent glass substrate. Finally, a glass tube was bonded with the substrate to compose a liquid reservoir for the following optical measurements in which the samples were immersed in aqueous solutions. Optical images of the 1L TMDs on SiO_2, transparent glass and bound tube are shown in **Figure 3.1** (b) (d) and (e), respectively.

In chapter 6, *p*-type chemical dopant molecule F_4TCNQ (2, 3, 5, 6-Tetrafluoro-7, 7, 8, 8-tetracyanoquinodimethane) (**Figure 3.1** (f)) was used for chemical doping treatment on 1L MoS_2. 1L MoS_2 was exfoliate and transferred on SiO_2 and then F_4TCNQ with a concentration of 0.02 μmol/mL was drop casted on the sample at room temperature.

3.2. Optical measurements

Optical measurements in this thesis mainly consist of two steps: First, the samples were screened via Raman and PL measurements using a commercial micro-spectroscopy system (Nanophoton) to confirm the layer number, and then measurements of PL spectra and decay profiles were conducted using a homebuilt optical setup.

3.2.1. **Raman and PL spectra of monolayer TMDs**

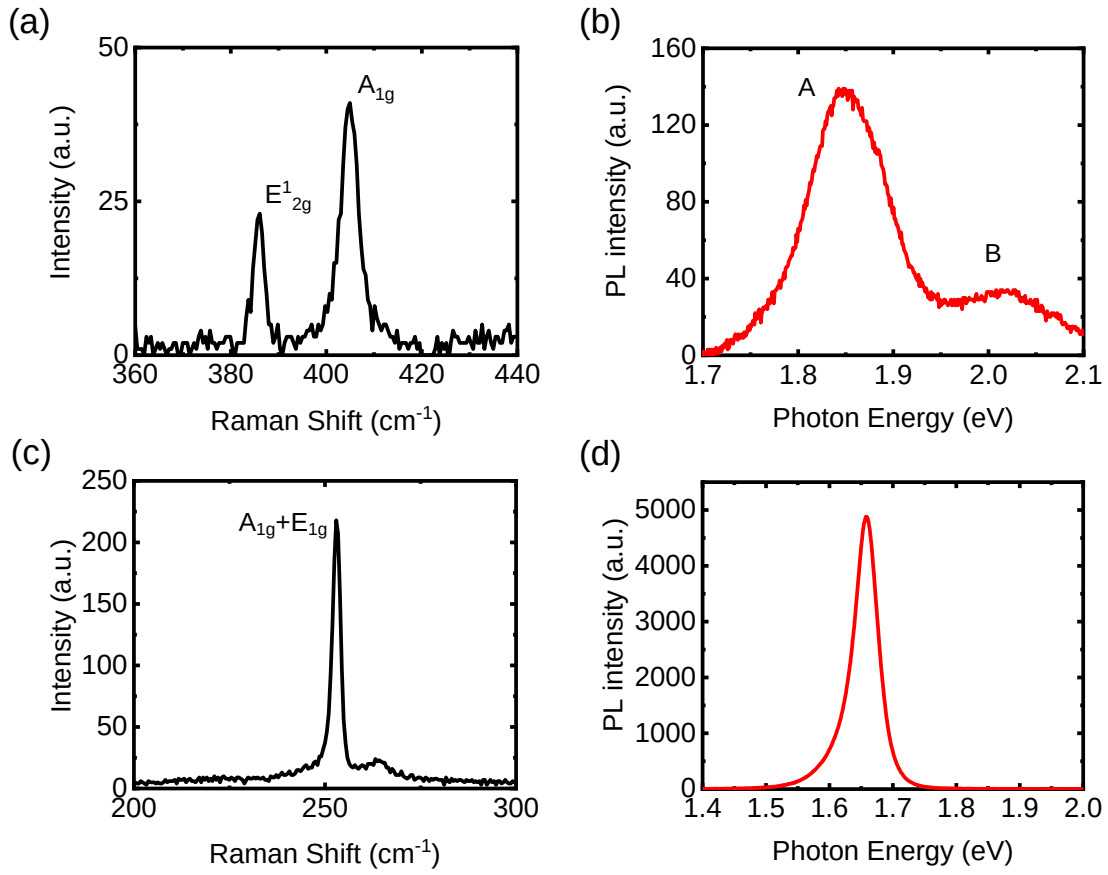

Figure 3.2 Raman (a and c) and PL (b and d) spectra of 1L MoS_2 (a and b) and WSe_2 (b and d) in the Raman spectroscopy system excited using a 532 nm laser. E_g, E^1_{2g} and A_{1g} were in plane and out of plane vibration mode, respectively. A and B indicate A- and B- exciton peaks that are normally observed in as-exfoliated (naturally *n*-doped) 1L MoS_2, respectively.

After identifying the MoS_2 (WSe_2) on SiO_2 or PDMS under the microscope through optical contrast, Raman and PL spectra were used to further confirm the layer number. In the following chapter, before measurements in homebuilt setup, Raman and PL spectra of all the samples are measured using the micro-spectroscopy system using a 532 nm laser

equipped with a high NA lens as shown in **Figure 3.1** (c). The typical PL and Raman spectra of 1L MoS_2 (WSe_2) are shown in **Figure 3.2**. For 1L MoS_2, the difference between in plane (E^1_{2g}) and out of plane (A_{1g}) vibration modes is ~19.4 cm^{-1}, which is a typical value for 1L MoS_2, and the PL peak is at ~1.90 eV.[78,93–96] as shown in **Figure 3.2** (a) and (b). For 1L WSe_2, the typical unseparated in plane (E_g) and out of plane (A_{1g}) vibration modes are near ~251.5 cm^{-1} and the PL peak position is at ~1.67 eV as shown in **Figure 3.2** (b) and (c).

3.2.2. **Optical setup for measurements of TMDs in liquids**

In chapters 4 and 5, 1L MoS_2 (WSe_2) was measured in a homebuilt optical setup as shown in **Figure 3.3** Schematic of homebuilt optical setup for PL and lifetime measurements. A supercontinuum light source and a monochromator were used to obtain the output light with a specific wavelength. In the following chapters 4 and 5, visible light with wavelength of 580 nm was typically used for the measurements. Band-pass and short-pass filters were used to exclude the directly scattered incident light of 580 nm. A high NA (1.45) oil immersion lens was used to collect the emission light from 1L MoS_2 or WSe_2. H_2SO_4 and NaOH were used as pH adjustors to modulate the pH of the aqueous solutions for the measurement in different pH conditions. The sample was first measured in ambient air condition. After dropping distilled water into the reservoir, the sample was measured in a distilled water condition, and then was measured in aqueous solutions with different pH after the pH adjustors were added. Other long-pass filters (633nm or 594 nm edge filter) were used to exclude the directly reflected/scattered incident light from the PL signal during the later measurements in the homebuilt setup. A spectrometer equipped with a liquid nitrogen cooled CCD was used to record the PL spectra. In chapters 4 and

5, Argon gas (99.99%) was used to degas the distilled water to decrease the oxygen concentration in water as shown in **Figure 3.3** Schematic of homebuilt optical setup for PL and lifetime measurements, and a gas flow controller equipped with a flow monitor was used to control the Argon gas flow speed.

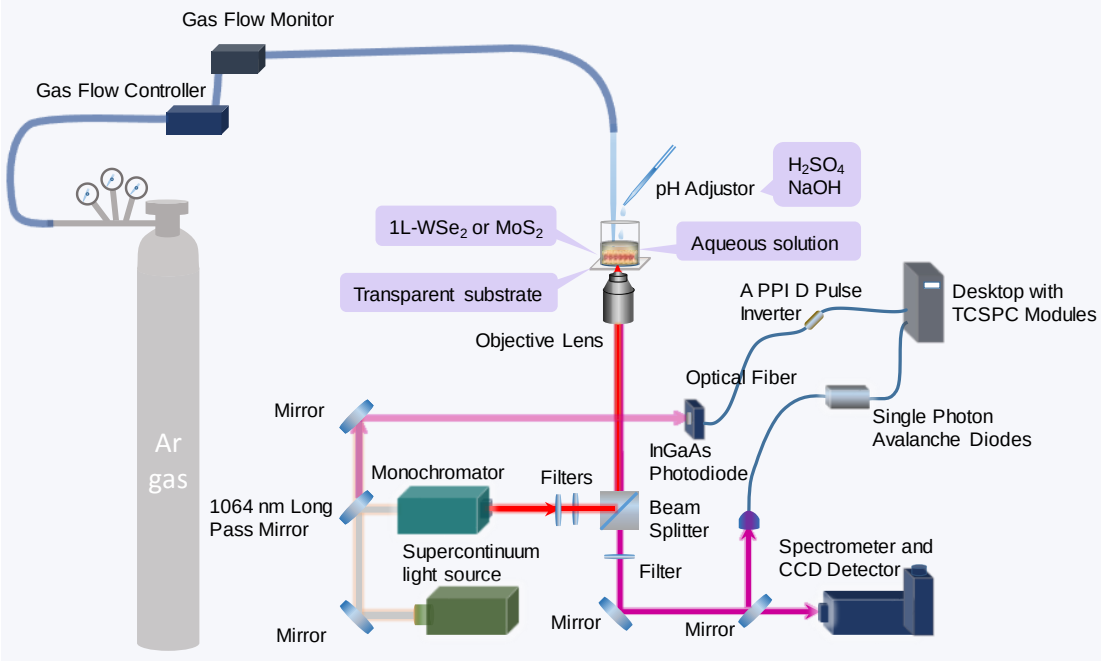

Figure 3.3 Schematic of homebuilt optical setup for PL and lifetime measurements

3.2.3. **Time resolved PL measurements**

Time resolved PL measurements were carried out in the homebuilt optical setup with a supercontinuum light source (pulse duration of ~20 ps and frequency of 40 MHz). As shown in **Figure 3.3**, near infrared pulse (≥1064 nm) from the light source was separated using long pass filter and collected using an high speed InGaAs photodiode and then the polarity of the signal was inverted as a trigger for the time correlated single photon

counting (TCSPC) modular using a passive differential pulse inverter. The optical fiber was used for the light transmission to an avalanche photodiode. A simple schematic of the TCSPC technic is shown in **Figure 3.4**.

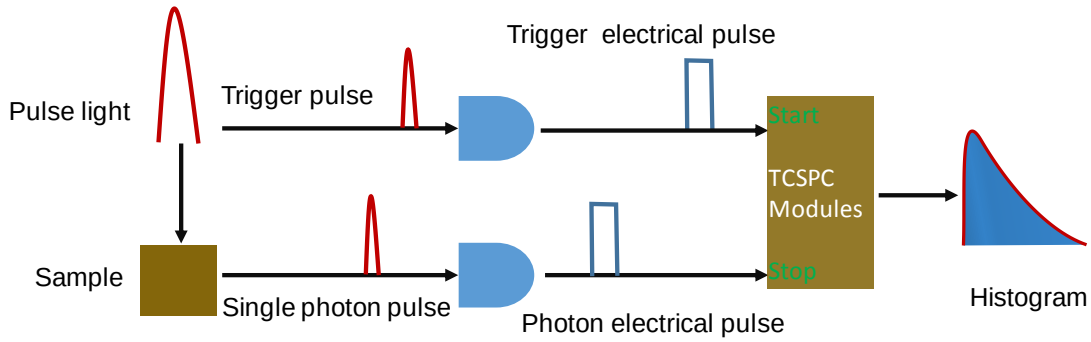

Figure 3.4 Simple schematic of a classic TCSPC measurement.

3.2.4. **Valley polarization measurements**

The valley polarization property measurements were carried out in a homebuilt confocal optical system with a 633 nm He-Ne laser as shown in **Figure 3.5**. A linear polarizer and a quarter wave plate were used to obtain σ^+ circularly polarized excitation light. 633 nm edge filters were used to exclude the directly reflected/scattered laser light from the PL signal. A pin hole was used to get the center signal from the excited spot. A polarizing beam displacer was used to separate the mixed linearly polarized light into two orthogonally polarized beams. A depolarizer was used to remove the polarization of the two beams, and focus lens was used to generate an image of two separated spots at the entrance the slit plane of the spectrometer. Finally, a spectrograph equipped with a liquid nitrogen cooled CCD detector was used to record the PL spectra of σ^+ and σ^- circularly polarized emission components from the sample at the same time. Different

regions of the CCD plane were used to detect the polarization-separated signals simultaneously.

In chapter 6, valley polarization mapping methods was used to obtain the PL property of the sample at 15K. Liquid Helium cooled cryostat was used for the low temperature measurements. The cryostat was fixed with a *xy* motored stage, which can be controlled using a software (Winspec with a fast mapping function) for the spatial mapping measurement. The whole sample was excited point by point through the scanning of the stage, and the PL signals from more than 700 points were collected. Finally, MATLAB (Mathworks) was used to generate the PL and valley polarization images from the measured data at all the points for further data analysis.

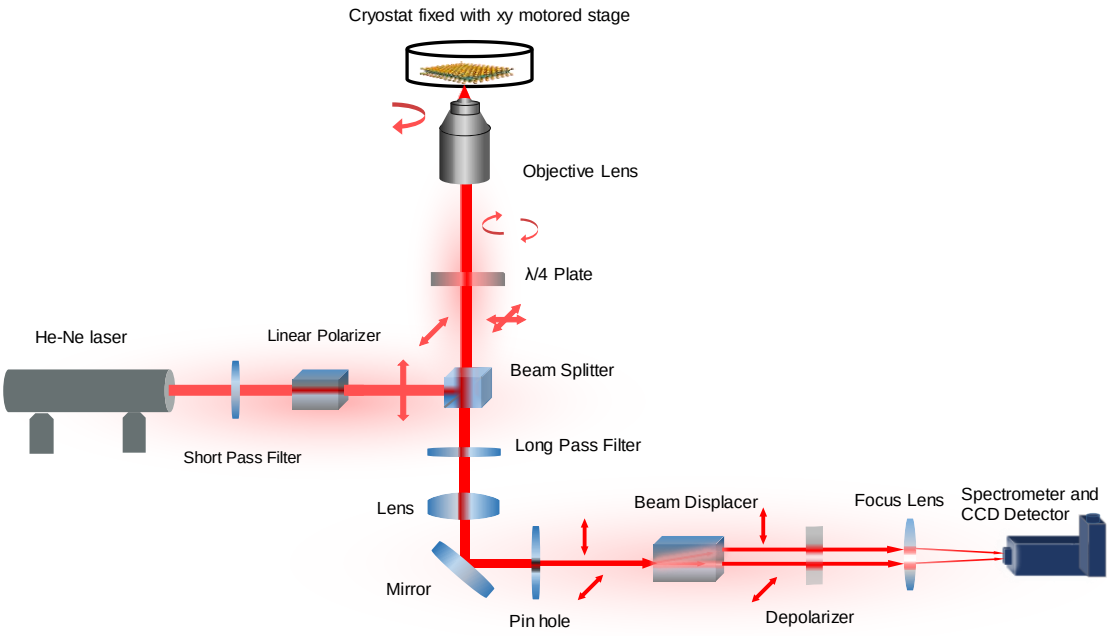

Figure 3.5 Schematic of the optical setup for valley polarization measurements at low temperature.

Chapter 4. PL property of monolayer transition metal dichalcogenide in aqueous solutions

4.1. Introduction

Because of their unique optical and electrical properties, 1L TMDs show high potential in future electronic and optoelectronic applications, such as phototransistors,[54] light emitting devices[47] and solar cells.[63] The optical and electronic properties are easily affected by many external effects or methods such as electrical gating,[86] chemical treatment[48] and applying magnetic field,[91] because of their 2D natures with a large specific surface area. Among these, the chemical treatment is one of the facile and effective methods to modify and control their properties of 1L TMDs. Recently, modulation of optical and electrical properties were demonstrated using various methods, such as covalent bonding,[97,98] chemisorption and physisorption doping,[48,99,100] electrostatic doping,[101] and chemical doping methods.[102] These studies showed that the optical and electrical properties of 1L TMDs could be easily modulated through the electron extraction form or injection into 1L TMDs via surface charge transfer[100] and/or by defect passivation effects.[49,98] Furthermore, water or oxygen molecules are easily absorbed on low dimensional materials such as carbon nanotube, graphene and MoS_2 in ambient air or humid conditions, which strongly affects their optical or electronic properties.[99,103,104]

As one of the typical environments for device fabrication or application based on 2D materials, ambient air, is full of water and oxygen molecules. The effects of oxygen and

water are inevitable for 2D materials because of the very large specific surface area. Since the various electrochemical phenomena occurring at the interfaces of aqueous solutions and 1L TMDs might considerably affect their physical/chemical properties and usefulness of 1L TMDs in future applications, it is important to clarify the impact of the surface electrochemical phenomena on their optical properties. 1L TMDs in the environment of aqueous solution is appropriate system to study these effects; however, knowledge of optical properties of 1L TMDs in the aqueous solution condition is still limited. Here, the PL properties of 1L MoS_2 in ambient air and aqueous solutions with various pH were studied in this chapter.

4.2. PL property of monolayer MoS_2 in air and aqueous solutions

The PL properties in ambient air and water condition were studied. The 1L MoS_2 was transferred on a transparent substrate which was bound with a glass tube later for keeping aqueous solution, as shown in **Figure 4.1** (a) and (b). The measurements were carried out in ambient air and then in water as shown in **Figure 4.1** (b). **Figure 4.1** (c) shows the PL spectra of 1L MoS_2 in air and water condition. After immersed into distilled water, the PL intensity dramatically increased almost 5 times. Moreover, the PL spectral shape of normalized PL spectra also show considerable difference between the air and water condition as shown in **Figure 4.1** (c) and (d). To further understand these differences, the normalized PL spectra in air and water were decomposed into trion (X^-, ~1.85 eV) and exciton (X, ~1.90 eV) peaks using the peak fitting procedures, as shown in **Figure 4.1** (e) and (f).[48] The spectral fitted results showed that the trion peak is the main component of PL spectrum in ambient air, whereas the exciton became dominant in

water condition, which is consistent with previous reports that 1L MoS_2 is an *n*-doped material. The PL intensity ratio of exciton and trion (X/X^-) increased in the water condition in comparison with that in ambient air condition, suggests that the trion formation is suppressed, and the carrier density dramatically reduced after the sample was immersed into water.

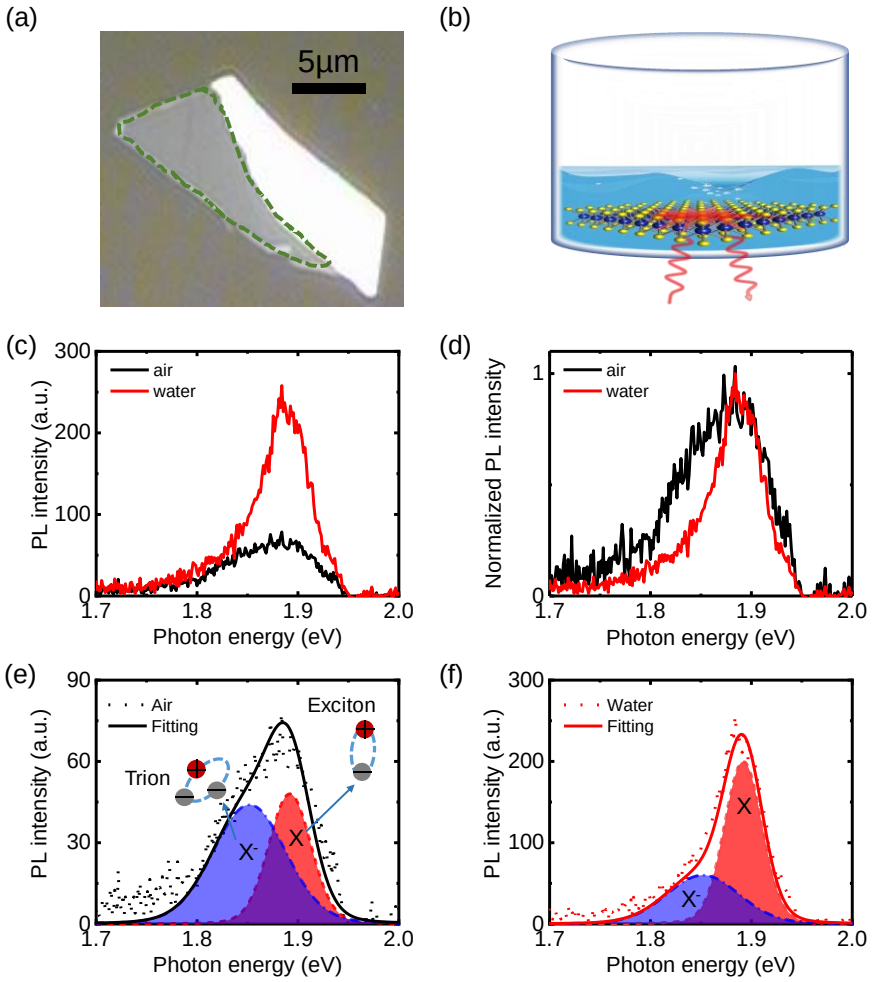

Figure 4.1 1L MoS_2 on transparent substrate (a). Simple schematic of 1L MoS_2 in aqueous solution (b). PL properties of 1L 1L MoS_2 in air and water, (c): PL spectra, (d): normalized PL spectra, (e) and (f): decomposition of normalized PL in air and water, respectively. Reproduced in part with permission from Ref.[105]. © 2018 ACS.

4.3. Oxygen effect on the PL property of monolayer MoS_2 in aqueous solutions

The oxygen effect in water might be one of the reasons for the considerable modulation of PL intensity and carrier density of 1L MoS_2 after immersing sample into the water because the oxygen centration in distilled water is strongly different with ambient air. To confirm this, 1L MoS_2 was immersed in a degassed water condition that Argon gas was used to bubble the water to decrease the dissolved oxygen concentration in distilled water. The PL spectra were measured in these conditions.

Figure 4.1 (a) shows the PL spectra of 1L MoS_2 in air, distilled water, and degassed water condition. The PL intensity of 1L MoS_2 dramatically decreased in the degassed water after bubbling the distilled water using Argon gas for 30 minutes, and this is even lower than the original PL intensity in ambient air. Noted that the normalized PL spectra as shown in **Figure 4.1 (**b) showed that the spectral shape recovered back to the original air condition after the gas bubbling. **Figure 4.1** (c), (d) and (e) show the decomposition of PL spectra in air, distilled water, and degassed water condition, respectively.[105] The spectral shape decomposition results suggested that the exciton and trion PL intensity ratio significantly increased after the sample immersed into distilled water, and decreased once again in degassed water with a continuous Argon gas bubbling, which suggests that the trion formation is suppressed in distilled water and increased again in degassed water condition. These results showed that the oxygen in water plays an important role in the exciton/trion formation process which induced in the modulation of PL intensity and spectral shape, which can be explained by the effect of oxygen in water redox at the interface of 1L MoS_2 and liquid. Furthermore, it is expected that this electrochemical

effect could be easily modulated by changing the pH of the solution, in which the redox potential strongly depends on the pH condition.

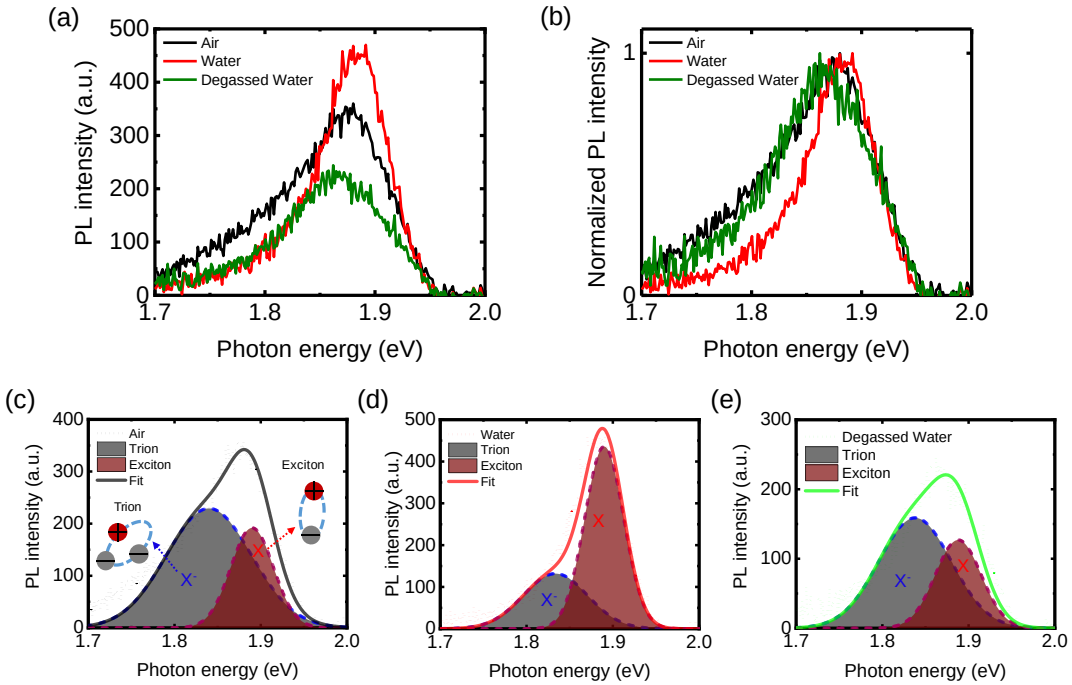

Figure 4.2 PL spectra of 1L MoS_2 in ambient air (black), distilled water (red) and degassed water (green) (a). Normalized PL spectra for comparison (b). The decomposition of PL spectra with trion (X^-) and exciton (X) in air (c), water (d) and degassed water (e).

4.4. pH effect on the PL property of monolayer MoS_2 in aqueous solutions

As discussed above, it is necessary to confirm the effects of pH on the PL properties after the oxygen effect was observed in distilled water. The H_2SO_4 and NaOH were used as the pH adjustors adding into water for changing the pH of the solution. The PL spectra of 1L MoS_2 was measured in different pH from acidic (pH~3) to basic (pH~12) condition.

Figure 4.3 shows the PL spectra and integrated PL intensity in various pH conditions. As shown in **Figure 4.3 (**a) and (b), the PL intensity strongly depended on the pH of solution. In the lower pH conditions, the PL intensity considerably increased whereas the PL intensity decreased in higher pH conditions. The integrated PL intensity in low pH (acidic) condition (pH~3) showed almost one order larger than that in high pH (basic) condition (pH~12) as shown in **Figure 4.3** (c). To further understand these pH dependent behaviors clearly, the PL spectra in various PH conditions were normalized as shown in **Figure 4.4**. The considerable difference of PL spectra between the basic condition and acidic condition were clearly observed, however, the almost no differences in lower pH condition (pH $<$ 7) was observed. The pH dependent spectral shape of PL spectra mainly comes from the exciton/trion intensity ratio that induced by the change of carrier density.

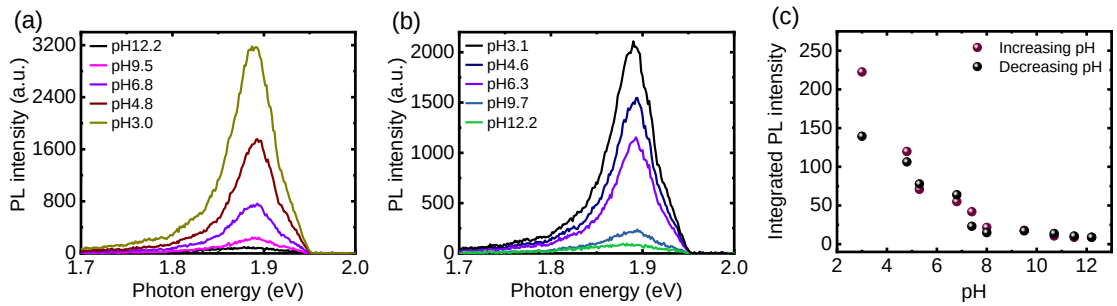

Figure 4.3 PL spectra of 1L MoS_2 in aqueous solution with increasing pH (a), and deceasing pH (b). Integrated PL intensity as a function of pH from the data of (a) and (b).

The carrier density is evaluated from the integrated intensity ratio of exciton and trion peak corresponding to their population according to the mass action law, as follows:

$$\frac{N_X n_e}{N_{X^-}} = \left(\frac{4m_X m_e}{\pi\hbar^2 m_{X^-}}\right) k_B T e^{-\frac{E_{tr}}{k_B T}} \quad 4.1$$

where the n_e, N_X, and N_{X^-} are the electron density, exciton and trion population respectively, and m_e, m_X, m_{X^-} are the effective mass of electron, exciton and trion, where k_B, T, and E_{tr} are the Boltzmann constant, temperature and trion binding energy, respectively[48,86] Normally, the effective radiative decay rate of the exciton in 1L TMDs is almost one order of magnitude larger than that of the trion.[48,83] With this assumption, n_e is evaluated to be on the order of ~10^{12} cm^{-2} in acidic condition (pH < ~7) and ~10^{13} cm^{-2} in basic condition (pH > ~8). The higher PL intensity in the acidic condition can be explained, since the lower electron density reduced the exciton carrier collision rate which induced in a lower nonradiative relaxation rate into the trion formation from exciton in the condition of pH < ~7, and the exciton PL intensity is strongly enhanced.

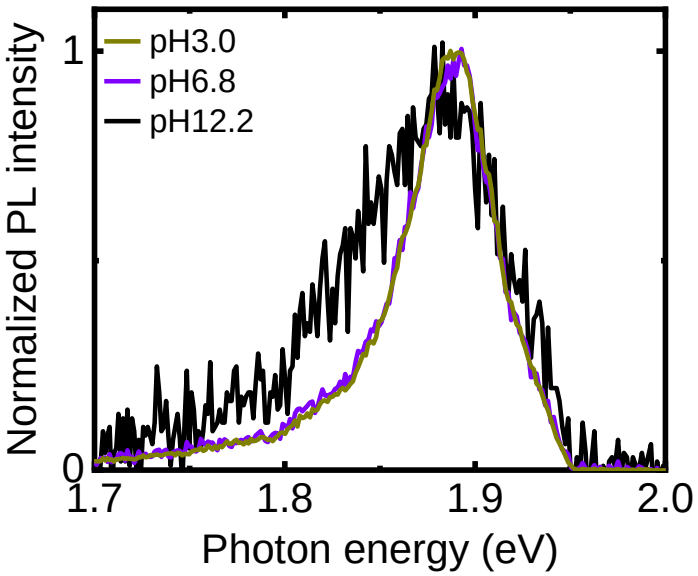

Figure 4.4 Normalized PL spectra of 1L MoS_2 in acid, neutral and basic conditions.

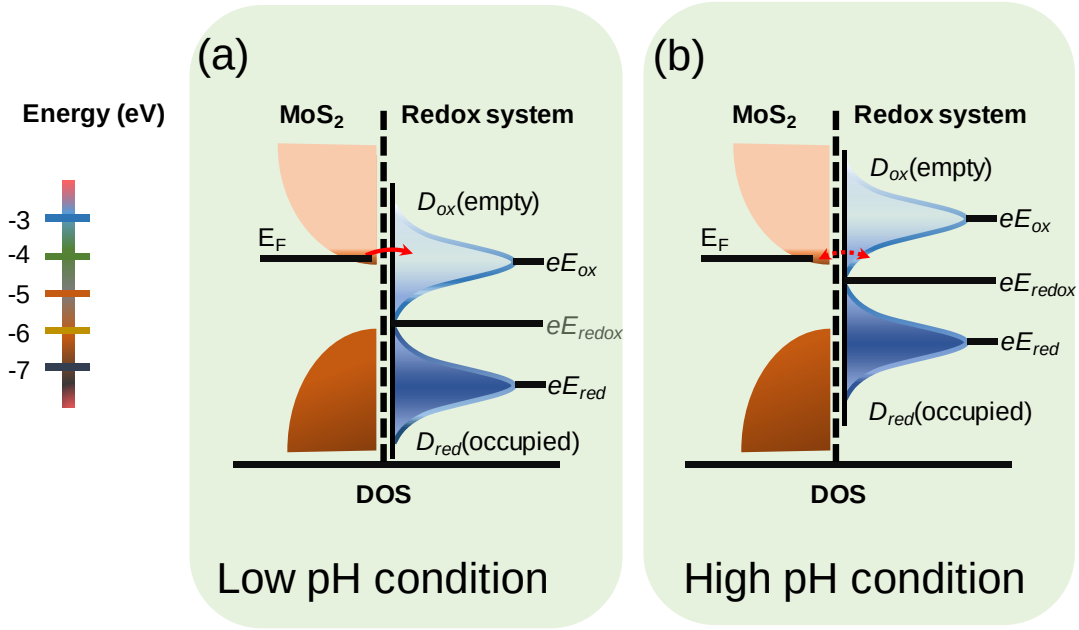

Figure 4.5 Electron transfer mechanisms with the Marcus−Gerischer (M-G) model: at low pH (a) and at high pH (b). Left, density of states (DOS) around the band edge of MoS_2 vs vacuum level. The conduction and valence bands of 1L MoS_2 with a direct band gap of ~1.9 eV. Right, DOS of the O_2/H_2O redox system. eE_{redox} is the energy of solution at which oxidizing and reducing species are equal, $D_{ox} = D_{red}$, where D is the DOS. eE_{ox} and eE_{red} are the mean energies for unoccupied and occupied states respectively. The red (a) solid and (b) dashed arrows indicate the direction of charge transfer.

To understand the mechanism of this electrochemical effect on the PL properties of 1L MoS_2, Marcus-Gerischer (M-G) model was used to understand the possible mechanism.[106] The M-G model has been applied to explain the interface reaction between a semiconductor or metal and a water redox system in previous reports.[107–109] In a standard atmospheric pressure at room temperature, oxygen molecules can be dissolves into water

with an amount of 9-10 ppm. After the sample was immersed into water, the surface charge transfer may occur from 1L MoS_2 into the O_2/H_2O redox system, as follows.

$$O_2(g) + 4H^+ + 4e^-(MoS_2) \rightleftharpoons 2H_2O \qquad 4.2$$

According to the M-G theory, molecules or ions in the aqueous solution have discrete energy levels that fluctuate with time.[110] Then, the electrons transfer occurs from the occupied states of MoS_2 to the unoccupied states of O_2/H_2O redox system if the Fermi energy or chemical potential of 1L MoS_2 is higher than the redox potential of the redox system, where the reverse transfer will occur while the potential levels are opposite as shown in **Figure 4.5**. As a result of the electron transfer, the O_2/H_2O redox system is regarded as the electron acceptor or donor depending on the direction of electron transfer which is determined by the relative value between the Fermi Level and the redox potential. According to the Nernst equation,[111] the potential *E* is described by:

$$E = E^0 - \frac{RT}{zF}\ln Q \qquad 4.3$$

where *Q* is the reaction quotient, and *R*, *T* and *F* is the ideal gas constant, temperature, and faraday constant, respectively. The E^0 is the standard potential and *z* is the mole of transferred electrons as shown in Equation 4.2, in which *z* is 4. In a perfect gas condition, Nernst equation is given by:

$$E = E^0 - \frac{RT}{zF}\ln\frac{P}{P^0} \qquad 4.4$$

and the redox potential of a O_2/H_2O redox system can be determined as:[108,110,111]

$$E_{\text{redox}} = \mu_{\text{e(SHE)}} + E^0_{\text{redox}} - \frac{2.303RT}{nF}\left[\log\left(p_{O_2}\right) - 4\text{pH}\right] \qquad 4.5$$

in an slightly acidic condition, whereas in the basic condition it can be written as:[108,110,111]

$$E_{\text{redox}} = \mu_{\text{e(SHE)}} + E^{0}_{\text{redox}} - \frac{2.303RT}{nF}\left[4\text{pOH} + \log\left(p_{O_2}\right)\right] \qquad 4.6$$

The $\mu_{e(\text{SHE})}$ is the electrochemical potential of an electron in the stand hydrogen electrode (SHE) relative to the vacuum level which is about -4.44 V; E^{0}_{redox} is the stand electrode potential of the reaction relative to the vacuum which is different for acidic (~-1.229 V) and basic (~-0.401 V) condition. *n* or *z* is the mole of transferred electrons as shown in Equation 4.2, in which *n* or *z* is 4; and $\frac{2.303RT}{nF} = \frac{0.059}{4}$ V, here; p_{O_2} is the partial pressure at room temperature that is ~0.21 bar and $\text{pH} + \text{pOH}=14$.[108,110]

At room temperature, the redox potential strongly depends on the dissolved oxygen and pH value of the solution. Without any dissolved oxygen modulation at room temperature, E_{redox} is estimated as ~-5.27 V at pH 6.5. The VBM and CBM is about -5.27 eV and -4.1 eV relative to the vacuum level.[112,113] The Fermi level is near the CBM because 1L MoS_2 is the natural heavily *n*-doped material. After immersing of 1L MoS_2 into distilled water with a pH of ~6.5 that redox potential lies below the Fermi level of 1L MoS_2, the difference between the Fermi level and eE_{redox} gives a driving force for the electrons transferring from MoS_2 into the surrounding redox system until the equilibrium reached. Thus, the trion formation is strongly suppressed and the exciton PL intensity increases (**Figure 4.3**). When the pH is tuned to lower, the redox potential shifts down from -5.27 at pH 6.5 to -5.66 in pH 0. The increased difference between the Fermi level and eE_{redox} extracts more electrons from 1L MoS_2, which induced in a further suppression of trion formation because of the reduced carrier density in 1L MoS_2 as shown in **Figure 4.5** (a) and **Figure 4.3**. In contrast, as shown in **Figure 4.5** (b) and

Figure 4.3, when the pH is tuned to basic condition, the redox potential increased from -5.27 V (pH 6.5) to -4.83 V (pH 14) and the electron extraction from 1L MoS_2 is suppressed or transferred oppositely. This opposite electrons transfer results in a trion formation increase because of the increased carrier density in 1L MoS_2 and a further spectral shape modulation (**Figure 4.4)**.

Furthermore, the M-G theory also can be used to explain the oxygen effect in water condition. During the Argon gas bubbling, the oxygen concentration in distilled water dramatically decreased, and the redox potential is lifted. Thus, difference between the redox potential and Fermi level of 1L MoS_2 became smaller and electron extraction from 1L MoS_2 is suppressed or oppositely injected into 1L MoS_2 which result in a modulation of both PL intensity and spectral shape (**Figure 4.2)**.

4.5. Time resolved PL of monolayer MoS_2 in aqueous solutions

As discussed above, the changes of PL intensity and spectral shape with increasing or decreasing pH can be understood through M-G model. It is also noticed that, in the low pH condition, the PL intensity enhanced a lot whereas the spectral shape almost does not show considerable difference. This suggests that the PL intensity enhancement under low pH conditions might be not only attributable to the reduced exciton decay rate into trion states due to the decreased carrier density. To further understand this phenomenon, the time resolved PL decay measurements were carried out in aqueous solutions with various pH as shown in the **Figure 4.6**. The time resolved PL profile became slower in low pH condition, whereas the lifetime became faster in the high pH condition. For better comparison, the time resolved PL profiles were fitted using convolutions of the

biexponential function $I(t) = C_1 \exp(-t/\tau_1) + C_2 \exp(-t/\tau_2)$ and the instrumental response function (IRF). The effective decay time $\langle\tau\rangle$ was obtained using the relation defined as, $\langle\tau\rangle = (C_1\tau_1 + C_2\tau_2)/(C_1 + C_2)$.

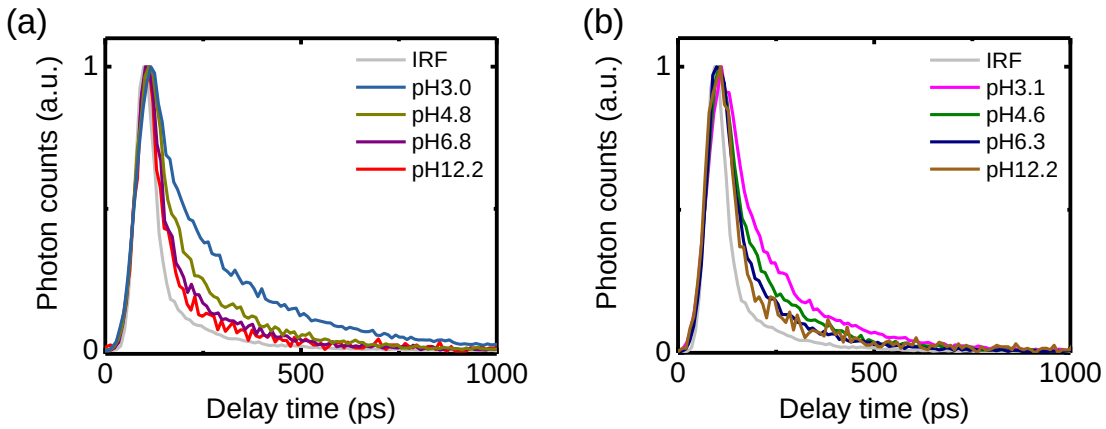

Figure 4.6 Time resolved PL of 1L MoS_2 with increasing pH (a) and decreasing (b) the pH of aqueous solutions.

Figure 4.7 (a) shows the effective life time as a function of pH of solution. The effective lifetime dramatically increased at low pH condition, whereas decreased at high pH conditions and this result can be reproduced in both direction decreasing and increasing pH. **Figure 4.7 (**b) shows the correlation between the integrated PL intensity and effective lifetime. The strongly correlation between pH and effective lifetime suggests that the observed PL intensity change in low pH conditions is mainly attributable to the changes of the PL decay time. This suggests that the modulation of pH strongly affects the nonradiative relaxation processes in 1L-MoS_2 because the PL decay is dominated by non-radiative relaxation pathways in the as-prepared 1L-MoS_2 with very low PL quantum yield.[49,114] Note that the effective decay time at pH higher than 9 reached to a limitation of our detection system (~20 ps). The increased effective decay time at low

pH condition (< pH ~7) does not change the PL spectral shape (shown in **Figure 4.4**), which means the negligible change in intensity ratio of X and X^-. This implies that the nonradiative recombination rate of excitons still reduced when the trion formation rate was unchanged at low pH conditions. This is similar with the previous reports that the PL can be brightened through the defect passivation by the super acid treatment.[49] The energy level of sulfur vacancy lies blow the conduction band edge of ~0.45-0.7 eV,[115–117] and it may be partially passivated by H^+ ions whose concentration is extremely high under low pH conditions.

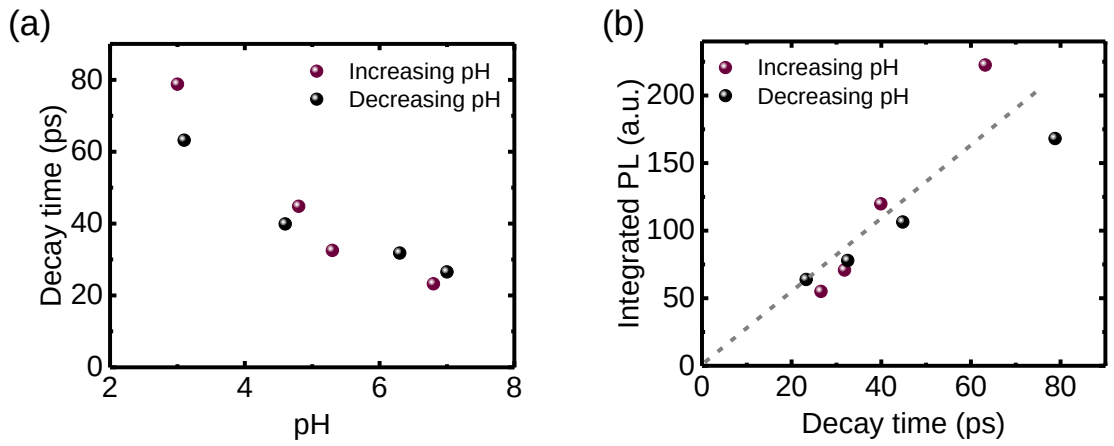

Figure 4.7 Effective decay time of 1L MoS_2 under different pH (a) and the effective decay time plotted as a function of the integrated PL intensities (b) with increasing and decreasing pH of aqueous solution.

4.6. Chapter summary

In this chapter, the PL properties of mechanically exfoliated 1L MoS_2 was investigated in ambient air, distilled water, degassed water and aqueous solutions with various pH. The PL properties were considerably changed after immersing 1L MoS_2 into

distilled water. Furthermore, the pH in aqueous solutions strongly affected the PL intensity, spectral shape and effective decay time. Both the PL intensity and effective lifetime increased as the pH of the aqueous solution decreased from basic to acidic condition, and the same results were obtained from acidic to basic condition. These strongly pH dependent PL properties can be understood that the carrier density in 1L MoS_2 was considerably modulated through electrochemical reactions at the interface of 1L MoS_2 and an O_2/H_2O redox system because of the pH dependent electrochemical potential. The increased exciton lifetime and the unchanged PL spectral shape at low pH conditions (< pH ~7) suggests that the passivation of local defects with H^+ ions may also contributes to the PL intensity enhancement when the concentration of H^+ is high at the lower pH conditions. These experimentally observed results and their mechanism might provide a new insight into the effects at the interface of the atomically thin semiconductors and oxygen/water redox system, which are important and unavoidable when the 1L material is in ambient air with finite humidity and in aqueous solutions.

Chapter 5. Photostability of monolayer transition metal dichalcogenide in aqueous solutions

5.1. Introduction

In the last chapter, it was observed that PL properties of 1L MoS_2 were strongly modified in aqueous solutions because of the electrochemical reactions at the interface of atomically thin TMDs and oxygen/water redox system, which gave us an insight into the environmental effect on the PL properties of 1L TMDs in real applications. Meanwhile, the electrochemical etching[118,119] and oxidation reactions[120,121] of atomically thin TMDs under the photoirradiation, ambient air and ozone exposure conditions were also reported. As introduced, thin layer TMDs showed high potential in applications of phototransistors,[122,123] photodetectors,[57] light-emitting devices,[47,60] light modulators,[124] and solar cells[62] because of their unique electronic and optical properties. With consideration of realistic application environment such as ambient air and wet conditions, it is important and necessary to give a deep understanding of the influence of these interface reactions between oxygen, water and 1L TMDs on their stability as well as physical or chemical properties of 1L TMDs. However, until now, knowledge of the stability of 1L TMDs under such conditions is still limited. Here, the surface interactions on the photostability of 1L TMDs under a continuous light irradiation condition by monitoring the PL properties will be studied. The findings in this chapter may give us an important understanding of surface environmental effect on the sample fabrication, storage, and future applications.

5.2. Optical property of monolayer MoS_2 and WSe_2 with light irradiation

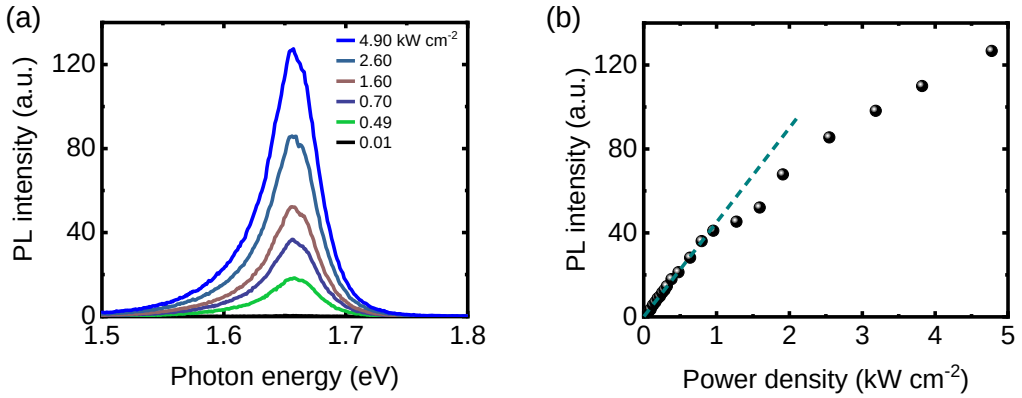

Figure 5.1 Power dependent PL spectra and PL intensity of 1L WSe_2 under a supercontinuum laser irradiation with a typical viable wavelength of 580 nm. Reproduced in part with permission from Ref.[125]. © 2019 ACS.

The photostability of PL properties of two typical TMDs (MoS_2 and WSe_2) were investigated by using a supercontinuum light source with a typical visible wavelength of 580 nm. Other different visible lights with a wavelength of 532 nm and 594 nm were also used to compare the wavelength effects. The experimental condition of light intensity (800 W cm^{-2}) was kept in the linear power dependence region of PL intensity as shown in **Figure 5.1** (a) and (b), and the same power density was used for the PL measurements.[125] The PL measurements were performed at regular intervals (5 min) with a signal acquisition time of 5 seconds.

Before the photostability measurement, the exfoliated 1L TMDs were confirmed using a microscope with a Raman system whose details have been introduced in Chapter

3. The optical images and PL spectra of 1L TMDs on transparent glass substrates under a 532 nm semiconductor excitation laser are shown in **Figure 5.2.** The regions indicated by the orange dotted curve correspond to the monolayer parts.

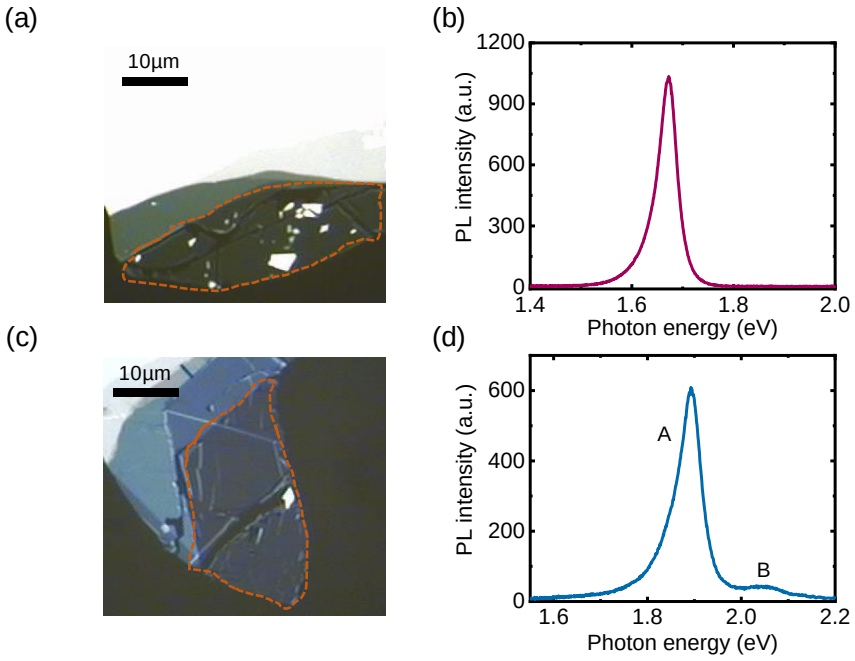

Figure 5.2 Optical images and PL spectra of 1L TMDs on transparent glass substrates. Optical image (a) and PL spectrum (b) of 1L WSe_2. Optical image (c) and PL spectrum (d) of 1L-MoS_2.

5.2.1. PL of monolayer MoS_2 and WSe_2 under with irradiation in ambient air

The experiments for the photostability property was first carried out in ambient air, corresponding to the most typical environment for devices application. **Figure 5.3 s**hows the PL spectra and PL intensity at different light irradiation time. The PL intensity of 1L WSe_2 showed a slightly decrease within ~200 minutes, whereas 1L MoS_2 showed a negligible change in PL intensity as shown in **Figure 5.3** (a) and (d). Because 1L WSe_2

and MoS_2 at 580 nm show a similar order of optical absorption coefficient (1×10^5 to 2×10^5 cm^{-1}),[126,127] the similar photogenerated number of electron and hole in 1L WSe_2 and MoS_2 by the photo irradiation was expected. These results suggested that the photostability of 1L WSe_2 is slightly lower than that of MoS_2 under the photoirradiation in ambient air. The normalized PL spectra showed an undetectable shape change in both 1L WSe_2 and 1L MoS_2, as shown in **Figure 5.3** (b) and (e), which implies that the exciton and trion ratio of both 1L WSe_2 and 1L MoS_2 did not change during the photoirradiation. The time dependent PL intensity as shown in **Figure 5.3** (c) and (f) clear shows the PL stability of 1L WSe_2 and MoS_2 at different time. Thus, the PL properties including their intensity could be used to evaluate the photostability of monolayer material.

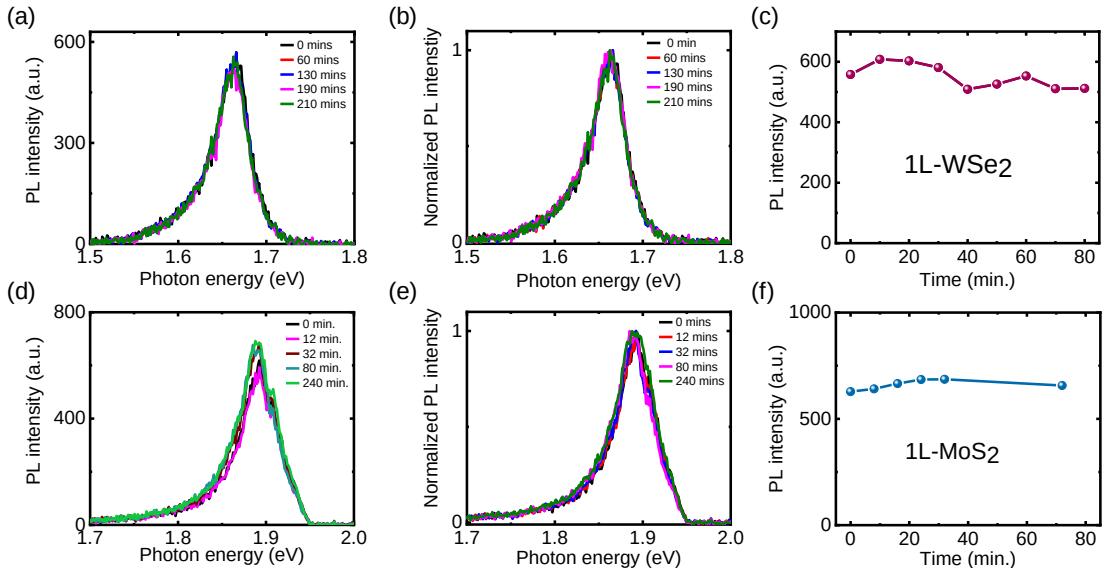

Figure 5.3 Time dependent PL spectra and PL intensity. PL spectra (a) and (d), normalized PL spectral shape (b) and (e) of 1L WSe_2 and MoS_2 at different time. Time dependent PL intensity of 1L WSe_2 (c) and MoS_2 (f), respectively.

5.2.2. PL of monolayer MoS_2 and WSe_2 with light irradiation in water

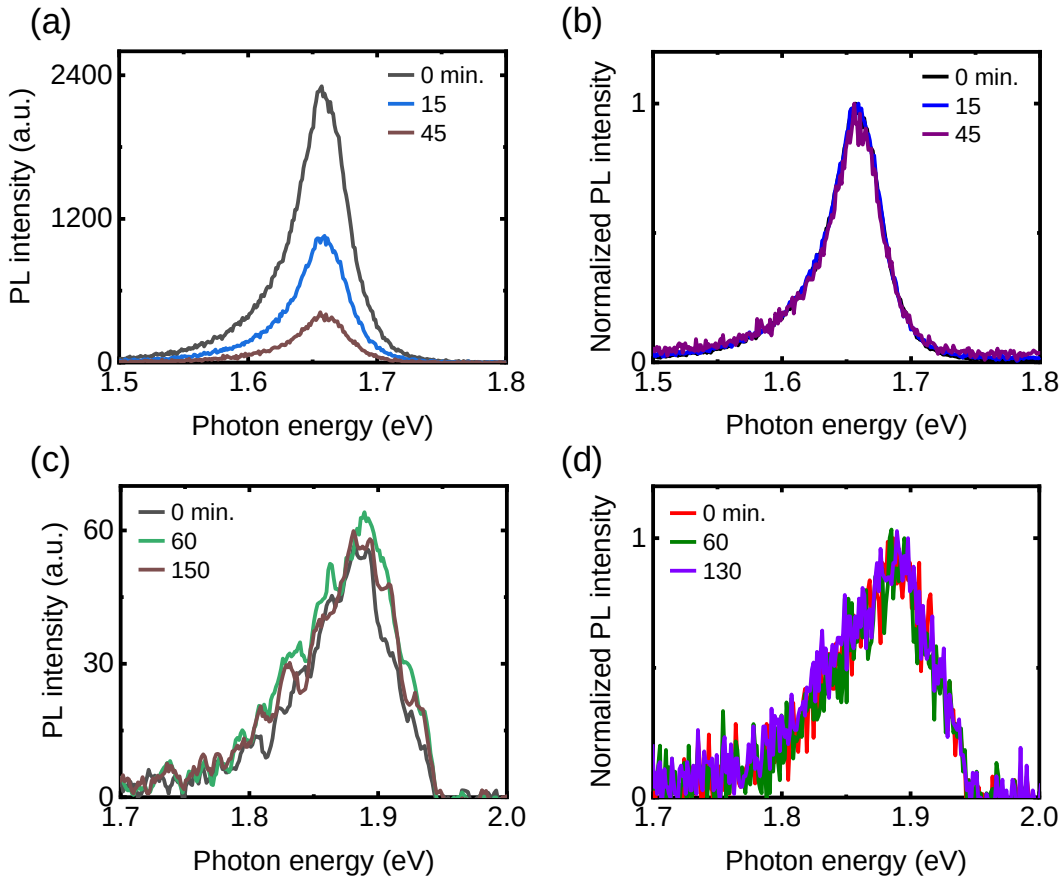

Figure 5.4 PL spectra and normalized PL spectra of 1L WSe_2 (a) and (b), and MoS_2 (c) and (d) in distilled water.

As discussed in the previous chapter, the properties of 1L TMDs are easily affected by the electrochemical effects of oxygen and water at the interface of 1L TMDs and environment with ambient air or other liquid. For the realistic applications of photodetectors, sensors and catalysts, it is important to understand the photostability of 1L TMDs in various environment including liquid or solutions. The aqueous solution is

one of the appropriate platforms for studying these interface effects. The photostability of 1L TMDs in distilled water under light irradiation was investigated, where water and the dissolved oxygen molecules are adsorbed onto the surface of TMDs and electrochemical effects became important.

Figure 5.4 (a) and (c) show PL spectra of 1L WSe_2 and MoS_2 in distilled water during photoirradiation, respectively, and the normalized PL spectra are shown in **Figure 5.4** (b) and (d). The PL intensity of 1L WSe_2 in distilled water gradually decreased within 60 minutes under a continuous light irradiation with a power density of 800 W cm^{-2}, whereas the PL intensity of 1L MoS_2 showed a negligible change within 150 minutes, which suggests that the photostability of 1L MoS_2 is much more stable in distilled water in comparison with 1L WSe_2. The normalized PL spectra showed that the spectral shape of both WSe_2 and MoS_2 did not have any spectral shape changes during the irradiation time, which excludes the effects of carrier density modulation during the photoirradiation.

To further understand the observed results of 1L WSe_2, the PL line mapping method was used to evaluate the photostability by laser irradiation of 532 nm. As shown in **Figure 5.5** (a), the optical image of 1L WSe_2 before the light irradiation in water showed a complete shape, whereas the irradiated point in the center of sample was broken after the irradiation. After removing the sample from distilled water and drying in ambient air, the broken part in the center of 1L WSe_2 was clearly seen as shown in **Figure 5.5** (a). The PL mappingS in **Figure 5.5** (b) strongly support the observed results of optical images and the PL became completely dark in the irradiated part after the continuous light irradiation. **Figure 5.5** (c) showed that after the PL intensity decreased to 0 at the spot after the light irradiation. This darkened PL intensity keeps same after the water was

removed and 1L WSe_2 was exposed in ambient air again. Thus, it is concluded that the photoinduced PL intensity decrease mainly comes from the photoinduced degradation or decomposition of 1L WSe_2, which means that 1L WSe_2 is easily photodegraded in distilled water, whereas 1L MoS_2 is much more stable and hardly degraded.

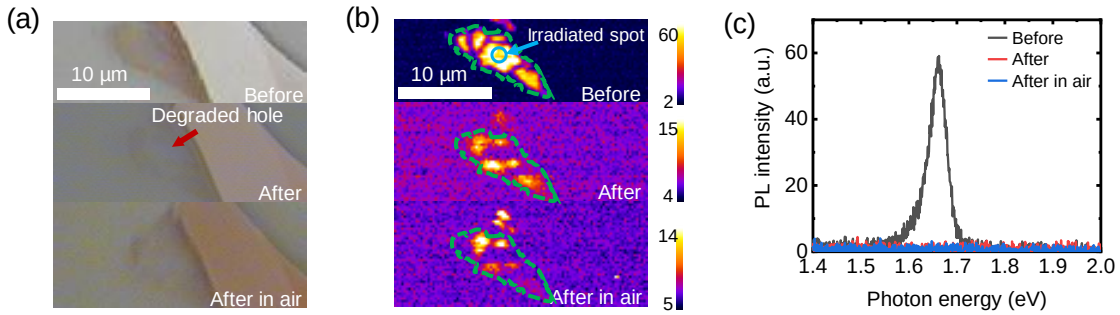

Figure 5.5 Optical images (a) and PL mappings (b) before and after the laser irradiation of 1L-WSe_2. (c) PL spectra measured at the irradiated spot.

To elucidate the mechanism of degradation and considerable difference between 1L WSe_2 and 1L MoS_2, the O_2/H_2O redox couple and electrochemical reaction at the interface between 1L TMDs and aqueous solution were considered. The O_2/H_2O molecules absorbed onto 1L TMDs and photogenerated electrons or holes might be the main factors for the degradation of 1L TMDs in the O_2/H_2O. Photogenerated holes (h^+) could facilitate the oxidation of compound semiconductors (AB) and destruct their original structure,[128] as follows,

$$AB + zh^+ + solv \rightarrow A(oxidation) + B^{z+} \cdot solv \qquad 5.1$$

where A and B are the transition metal and chalcogen atoms that compose the semiconductors. z is the number of holes and solv means solvent.

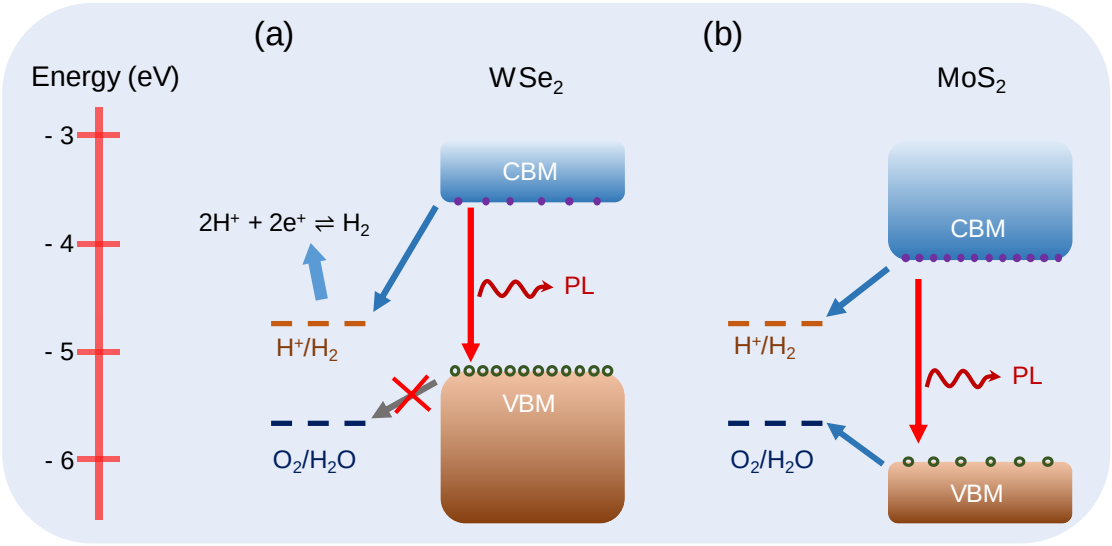

Figure 5.6 Band alignment of 1L WSe_2 (a) and 1L MoS_2 (b) with the water redox potential.

Considering the effects of the photoinduced electron or hole, the band alignment of 1L TMDs and water redox system is important. Depending on the material, the band alignment of semiconductors with oxidation/reduction potentials of O_2/H_2O is different as shown in **Figure 5.6**. The CBM of 1L WSe_2 is near -3.6 eV, which lies above the H^+/H_2 reduction potential (-4.83 eV).[109,113,129] Thus, part of the photogenerated electrons can relax to the H^+/H_2 energy level and reduce H^+ to H_2 in the solutions. The similar process can occur for 1L MoS_2 with a CBM near -4.1 eV, as shown in **Figure 5.6** (b), however, the smaller energy difference between CMB and $\phi(H^+/H_2)$ in comparison with 1L WSe_2 results in a smaller electron driving force/rate to reduce H^+ to H_2.[130,131] The VBM of 1L WSe_2 is about -5.2 eV,[113,132] which lies above the O_2/H_2O potential (-5.66 eV). The photogenerated holes from 1L WSe_2 cannot totally recombine with the photogenerated electrons because the parts of the electrons which relaxed to the H^+/H_2 level and reduced

H^+ to H_2 have been consumed which relaxed to the H^+/H_2 level and reduced H^+ to H_2 as shown in **Figure 5.6** (a). Thus, the residual holes degrades the 1L WSe_2 rather than generating O_2 from H_2O which is energetically unfavorable for holes.[128,133] These electrons and residual holes involved the reactions are:[134,135]

$$2H^+ + 2e^- \rightarrow H_2 \qquad 5.2$$

and

$$2WSe_2 + 8h^+ + 8H_2O + 7O_2 \rightleftharpoons 2WO_3 + 4{SeO_4}^{2-} + 16H^+ \qquad 5.3$$

Moreover, WO_3 is thermodynamically unstable[135,136] in aqueous solution, which will induce a second reaction of dissolution, and this will be discussed in the next subchapter. The VBM of 1L MoS_2 is about -6.0 eV which lies below the potential of O_2/H_2O and parts of photogenerated holes might oxygenate H_2O to O_2, as shown in **Figure 5.6** (b). Thus, 1L MoS_2 does not tend to be degraded within a short time, which well explained the photodegradation difference between 1L WSe_2 and MoS_2 in distilled water condition.

5.2.3. Photon energy effect on the PL property in distilled water

1L WSe_2 is easily photodegraded in distilled water because of the band edge alignment between 1L WSe_2 and O_2/H_2O system. The excess photon energy of irradiation light could affect the photodegradation. Hence, the effects on the photodegradation of 1L WSe_2 by various laser wavelength (532, 550, and 594 nm from supercontinuum light source, and 594 nm from CW He-Ne laser) in water is also studied, where the irradiation density was kept in the same power density. **Figure 5.7** shows the degradation rates as a function of irradiation wavelength (photon energy), in which the degradation rate was

simply calculated using the PL intensity difference in a fixed time interval (10~15 min.). The longer light wavelength showed a lower degradation rate, which is attributable to the wavelength dependent photocarrier density because of the differences in the absorption coefficient and the photon flux. The CW laser with the same wavelength showed a higher degradation rate compare with the pulse laser. This can be explained that the photo generated carrier density is high only within a very short time (on the order of the pulse duration of ~20 ps) in pulsed excitation whereas the CW excitation provides a time independent average photocarrier density. Thus, the total time allowed for photo induced chemical reactions induced a difference for the CW and pulse excitation.

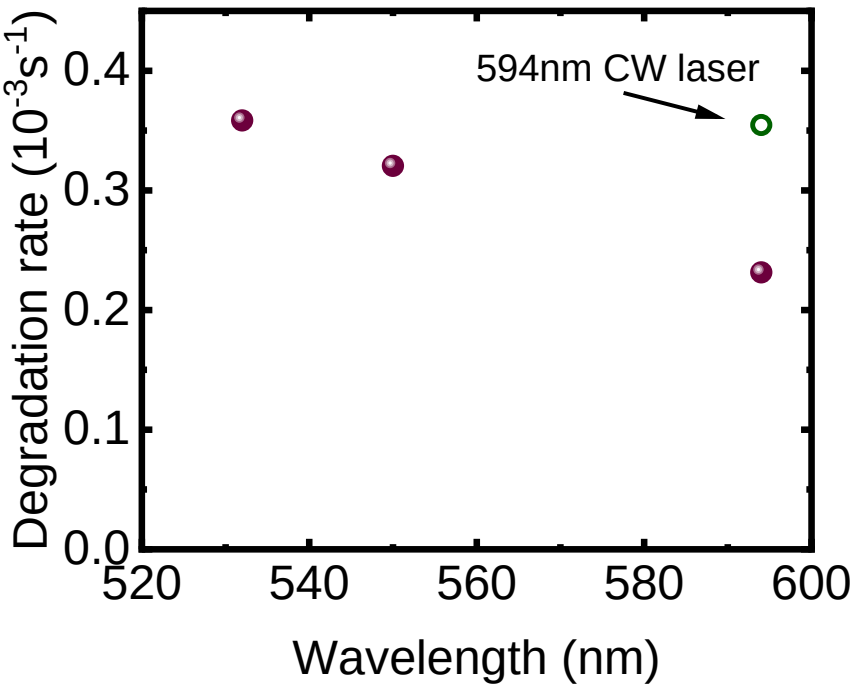

Figure 5.7 Photo induced degradation rate of 1L WSe_2 in distilled water with the pulse laser irradiation of 532, 550, 594 nm and CW laser irradiation of 594 nm.

5.2.4. pH effect on the PL property of monolayer WSe_2 under light irradiation in aqueous solution

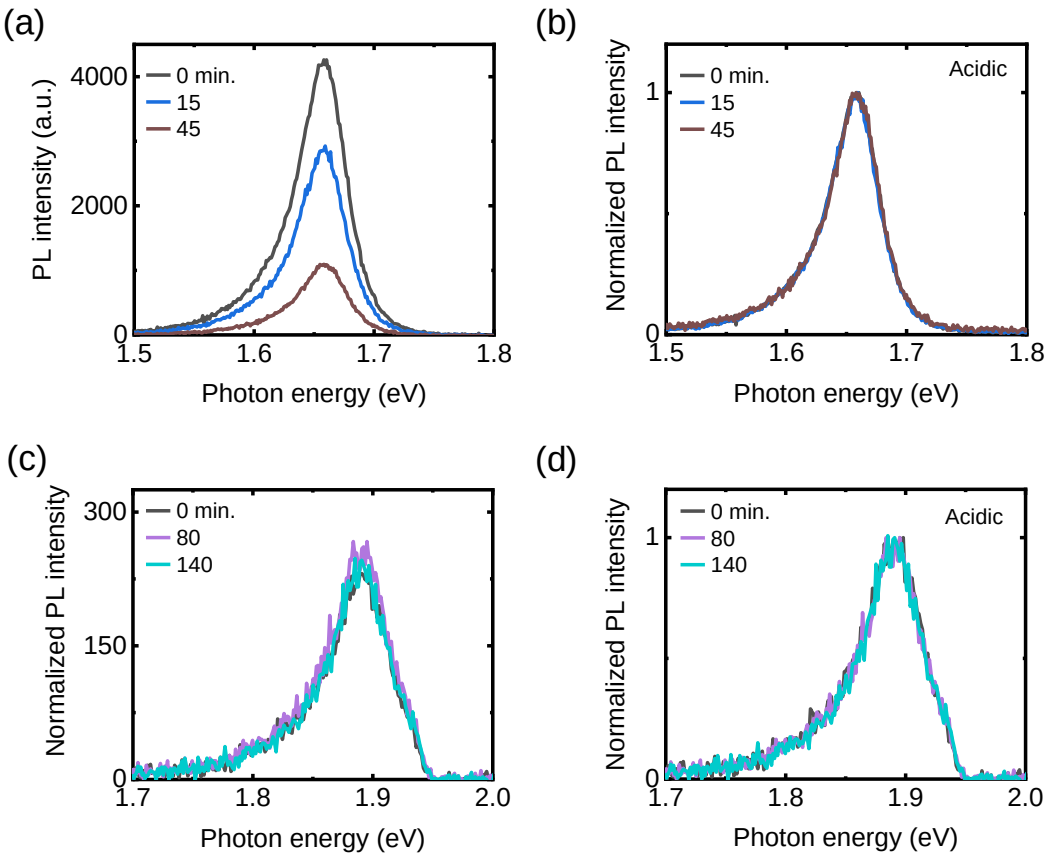

Figure 5.8 PL spectra (a) and (c) and normalized PL spectral shape (b) and (d) of 1L WSe_2 and MoS_2 in basic condition under a 580 nm light irradiation.

As described in Chapter 4, the pH of aqueous solution strongly affects the optical properties of 1L TMDs because of the surface electrochemical reactions resulting in considerable carrier modulation. The pH effect on photostability is also necessary to be studied. **Figure 5.8** shows the change of PL spectra of 1L WSe_2 and MoS_2 measured in basic condition (pH ~12): (a) and (c); and in acidic condition (pH ~2): (b) and (d), respectively. In the acidic condition, the PL intensity of 1L WSe_2 dramatically decreased

within 45 minutes, whereas the 1L MoS_2 did not show any changes within 140 minutes. The normalized PL spectra shape showed that both the 1L WSe_2 and MoS_2 did not show any changes of spectral shape during the photo irradiation time, which suggests that the carrier density in 1L TMDs keeps constant during this process and the changes of PL intensity is not from the carrier injection or extraction into/from 1L TMDs.

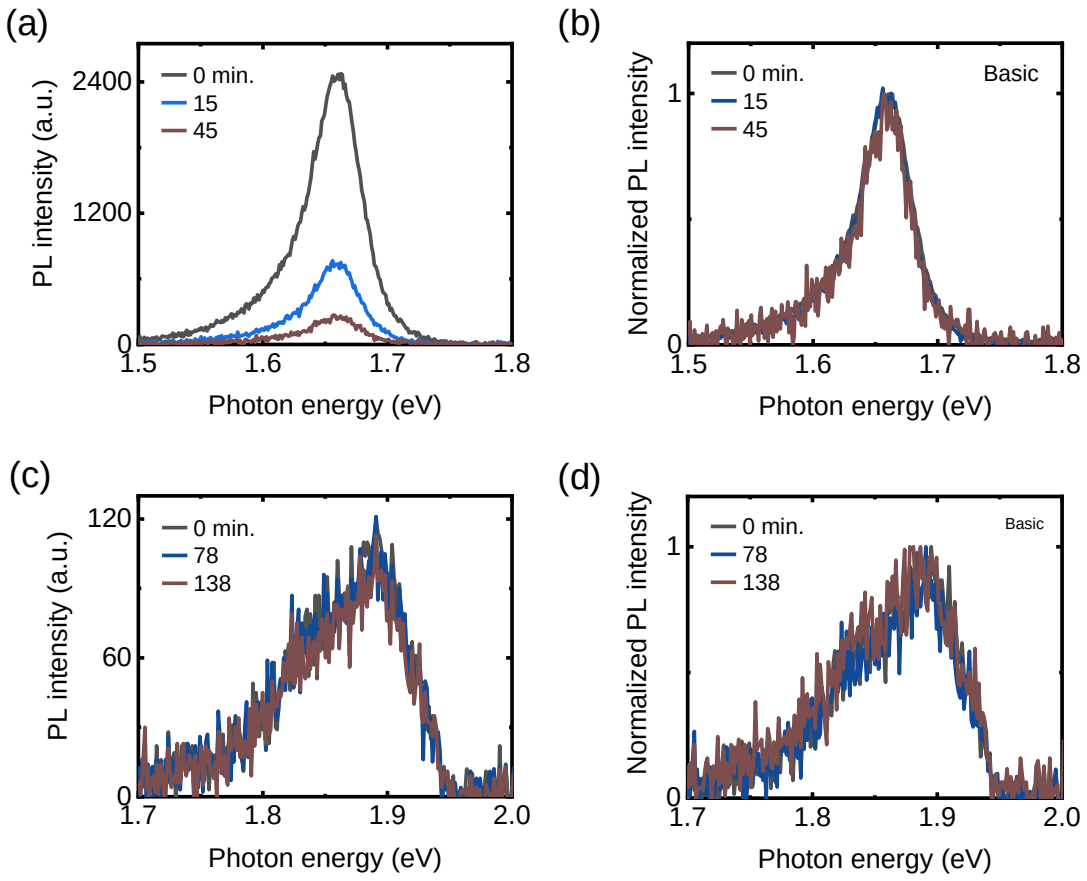

Figure 5.9 PL spectra (a) and (c), and normalized PL spectral shape (b) and (d) of 1L WSe_2 ((a) and (b)) and MoS_2 ((c) and (d)) in basic condition under a 580 nm light irradiation.

Similar results were observed in basic conditions. As shown in **Figure 5.9**, the PL intensity of 1L WSe_2 in basic condition rapidly decreased within 15 minutes with an amount of more than ~75%, which is much faster than that in acidic condition (~30%). The normalized PL spectral shape of both 1L WSe_2 and MoS_2 as shown in **Figure 5.9** (b) and (d) kept unchanged during the photoirradiation, which is similar with the behaviors in acidic and distilled water conditions. These results can be explained that the photogenerated electrons and holes are energetically committed to the water redox reactions and not likely to involve into trion formation from exciton.

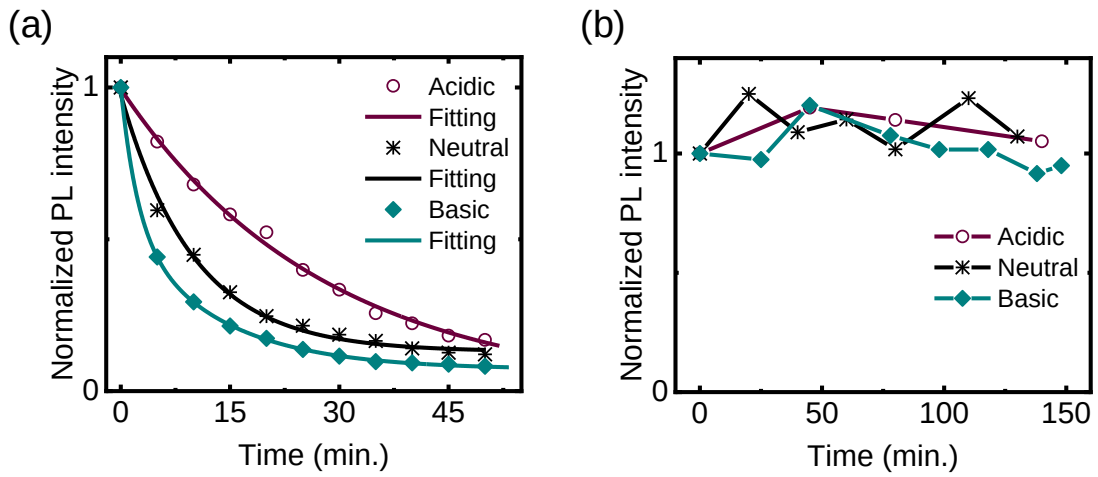

Figure 5.10 Time dependent PL intensity of 1L WSe_2 (a) and MoS_2 (b) in acidic, neutral and basic condition, respectively.

The decreasing speeds of PL intensity of 1L WSe_2 within the same time interval are different in acidic, water and basic condition, which means that the degradation rate is different in these conditions. For better comparison and understanding the mechanism, the normalized PL intensities of 1L WSe_2 and MoS_2 in acidic, water (neutral) and basic conditions were plotted in **Figure 5.10**. The PL intensity of 1L WSe_2 in all conditions

showed a rapidly decrease with increasing the photoirradiation time, whereas the 1L MoS_2 showed a stable PL intensity in all the conditions as shown in **Figure 5.10** (a) and (b), respectively. In addition, the main decrease of PL intensity for 1L WSe_2 in all the conditions occurred within the first 10–15 min and then the decrease slowed down, which is likely because the increased concentration of the degradation products from 1L WSe_2 slowed down the degradation reactions. The PL intensity plot (degradation curve) is considerably different for 1L WSe_2 in all the conditions. 1L WSe_2 showed a relatively moderate degradation rate (PL intensity decrease) in acidic condition, whereas faster degradation was observed in neutral and basic conditions. Within the first 10 minutes, the original PL intensities showed a decrease by approximately 15, 40, and 55% in acidic, neutral, and basic condition respectively. This large difference of degradation rate mainly comes from the easily dissolved WO_3 that is one of the degradation products of WSe_2 in aqueous solutions. It has been well know that the WO_3 showed a thermodynamic instability[135,136] in aqueous solution,

$$WO_3 + H_2O \rightleftharpoons {WO_4}^{2-} + 2H^+ \qquad 5.4$$

whose reaction rate also strongly depends on the pH of aqueous solution. This second degradation reaction in Equation 5.4 can well explain the pH dependence of photodegradation rate. The dissolution reactions of WO_3 become faster because of the higher concentration of OH^- in basic condition than that in acidic condition. Thus, the oxidation reaction and the dissolution reaction of WSe_2 and WO_3 induced a fast degradation in basic condition, in which more defects and edges on 1L WSe_2 flake were generated.[137–140] This is supported by the fitting of time dependent PL intensity plot as shown in **Figure 5.10.** In acidic condition, the PL intensity in the time trace is well fitted

by a single exponential function, whereas a much faster initial degradation was observed in basic condition that cannot be reproduced by a single exponential function, which implied that an additional electrochemical process was involved with a different time scale. Consequently, the degradation species of WSe_2 differ among the acidic (WO_3 and SeO_4^{2-}), neutral, and basic conditions (WO_4^{2-} and SeO_4^{2-}). This experimentally observed pH dependent degradation properties are also consistent with the pH dependent Gibbs free energy of WSe_2 as reported recently.[141]

Moreover, the rate equation was introduced to describe the degradation of 1L WSe_2 in acidic condition,

$$dA/dt = -\alpha A \qquad 5.5$$

where A is the undegraded area of 1L WSe_2 at time t, and α is a rate constant. From equation above, $A = A_0 e^{-\alpha t}$ is obtained, where A_0 is the original area of 1L WSe_2. The undegraded area of 1L WSe_2 exponentially decreases with time, which also support the single exponential PL intensity decrease in acidic condition as shown **Figure 5.10** (a).

5.2.5. Oxygen effect on the PL property of monolayer WSe_2 with light irradiation in distilled water

As introduced in Equation 5.3, 1L WSe_2 was degraded by the photogenerated holes, and the oxygen also played an important role during the degradation reaction. To further confirm this oxygen effect, the PL properties of 1L WSe_2 in the dark (not light illuminated except the PL measurement time) and in degassed water condition were measured. As shown in **Figure 5.11**, the degradations corresponding to the PL intensity decrease in dark (~46%) and degassed water (~38%) are much slower than that in distilled water (~38%)

within 30 minutes. Furthermore, the degradation in degassed water is slightly smaller in comparison with that in dark condition. These results strongly support the conclusion described above that the dissolved oxygen and photogenerated holes are key elements for the degradation of 1L WSe_2 in aqueous solutions.

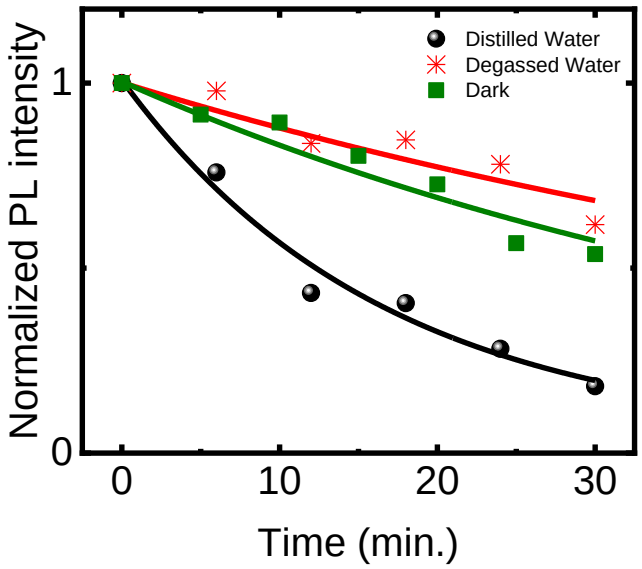

Figure 5.11 Time dependent PL intensity of 1L WSe_2 in distilled water, water in dark, and degassed water. The solid curves are the results of fitting using single exponential functions.

5.2.6. Photoexcited carrier density effect on degradation of monolayer WSe_2 in distilled water

As discussed above, the photoexcited holes is one of the key elements for degradation of 1L WSe_2 in aqueous solutions. The photoexcited holes density strongly depend on the irradiation power density, by which the photogenerated carrier density was directly modulated. **Figure 5.12** shows the power dependent PL intensity of 1L WSe_2 in

water in acidic, neutral and basic conditions, respectively. The degradation (PL intensity decrease) speed in acidic, neutral and basic conditions strongly depends on the irradiation power density. In all conditions, the higher power density results in a faster degradation speed, which supports the above discussion that the photogenerated holes degraded 1L WSe_2 in aqueous solutions.

Furthermore, the time trace of PL intensity in acidic condition are well fitted using a single exponential function, whereas those in neutral and basic conditions are reproduced by biexponential function, which also supports the above discussion that an additional electrochemical process was involved with a different time scale. For better comparison, the degradation rate was used to estimate the degradation speed of 1L WSe_2 that was calculated using PL intensity decrease at a time interval, and the power density was used to calculate the photogenerated carrier density, in which the photon number is proportional to the photo generated election hole pairs.

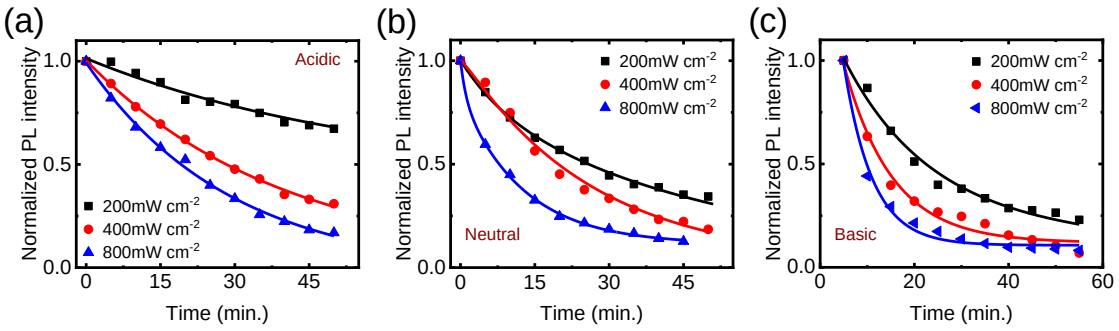

Figure 5.12 Power dependent PL intensity of 1L WSe_2 with time increasing in acidic (a), neutral (b) and basic (c) conditions. The solid lines are the fitting curve using single (a) and biexponential functions (b and c).

Figure 5.13 showed the degradation rate as a function of photogenerated carrier density in the acidic, neutral, and basic conditions. The degradation rates in all conditions are nearly proportional to the density of photogenerated electrons/holes. Moreover, the degradation rate in basic condition is almost one order of magnitude larger than that in acidic condition with a photocarrier density of 6×10^{10} cm^{-2} s^{-1}. The degradation rate in neutral condition is between the acidic and basic condition, which support the above discussion that the second dissolve reaction in Equation 5.4 increased degradation speed of the 1L WSe_2 in neutral and basic conditions.

From the calculated results, the degradation rate (PL intensity decrease rate) of 0.1 ~0.3×10^{-3} s^{-1} was extrapolated when the photocarrier density is zero as shown in **Figure 5.13**, which is consistent with the calculated degradation rate of ~0.3×10^{-3} s^{-1} in the dark condition (**Figure 5.11**).

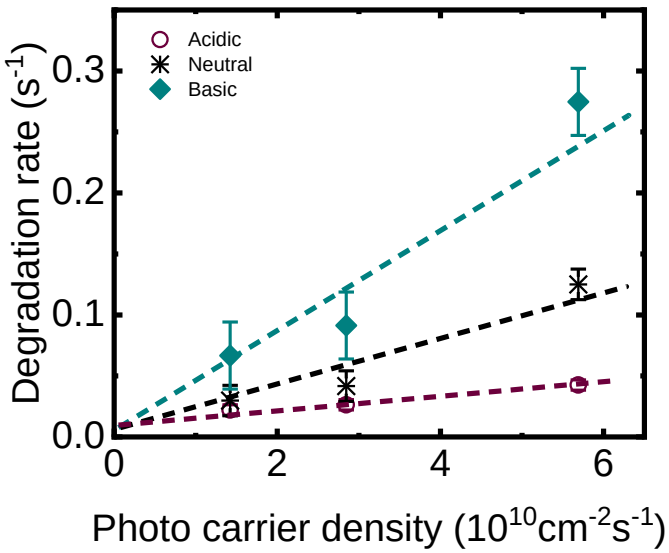

Figure 5.13 Photocarrier density dependent degradation rate in acidic, neutral, and basic conditions, respectively. The dashed lines are the trend fitting lines.

5.3. Chapter summary

In this chapter, the photostabilities of 1L WSe_2 and MoS_2 in ambient air, aqueous solutions with pH were investigated by PL spectroscopy. Under a continuous irradiation using a light with visible wavelength, 1L WSe_2 was readily degraded whereas 1L MoS_2 was relatively stable in both ambient air and aqueous solutions. This considerable difference between two 1L TMDs was mainly ascribed to the difference of oxidization reaction at the interface of 1L TMDs and the O_2/H_2O redox system induced by band alignment. The photogenerated holes and dissolved oxygen played important roles in degradation reactions. These are strongly supported by the further observed results that the degradation rate of 1L WSe_2 is much lower in dark and degassed water in comparison with distilled water and the results of photogenerated carrier density dependent degradation rates in acidic, neutral and basic conditions. Furthermore, the degradation rate showed a strong pH dependent behavior that the degradation in basic condition is faster than that in acidic conditions. This is attributed to the oxidation/reduction potential of the 1L WSe_2 and the dissolution reaction of degraded species, both of which are strongly pH dependent.

The experimental findings and revealed mechanism in this chapter might provide an insight into the electrochemical reactions at the interface of atomically thin semiconductors and an O_2/H_2O redox system on their photostability. This is one of the key factors for the device fabrication and applications in realistic environments with finite humidity or liquid conditions.

Chapter 6. Chemical doping effect on the trion valley polarization property of monolayer MoS_2

In the liquid (aqueous solution) condition at room temperature, the modulations of photophysical properties, which mainly induced by surface electrochemical reactions on 1L TMDs, was observed as discussed in the previous chapters. In this chapter, the impacts of chemical doping treatment at a dry condition on the valley polarization properties of 1L MoS_2 at low temperature will be discussed.

6.1. Introduction

Monolayers of TMDs have emerged as a new class of 2D semiconductors promising for future electronics and optoelectronics applications beyond graphene, not only because of their finite direct bandgaps and readily tunable physical or electrical properties, but also because of their two degenerated valleys K and K' at the corners of the hexagonal Brillouin zone. The strong spin orbit interaction and the broken structural inversion symmetry in these 1L TMDs enable a selective generation of excitons and trions in one of these valleys using circular polarized light, which results in a unique excited state with "valley polarization." This makes these materials quite attractive for exploiting optoelectronics called valleytronics, where the valley degree of freedom is used as information carriers in information processing technology with high speed and low energy consumption.

Excitons and trions are two important quasiparticles that dominate the optical properties of 1L TMDs. Various methods for modulating exciton valley polarization have been proposed, such as using a magnetic field,[43,45,50,142] photon-upconversion

process,[143,144] carrier density tuning,[145–150] and van der Waals engineering.[151–154] However, bright excitons in 1L TMDs, which can potentially show high PL intensity necessary for their realistic applications, have a very short intrinsic valley lifetime on the order of 10 ps, and this is considered as a major limitation for their applications.[155–157] In contrast, trions can potentially show a longer valley lifetime than excitons,[158–160] which can be an alternative for carrying information in valleytronics.[158,159] However, trion emission is normally weak and show spatially heterogeneous valley polarization, which prohibits the realistic application of trions in these materials.

Many methods have been used to enhance the PL emission efficiency such as using *h*BN substrate,[46,161,162] or chemical treatment,[48,49,124] and to increase the valley lifetime using heterostructure method.[151–154,163,164] Among various methods, chemical doping treatment is one of the easy and efficient methods to modify the exciton or trion PL properties.[48,49] At room temperature, *p*-type dopant F_4TCNQ has been proved as an effective molecule to modify the exciton/trion PL emissions.[48] However, the effect of the F_4TCNQ treatment on valley polarization property at cryogenic temperature remains to be revealed. In this chapter, the typical *p*-type dopant F_4TCNQ was used to treat the 1L MoS_2 on SiO_2/Si substrate. The valley polarization property of trions was measured at 15K after the doping treatment using a PL mapping method to obtain the information of the whole sample.

6.2. Adsorption effect of chemical dopant F_4TCNQ on the PL properties of excitons and trions

In this subchapter, the effect of F_4TCNQ adsorption on the PL properties of excitons and trions for as-prepared 1L MoS_2 on SiO_2 substrate at 300 K and 15 K will be discussed.

6.2.1. **Chemical dopant effect on PL properties of monolayer MoS_2 at 300 K**

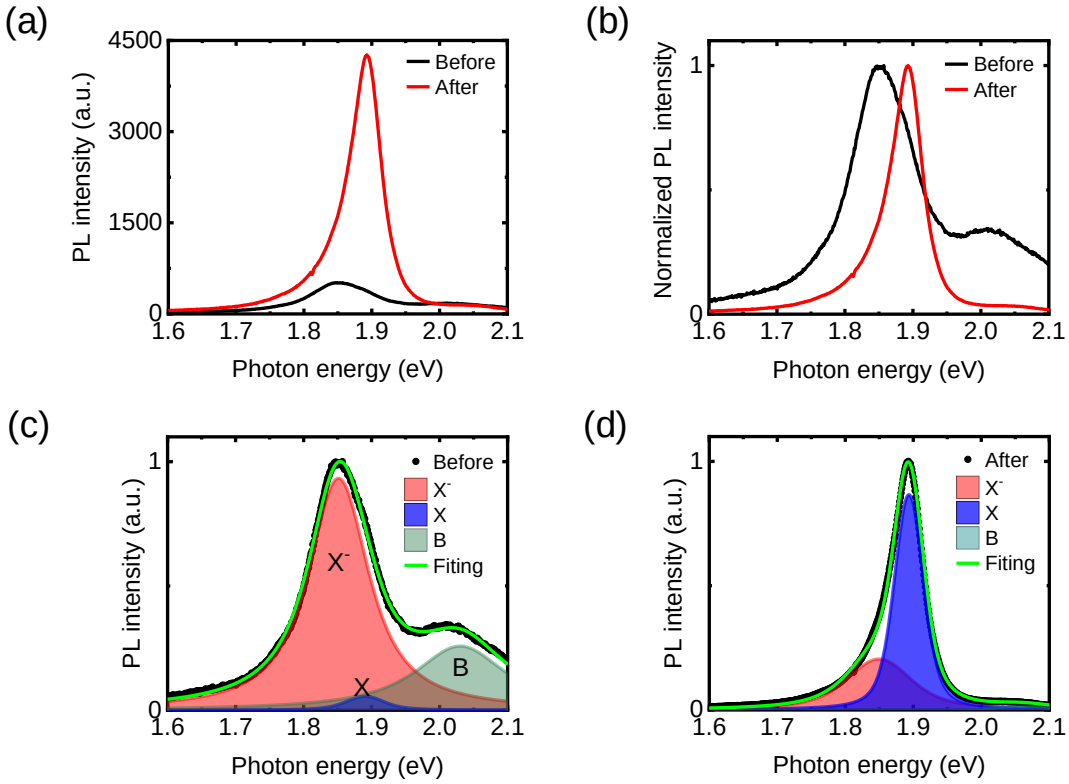

Figure 6.1 PL spectra (a) and normalized PL spectra shape (b) before and after the F_4TCNQ doping treatment with 532 nm laser exciton. Decomposition of the normalized PL spectra with exciton and trion peaks before (c) and after (d) the treatment.

The drop cast method was used for the F_4TCNQ chemical doping treatment of as prepared 1L MoS_2 on SiO_2.[48] The PL properties before and after the treatment were measured under a 532 nm CW laser excitation. As shown in **Figure 6.1** (a) and (b), PL intensity increased almost 10 times after the treatment. Normalized PL spectra showed that after the treatment, there is a considerable change in the spectral shape and peak

position. For better comparison, the normalized PL spectra were decomposed into negatively charge trion (X^-) at ~1.85 eV, neutral exciton (X) at ~1.89 eV (A exciton), and B exciton (B) at ~2.03 eV.[48] As shown in **Figure 6.1** (c) and (d), before the treatment, the PL intensity ratio of A excitons and trions I_X / I_{X^-} was ~0.06, and increased to ~4.2 after the treatment by a factor of ~70 times. This considerable modulation of I_X / I_{X^-} suggests electron extraction from heavily *n* doped MoS_2. This also explained the peak shape change and shift in **Figure 6.1** (b): before the treatment, the main PL component of 1L MoS_2 is attributed to trions, while exciton PL is the main component after the treatment. This result is consistent with the previous report that the carrier density in as-prepared 1L MoS_2 strongly reduced after the *p*-type dopant F_4TCNQ treatment.[48] The peak labeled as B is from the B exciton hot luminescence and will be not discussed at the present stage.

6.2.2. Trion PL properties of monolayer MoS_2 at 15 K

To further examine the chemical doping effect on the valley polarization properties of 1L MoS_2, the PL spectra were measured at 15 K. As shown in **Figure 6.2**, the exciton peak was cut by the edge filter because the A excitons were resonantly excited using 633 nm (1.96 eV) light. The trion PL intensity showed a considerable increase at 15 K after the F_4TCNQ treatment as compared in **Figure 6.2** (a) and (b).

To further understand this increase of trion PL intensity after the treatment, time resolved PL spectroscopy was carried out. As shown in **Figure 6.3**, the time resolved PL profiles before the treatment is almost undistinguishable with the instrumental response function (IRF), whereas the decay profile after the treatment is considerably extended. The effective lifetime of trion, $\langle \tau_{tr} \rangle$ was deduced from the time resolved PL decay curve using convolutions of a biexponential function $I(t) = C_1 \exp(-t/\tau_1) + C_2 \exp(-t/\tau_2)$

and the IRF, then was calculated using $\langle \tau_{tr} \rangle = (C_1\tau_1 + C_2\tau_2)/(C_1 + C_2)$. This quantity is proportional to the trion photoluminescence quantum yield η_{tr} as $\eta_{\mathrm{tr}} = \tau_{\mathrm{r-tr}}^{-1}\langle \tau_{\mathrm{tr}} \rangle$, where $\tau_{\mathrm{r-tr}}$ is the radiative lifetime of trions. Before the treatment, $\langle \tau_{\mathrm{tr}} \rangle$ could not be rigorously determined because of the limitation of the detection system (~ 20 ps), whereas ~70 ps was obtained after the treatment. With consideration of the low PL quantum yield of trions in 1L MoS_2, this result suggests that the observed enhancement of the trion PL intensity after the F_4TCNQ chemical treatment is owing to the considerably extended trion effective lifetime, mainly due to the increased nonradiative lifetime of trions. The increase of the nonradiative lifetime may be from the passivation of sulfur vacancy defect[49,98,117,165] by the F_4TCNQ molecular absorption.

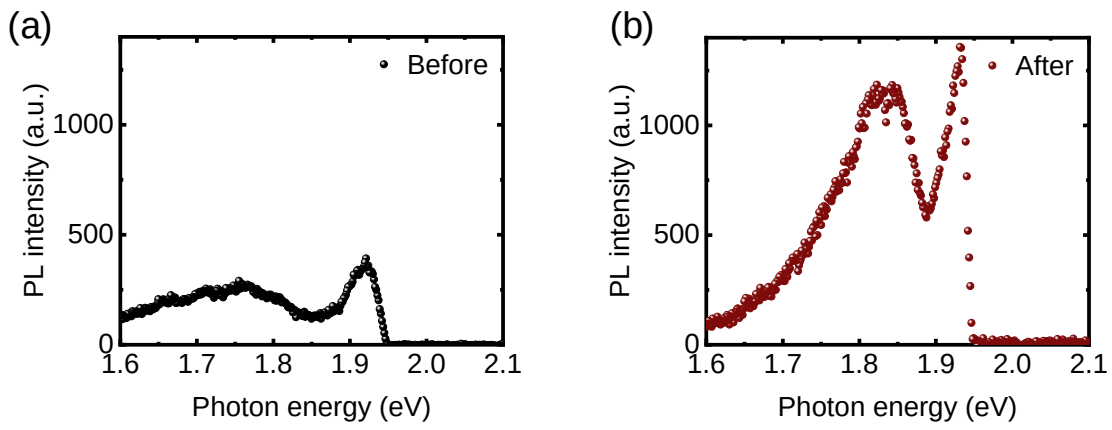

Figure 6.2 PL spectra of 1L MoS_2 before and after the treatment at 15 K under the near A-exciton resonant excitation at 633 nm (1.96 eV). The PL feature around 1.9 eV corresponds to the trion PL, and the broad lower energy feature has been attributed to localized exciton state.[166] The abrupt cut off at ~ 1.95 eV is because of the edge pass filter which was used to cut the direct scattering/reflection of the excitation light.

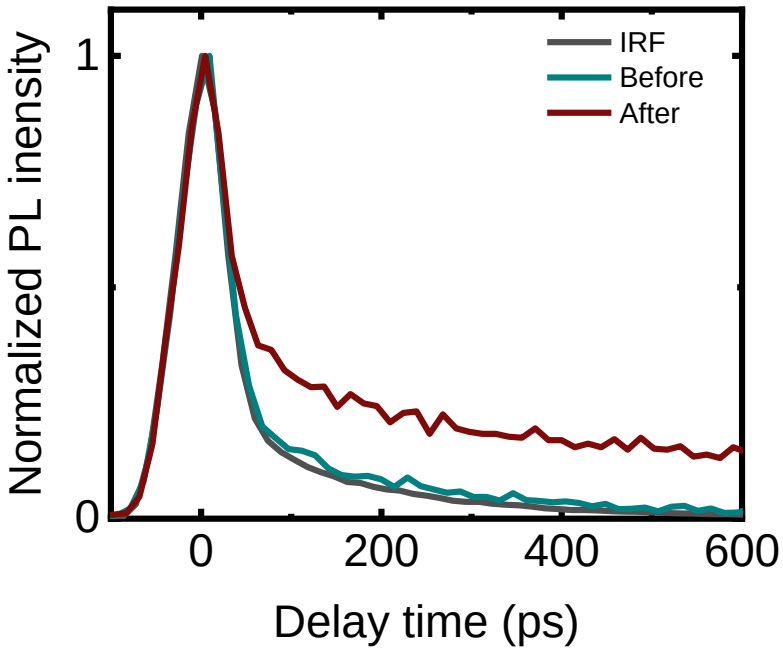

Figure 6.3 Time resolved PL decay profiles of 1L MoS_2 at 15 K before and after the F_4TCNQ treatment with a 580nm pulse laser exciton.

6.2.3. **Trion PL map of monolayer MoS_2 at low temperature**

To further examine the PL and valley polarization properties throughout the sample, spatial PL mapping method was used to obtain valley polarization resolved PL spectra at all the points on sample. The PL images reconstructed from the data before and after F_4TCNQ treatment at room temperature are shown in **Figure 6.4**. The average PL intensity considerably increased after the treatment, however, the heterogeneity of PL intensity was still observed after the treatment. This result suggests that the F_4TCNQ chemical treatment is effective for enhancing the PL intensity, but ineffective for improving the PL heterogeneity of 1L MoS_2 on SiO_2/Si substrate.

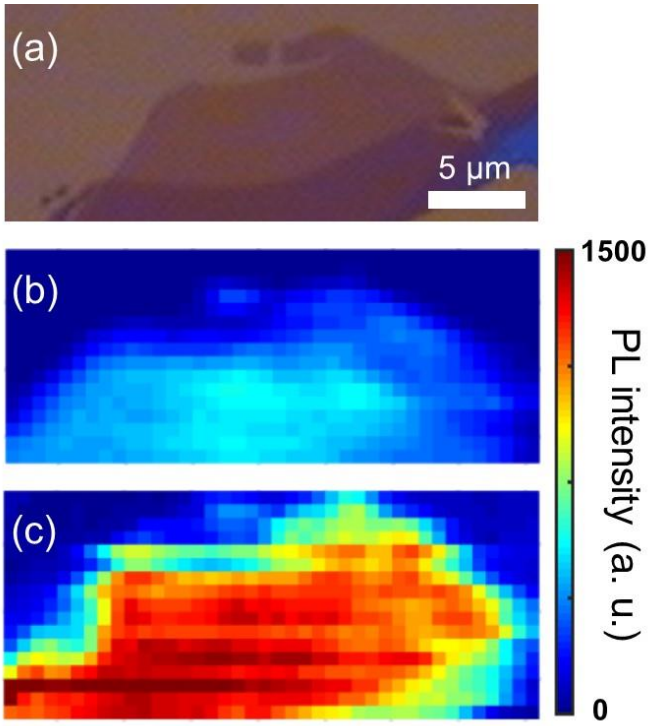

Figure 6.4 Optical image (a) and PL mapping images of 1L MoS_2 before (b) and after (c) the F_4TCNQ chemical treatment.

6.2.4. Position dependent trion lifetimes after the doping treatment

To further understand the PL property of the whole sample, we measured time resolved PL profiles at typical points showing different PL intensities. As shown in **Figure 6.5** (a), the time resolved PL profiles are considerably different among the measured points with various PL intensities. The effective lifetime was obtained through a fitting procedure as introduced above. Strong positive correlation was obtained between the effective lifetime of trions $\langle \tau_{tr} \rangle$ and the corresponding PL intensity I of 1L MoS_2 as shown in **Figure 6.5** (b). This result also suggests that nonradiative relaxation pathways mainly dominate the trion PL lifetime. The spatial variation in the local defect density,

local carrier density, and/or local condition of passivation are presumably be the potential causes of spatial heterogeneity in the trion PL intensity on the sample.

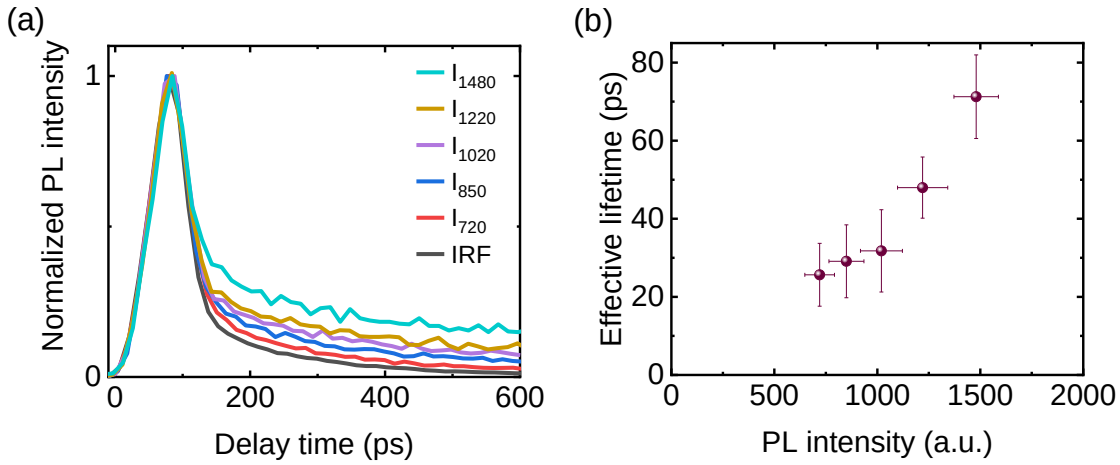

Figure 6.5 Time-resolved PL profile at points with various PL intensities I_α, where α is the corresponding PL intensity at the same position (a). Effective PL lifetime of trions at various points plotted as a function of the corresponding PL intensity (b).

6.3. Effects of chemical dopant F_4TCNQ adsorption on valley polarization properties of monolayer MoS_2

6.3.1. Trion valley polarization of monolayer MoS_2

To statistically compare the valley polarization property throughout the sample, the trion valley polarization maps were obtained using the circular polarization resolved PL spectra measured at each point under σ^+ excitation light as:

$$\rho = \frac{I^+ - I^-}{I^+ + I^-} \qquad 6.1$$

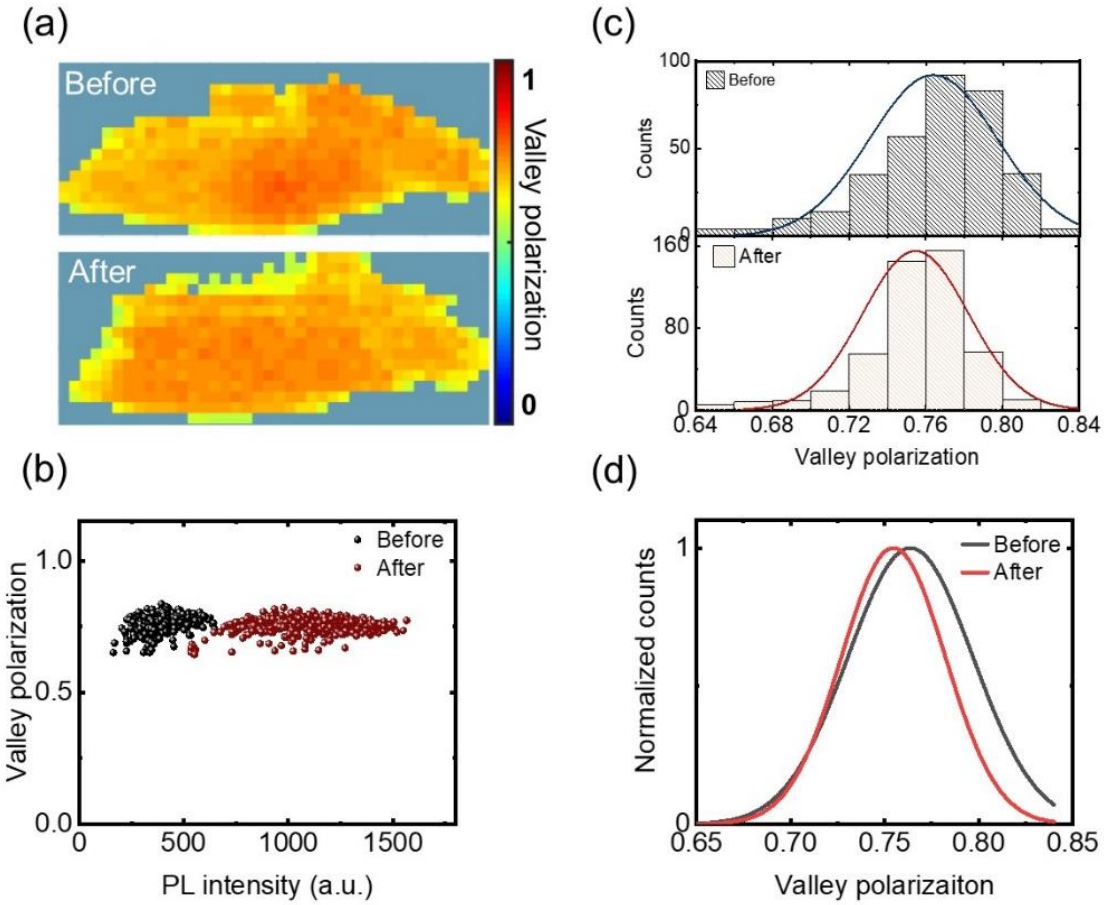

Figure 6.6 Valley polarization map of 1L MoS_2 measured before and after the F_4TCNQ treatment at 15K (a). Valley polarization at various spots plotted as a function of the corresponding PL intensity at the same spots before and after treatment (b). Valley polarization histogram with distribution curve before and after the treatment (c). Comparison of the distribution curves of the valley polarization in (c) (d).

where I^+ and I^- are σ^+ and σ^- polarized trion emission intensity, respectively. The PL data from the sample edges were excluded for generating the valley polarization maps to avoid possible edge effects, such as residual strain, folding, insufficient substrate contacts, and insufficient excitation.[167–171] As shown in **Figure 6.6** (a) and (b), the degree

of trion valley polarization did not show considerable change after the treatment, while the uniformity became slightly improved. To statistically compare, the histograms and distribution curves were plotted in **Figure 6.6** (c) and (d). The valley polarization became closer to a well normal distribution with a narrower spread after the treatment than that before the treatment as shown in **Figure 6.6** (c). The trion valley polarization before the treatment exhibited an average value of 0.76 with a standard deviation (STD) of 0.03, and the value of 0.75 with an STD of 0.02 after the treatment. The normalized distribution curve after the treatment showed a small decrease of the mode value (of the order of 0.01) which is a negligible decrease compared to the high trion valley polarization of ~0.75. These results suggested that the F_4TCNQ chemical treatment only yields a considerable enhancement of the PL intensity with a negligible decrease of the trion valley polarization of 1L MoS_2 at 15 K.

6.3.2. **Trion valley lifetime in monolayer MoS_2**

To further understand the mechanism of the PL intensity enhancement without large modulation in the valley polarization, the valley polarizations of trions at typical positions on the sample were plotted against the PL lifetimes measured at the same positions in **Figure 6.7**. High uniformity of the trion valley polarization was observed regardless of the various trion effective lifetimes $\langle\tau_{tr}\rangle$ at each point.

Under the direct excitation of A excitons and successive trion generation from excitons and excessive electrons, the valley polarization of trions ρ_{tr} can be phenomenologically expressed as:

$$\rho_{tr} = \frac{1}{1+\langle\tau_{tr}\rangle/\tau_{v-tr}}\rho_{ex} \qquad 6.2$$

where $\langle\tau_{tr}\rangle$, τ_{v-tr} and ρ_{ex} are effective trion lifetime, trion valley lifetime and exciton valley polarization, respectively.[35,172] Equation 6.2 suggests that the $\langle\tau_{tr}\rangle$ and ρ_{tr} are correlated in principle. However, the effective lifetime $\langle\tau_{tr}\rangle$ is independent of ρ_{tr} as shown in **Figure 6.7** and this implies that almost no strong correlation between these parameters, which is considerably different from the case of neutral bright excitons.[35,149,157] With regard to neutral bright excitons in 1L TMDs, the extension of exciton PL lifetime normally results in a strong reduction in their valley polarization because the valley relaxation is dominated by electron-hole exchange interaction occurs within a time scale of picoseconds, which is much shorter than or is at most comparable to the exciton lifetime in 1L TMDs.[35,149,157] According to the Equation 6.2, the correlation between ρ_{tr} and $\langle\tau_{tr}\rangle$ was simulated by setting τ_{v-tr} as a constant value as shown in **Figure 6.7**. From the comparison of the experimental and simulated results, valley lifetime τ_{v-tr} at least with an order of at least nanosecond was deduced. The condition $\langle\tau_{tr}\rangle/\tau_{v-tr} \ll 1$ implies that the trion valley lifetime τ_{v-tr} is much longer than typical values of $\langle\tau_{tr}\rangle$. This is consistent with previously reported values.[173–175] The long trion valley lifetime, τ_{v-tr}, is a manifestation of the lack of an efficient intrinsic valley relaxation pathway for trions at low temperatures,[160] which results in a high valley polarization of trions that is insensitive to the local fluctuations in $\langle\tau_{tr}\rangle$. Thus, the valley polarization of trions ρ_{tr} could be kept high, despite $\langle\tau_{tr}\rangle$ increased several times after the F_4TCNQ treatment.

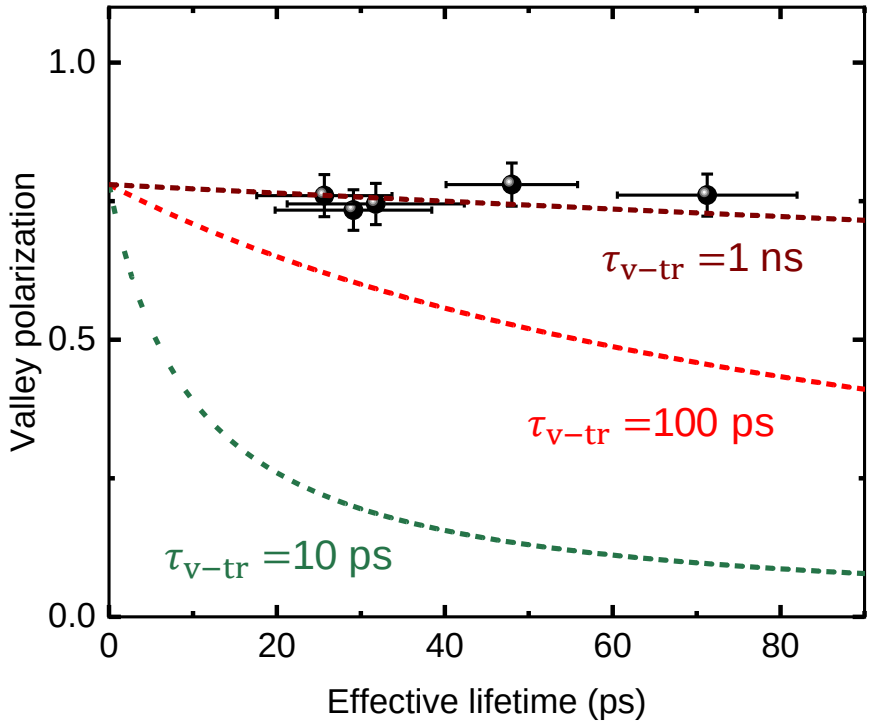

Figure 6.7 Trion valley polarization of F_4TCNQ-doped 1L MoS_2 at various positions plotted against the corresponding effective lifetime measured at the same positions. The dashed lines are simulated curves based on Equation 6.2 with various τ_{v-tr}. Exciton valley polarization ρ_{ex} is estimated as ~0.8.

6.4. Chapter summary

In this chapter, the effects of F_4TCNQ chemical dopant treatment on the valley polarization properties of trions in as-exfoliated 1L MoS_2 was studied. The valley polarization properties of trions at a cryogenic temperature was measured using the polarization resolved PL mapping method before and after the treatment. The PL intensity of 1L MoS_2 showed a considerably increase after the *p*-type dopant F_4TCNQ adsorption at 300 K, which results from the carrier extraction from heavily *n*-doped 1L MoS_2. This

was confirmed by observing the change in the exciton and trion PL intensity ratio modification at room temperature.[48,176] At 15 K, the trion PL intensity considerably increased after the treatment, and this is attributed to the extension of trion lifetime from < ~20 ps to ~70 ps based on the results of time-resolved PL decay measurements. In contrast to the considerable increase of trion PL intensity, the trion valley polarization evaluated from more than 700 mapping points showed a high and quite uniform (~0.75) values regardless of the dopant treatment, local PL intensities, and local PL lifetimes. This insensitivity of the trion valley polarization to the trion lifetime suggests a very long valley lifetime at least of the order of at least nanoseconds, which is considerably different with excitons dominated by electron hole exchange interaction. This finding of the brightened and highly valley polarized trions in 1L MoS_2 after the F_4TCNQ chemical doping treatment offers an opportunity to improve the trion PL brightness in 1L MoS_2 with retaining their valley polarization as high as ~0.75. Thus, the trions in the chemically doped 1L MoS_2 are one of the unique candidate as the information carriers for realizing future optovalleytronics based on 1LTMDs.

Chapter 7. Summary and Future outlook

7.1. Summary

In this thesis, the effects of various surface interactions on the optical, photostability, and valley polarization properties in 1L TMDs were studied in liquid and dry conditions using various optical spectroscopy methods. In the liquid (aqueous solution) conditions, the PL properties of 1L MoS_2 were strongly modulated depending on pH of the solutions. The mechanisms of these modulations were revealed and confirmed using an electrochemical model. The effects of pH, oxygen, water and their redox potential on the PL properties were understood. Based on the understanding of these surface interaction effects on the PL properties, the photostability of 1L MoS_2 and WSe_2 was further studied. The effect of the bandgap alignment, oxygen, solution pH, and photogenerated carriers on the stability of 1L TMDs was clarified. The difference of the photostability of 1L MoS_2 and WSe_2 was experimentally found and the mechanism of this difference was explained based on the relative alignment of the valence and conduction band levels and the pH-dependent water redox potential. These experimental results and the revealed mechanisms in ambient air and aqueous solutions gave us a fundamental understanding on the surface electrochemical interactions effects on optical properties of 1L TMDs in various humid or full of water molecules conditions. This understanding also gave us an insight on future optical, electronic, and optoelectronic device fabrications and applications which relies on the optical or electronic properties of 1L TMDs that are easily affected by various interface effects in ambient air with humidity or in aqueous solution conditions.

Inspired by the finding and understandings of the strong surface interaction effects on 1L TMDs clarified in chapters 4 and 5, the chemical surface treatment effects on the trion valley polarization properties of 1L MoS_2 in dry condition were also studied. The *p*-type dopant F_4TCNQ was used to treat 1L MoS_2 to extract heavily doped excess electrons from 1L MoS_2. The strong modulation in PL intensity ratio of excitons and trions was observed at 300 K. Then, the valley polarization property of trions at a cryogenic temperature was studied. The considerable enhancement of the PL intensity of trions after the chemical doping treatment was observed at 15 K. The origin of the trion PL enhancement is attributed to the extension of the nonradiative lifetime of trions after the treatment. In contrast to the considerable change in the PL intensity and lifetime before and after the treatment, the trion valley polarization with a high value (~0.75) and high spatial uniformity was found regardless of the treatment. From the relation between the trion lifetime and the trion valley polarization, the long trion valley lifetime with an order of at least nanosecond was deduced. The brightening of the trion PL with retaining the high valley polarization suggested that the chemical treatment using *p*-type dopant F_4TCNQ is one of the effective methods to achieve both high PL intensity and valley polarization of trion at the same time. The observed results and the revealed mechanisms of trion at 15 K suggested that trions are one of the unique alternatives as the valley information carrier which has high potential in optovalleytronics for fast information processing or information storage technology with low energy consumption.

The effects of oxygen, water, photogenerated carriers and chemical dopant molecules on the PL property, photostability and valley polarization property of on 1L TMDs in liquid and dry conditions were systematically studied. The observed results and

revealed mechanisms gave us a deep understanding of the surface interaction effects on excitonic physical properties of 1L TMDs, which is very useful and an important information for future device fabrication and applications using 1L TMDs.

7.2. Future outlook

In this thesis, the surface interaction effects on PL, photostability and valley polarization properties of two typical 1L TMDs were studied. In chapters 4 and 5, the experimental results suggest that 1L MoS_2 is one of the promising materials for device application using its PL properties in aqueous solutions because of its electrochemically tunable PL through carrier density modulation and high photostability. Highly sensitive electronic or optoelectronic devices based on the pH dependent modulation of PL properties or carrier density of 1L MoS_2 in water or aqueous solutions may open a new sensor application field of 1L TMDs. The high stability of 1L MoS_2 in aqueous solutions suggested that it is also a better candidate for water splitting or photo catalyst in aqueous solutions.

The experimental results in chapter 5 showed that the photostability of 1L WSe_2 is much lower in aqueous solutions than that in dry air conditions. This suggests that 1L WSe_2 should be kept in dry condition to avoid the photodegradation, which is important for optoelectronic device applications of 1L WSe_2 in in realistic environments taking advantage of its relatively high quantum yield compared to 1L MoS_2.[49,177] Covering 1L WSe_2 using layers of thin *h*BN and/or AlO_x against the oxidation[178–181] will be a possible solution to avoid the photodegradation of 1L WSe_2 in ambient air with humidity or in aqueous solution, this may show high potential in electrical and optoelectronics device applications based on PL properties of 1L WSe_2.

In chapter 6, the enhanced PL emission and high valley polarization of trion after the F_4TCNQ chemical dopant treatment suggested that this is an effective way to improve the brightness of trion PL and without losing its high valley polarization. This chemical method is easily extendable for the trion PL enhancement in 1L MoS_2 with large area. The deduced long valley lifetime of trion suggested that the trion in 1L MoS_2 is one of the unique candidates as a valley information carrier which is important for future fast information processing or information storage in optovalleytronics. The manipulation of the trion valley polarization based on these findings is one of next important projects to be continued which is also important for real applications. However, after the chemical dopant treatment, the spatial inhomogeneity in the PL intensity was still observed. Recently, the atomic layered materials such as *h*BN and multilayer graphene were used to improve the PL or valley polarization properties of 1L TMDs.[149,181] Therefore, the devices based on trion valley polarization properties of 1L TMDs on these atomically thin substrates may have an improvement in PL or valley polarization properties.

The systematical studies in this thesis not only gave a deep understanding of various surface interaction effects on exciton photophysical properties of 1L TMDs in the liquid and dry conditions, but also gave us an insight for robust device fabrication and applications of 2D semiconductor TMDs. This may offer an opportunity for resolving the problems of growing consumption of energy resources indirectly or directly in near future.

Bibliography

1 S. Sharma, C. Ambrosch-Draxl, M. Khan, P. Blaha and S. Auluck, *Phys. Rev. B*, 1999, **60**, 8610–8615.

2 Sumlo Iijima, *Nature*, 1991, **354**, 56–58.

3 A. C. Neto, F. Guinea and N. M. Peres, *Phys. World*, 2006, **19**, 33–37.

4 R. PEIERLS, *Ann. I. H. Poincare*, 1935, **5**, 177–222.

5 L. D. Landau, *Phys. Z. Sowjet.*, 1937, **11**, 26–35.

6 D. TER HAAR, Ed., *Collected papers of L. D. LANDAU*, GORDON AND BREACH, SCIENCE PUBLISHERS, New York, 1st edn., 1965.

7 A. K. Geim and K. S. Novoselov, *Nat. Mater.*, 2007, **6**, 183–191.

8 K. S. Novoselov, *Science*, 2004, **306**, 666–669.

9 K. S. Novoselov, A. K. Geim, S. V. Morozov, D. Jiang, M. I. Katsnelson, I. V. Grigorieva, S. V. Dubonos and A. A. Firsov, *Nature*, 2005, **438**, 197–200.

10 K. S. Novoselov, D. Jiang, F. Schedin, T. J. Booth, V. V Khotkevich, S. V. Morozov and A. K. Geim, *Proc. Natl. Acad. Sci.*, 2005, **102**, 10451–10453.

11 A. K. Geim and A. H. Macdonald, *Phys. Today*, 2007, **60**, 35–41.

12 B. Partoens and F. M. Peeters, *Phys. Rev. B*, 2006, **74**, 075404.

13 S. Latil and L. Henrard, *Phys. Rev. Lett.*, 2006, **97**, 036803.

14 Z. Chen, Y. M. Lin, M. J. Rooks and P. Avouris, *Phys. E Low-Dimensional Syst. Nanostructures*, 2007, **40**, 228–232.

15 K. I. Bolotin, K. J. Sikes, Z. Jiang, M. Klima, G. Fudenberg, J. Hone, P. Kim and H. L. Stormer, *Solid State Commun.*, 2008, **146**, 351–355.

16 B. Standley, W. Bao, H. Zhang, J. Bruck, C. N. Lau and M. Bockrath, *Nano Lett.*, 2008, **8**, 3345–3349.

17 F. Xia, D. B. Farmer, Y. M. Lin and P. Avouris, *Nano Lett.*, 2010, **10**, 715–718.

18 D. Xiao, W. Yao and Q. Niu, *Phys. Rev. Lett.*, 2007, **99**, 236809.

19 W. Yao, D. Xiao and Q. Niu, *Phys. Rev. B*, 2008, **77**, 235406.

20 V. P. Gusynin and S. G. Sharapov, *Phys. Rev. Lett.*, 2005, **95**, 146801.

21 J. S. Bunch, A. M. van der Zande, S. S. Verbridge, I. W. Frank, D. M. Tanenbaum, J. M. Parpia, H. G. Craighead and P. L. McEuen, *Science*, 2001, **315**, 490–493.

22 S. Gilje, S. Han, M. Wang, K. L. Wang and R. B. Kaner, *Nano Lett.*, 2007, **7**, 3394–3398.

23 X. Wang, L. Zhi and K. Müllen, *Nano Lett.*, 2008, **8**, 323–327.

24 J. Kim, H. Zhou, E. Hosono, E. Yoo, I. Honma and T. Kudo, *Nano Lett.*, 2008, **8**, 2277–2282.

25 A. V. Murugan, T. Muraliganth and A. Manthiram, *Chem. Mater.*, 2009, **21**, 5004–5006.

26 A. K. Geim and K. S. Novoselov, *Nat. Mater.*, 2007, **6**, 183–191.

27 D. Golberg, Y. Bando, Y. Huang, T. Terao, M. Mitome, C. Tang and C. Zhi, *ACS Nano*, 2010, **4**, 2979–2993.

28 K. Mak, C. Lee, J. Hone, J. Shan and T. Heinz, *Phys. Rev. Lett.*, 2010, **105**, 136805.

29 A. Splendiani, L. Sun, Y. Zhang, T. Li, J. Kim, C. Y. Chim, G. Galli and F. Wang, *Nano Lett.*, 2010, **10**, 1271–1275.

30 L. Li, Y. Yu, G. J. Ye, Q. Ge, X. Ou, H. Wu, D. Feng, X. H. Chen and Y. Zhang, *Nat. Nanotechnol.*, 2014, **9**, 372–377.

31 B. W. H. Baugher, H. O. H. Churchill, Y. Yang and P. Jarillo-Herrero, *Nat. Nanotechnol.*, 2014, **9**, 262–267.

32 R. Lv, H. Terrones, A. L. Elías, N. Perea-López, H. R. Gutiérrez, E. Cruz-Silva, L. P. Rajukumar, M. S. Dresselhaus and M. Terrones, *Nano Today*, 2015, **10**, 559–592.

33 I. Pletikosić, F. Von Rohr, P. Pervan, P. K. Das, I. Vobornik, R. J. Cava and T. Valla, *Phys. Rev. Lett.*, 2018, **120**, 156403.

34 F. Xia, H. Wang, J. C. M. Hwang, A. H. C. Neto and L. Yang, *Nat. Rev. Phys.*, 2019, **1**, 306–317.

35 K. F. Mak, K. He, J. Shan and T. F. Heinz, *Nat. Nanotechnol.*, 2012, **7**, 494–498.

36 H. Zeng, J. Dai, W. Yao, D. Xiao and X. Cui, *Nat. Nanotechnol.*, 2012, **7**, 490–493.

37 H. Yu, X. Cui, X. Xu and W. Yao, *Nat. Sci. Rev.*, 2015, **2**, 57–70.

38 K. F. Mak and J. Shan, *Nat. Photonics*, 2016, **10**, 216–226.

39 J. R. Schaibley, H. Yu, G. Clark, P. Rivera, J. S. Ross, K. L. Seyler, W. Yao and X. Xu, *Nat. Rev. Mater.*, 2016, **1**, 16055.

40 K. F. Mak, D. Xiao and J. Shan, *Nat. Photonics*, 2018, **12**, 451–460.

41 M. Buscema, G. A. Steele, H. S. J. van der Zant and A. Castellanos-Gomez, *Nano Res.*, 2014, **7**, 561–571.

42 O. Iff, Y.-M. He, N. Lundt, S. Stoll, V. Baumann, S. Höfling and C. Schneider, *Optica*, 2017, **4**, 669–673.

43 G. Aivazian, Z. Gong, A. M. Jones, R. L. Chu, J. Yan, D. G. Mandrus, C. Zhang, D. Cobden, W. Yao and X. Xu, *Nat. Phys.*, 2015, **11**, 148–152.

44 T. Smoleński, M. Goryca, M. Koperski, C. Faugeras, T. Kazimierczuk, A. Bogucki, K. Nogajewski, P. Kossacki and M. Potemski, *Phys. Rev. X*, 2016, **6**, 21024.

45 P. Back, M. Sidler, O. Cotlet, A. Srivastava, N. Takemura, M. Kroner and A. Imamoğlu, *Phys. Rev. Lett.*, 2017, **118**, 237404.

46 K. F. Mak, K. He, C. Lee, G. H. Lee, J. Hone, T. F. Heinz and J. Shan, *Nat. Mater.*, 2013, **12**, 207–211.

47 J. S. Ross, P. Klement, A. M. Jones, N. J. Ghimire, J. Yan, D. G. Mandrus, T. Taniguchi, K. Watanabe, K. Kitamura, W. Yao, D. H. Cobden and X. Xu, *Nat. Nanotechnol.*, 2013, **9**, 268–272.

48 S. Mouri, Y. Miyauchi and K. Matsuda, *Nano Lett.*, 2013, **13**, 5944–5948.

49 M. Amani, D.-H. Lien, D. Kiriya, J. Xiao, A. Azcatl, J. Noh, S. R. Madhvapathy, R. Addou, S. Kc, M. Dubey, K. Cho, R. M. Wallace, S.-C. Lee, J.-H. He, J. W. Ager, X. Zhang, E. Yablonovitch and A. Javey, *Science*, 2015, **350**, 1065–1068.

50 A. Srivastava, M. Sidler, A. V Allain, D. S. Lembke, A. Kis and A. Imamoglu, *Nat. Phys.*, 2015, **11**, 141–147.

51 R. Nouchi and K. Tanigaki, *Appl. Phys. Lett.*, 2010, **96**, 253503.

52 Z. Yin, H. Li, H. Li, L. Jiang, Y. Shi, Y. Sun, G. Lu, Q. Zhang, X. Chen and H. Zhang, *ACS Nano*, 2012, **6**, 74–80.

53 W. Liu, J. Kang, D. Sarkar, Y. Khatami, D. Jena and K. Banerjee, *Nano Lett.*, 2013, **13**, 1983–1990.

54 C. C. Wu, D. Jariwala, V. K. Sangwan, T. J. Marks, M. C. Hersam and L. J. Lauhon, *J. Phys. Chem. Lett.*, 2013, **4**, 2508–2513.

55 Y. Gao, Z. Liu, D.-M. Sun, L. Huang, L.-P. Ma, L.-C. Yin, T. Ma, Z. Zhang, X.-L. Ma, L.-M. Peng, H.-M. Cheng and W. Ren, *Nat. Commun.*, 2015, **6**, 8569.

56 S. Kretschmer, H.-P. Komsa, P. Boggild and A. V. Krasheninnikov, *J. Phys. Chem. Lett.*, 2017, **8**, 3061–3067.

57 O. Lopez-Sanchez, D. Lembke, M. Kayci, A. Radenovic and A. Kis, *Nat. Nanotechnol.*, 2013, **8**, 497–501.

58 D. Tan, H. E. Lim, F. Wang, N. B. Mohamed, S. Mouri, W. Zhang, Y. Miyauchi, M. Ohfuchi and K. Matsuda, *Nano Res.*, 2017, **10**, 546–555.

59 W. Yu, S. Li, Y. Zhang, W. Ma, T. Sun, J. Yuan, K. Fu and Q. Bao, *Small*, 2017, **13**, 1700268.

60 R. S. Sundaram, M. Engel, A. Lombardo, R. Krupke, A. C. Ferrari, P. Avouris and M. Steiner, *Nano Lett.*, 2013, **13**, 1416–1421.

61 S. Tongay, J. Zhou, C. Ataca, J. Liu, J. S. Kang, T. S. Matthews, L. You, J. Li, J. C. Grossman and J. Wu, *Nano Lett.*, 2013, **13**, 2831–2836.

62 M. Bernardi, M. Palummo and J. C. Grossman, *Nano Lett.*, 2013, **13**, 3664–3670.

63 Y. Tsuboi, F. Wang, D. Kozawa, K. Funahashi, S. Mouri, Y. Miyauchi, T. Takenobu and K. Matsuda, *Nanoscale*, 2015, **7**, 14476–14482.

64 Y. Zhou, W. Xu, Y. Sheng, H. Huang, Q. Zhang, L. Hou, V. Shautsova and J. H. Warner, *ACS Appl. Mater. Interfaces*, 2019, **11**, 2234–2242.

65 J. J. Quinn and K.-S. Yi, *Solid State Physics*, Springer International Publishing, Cham, 2nd edn., 2018.

66 W. Setyawan and S. Curtarolo, *Comput. Mater. Sci.*, 2010, **49**, 299–312.

67 M. FOX, *Optical properties of solids*, Oxford University Press, Oxford, 2nd edn., 2010.

68 T. Cheiwchanchamnangij and W. R. L. Lambrecht, *Phys. Rev. B*, 2012, **85**, 205302.

69 C. Kittel, *Introduction to solid state physics*, John Wiley & Sons, Inc., Hoboken, 8th edn., 2005.

70 S. O. Kasap, *Principles of Electronic Materials & Devices*, McGraw-Hill Education, New York, Fourth., 2018.

71 M. FOX, *Quantum Optics: An Introduction*, Oxford University Press, Oxford, 2006.

72 M. Chhowalla, H. S. Shin, G. Eda, L.-J. Li, K. P. Loh and H. Zhang, *Nat. Chem.*, 2013, **5**, 263–275.

73 B. Radisavljevic, A. Radenovic, J. Brivio, V. Giacometti and A. Kis, *Nat. Nanotechnol.*, 2011, **6**, 147–150.

74 Q. H. Wang, K. Kalantar-Zadeh, A. Kis, J. N. Coleman and M. S. Strano, *Nat. Nanotechnol.*, 2012, **7**, 699–712.

75 A. Splendiani, L. Sun, Y. Zhang, T. Li, J. Kim, C. Y. Chim, G. Galli and F. Wang, *Nano Lett.*, 2010, **10**, 1271–1275.

76 D. Xiao, G. Bin Liu, W. Feng, X. Xu and W. Yao, *Phys. Rev. Lett.*, 2012, **108**, 196802.

77 A. Chernikov, T. C. Berkelbach, H. M. Hill, A. Rigosi, Y. Li, O. B. Aslan, D. R. Reichman, M. S. Hybertsen and T. F. Heinz, *Phys. Rev. Lett.*, 2014, **113**, 076802.

78 C. Lee, H. Yan, L. E. Brus, T. F. Heinz, J. Hone and S. Ryu, *ACS Nano*, 2010, **4**, 2695–2700.

79 Z. Wang, J. Shan and K. F. Mak, *Nat. Nanotechnol.*, 2017, **12**, 144–149.

80 B. W. H. Baugher, H. O. H. Churchill, Y. Yang and P. Jarillo-Herrero, *Nat. Nanotechnol.*, 2014, **9**, 262–267.

81 H. Wang, C. Zhang and F. Rana, *Nano Lett.*, 2015, **15**, 339–345.

82 X.-X. Zhang, Y. You, S. Y. F. Zhao and T. F. Heinz, *Phys. Rev. Lett.*, 2015, **115**, 257403.

83 H. Shi, R. Yan, S. Bertolazzi, J. Brivio, B. Gao, A. Kis, D. Jena, H. G. Xing and L. Huang, *ACS Nano*, 2013, **7**, 1072–1080.

84 H. J. Conley, B. Wang, J. I. Ziegler, R. F. Haglund, S. T. Pantelides and K. I. Bolotin, *Nano Lett.*, 2013, **13**, 3626–3630.

85 H. Li, A. W. Contryman, X. Qian, S. M. Ardakani, Y. Gong, X. Wang, J. M. Weisse, C. H. Lee, J. Zhao, P. M. Ajayan, J. Li, H. C. Manoharan and X. Zheng, *Nat. Commun.*, 2015, **6**, 7381.

86 J. S. Ross, S. Wu, H. Yu, N. J. Ghimire, A. M. Jones, G. Aivazian, J. Yan, D. G. Mandrus, D. Xiao, W. Yao and X. Xu, *Nat. Commun.*, 2013, **4**, 1474.

87 Y. Ye, J. Xiao, H. Wang, Z. Ye, H. Zhu, M. Zhao, Y. Wang, J. Zhao, X. Yin and X. Zhang, *Nat. Nanotechnol.*, 2016, **11**, 598–602.

88 S. Wu, J. S. Ross, G.-B. Liu, G. Aivazian, A. Jones, Z. Fei, W. Zhu, D. Xiao, W. Yao, D. Cobden and X. Xu, *Nat. Phys.*, 2013, **9**, 149–153.

89 H. Yuan, M. S. Bahramy, K. Morimoto, S. Wu, K. Nomura, B. J. Yang, H. Shimotani, R. Suzuki, M. Toh, C. Kloc, X. Xu, R. Arita, N. Nagaosa and Y. Iwasa, *Nat. Phys.*, 2013, **9**, 563–569.

90 J. Lee, K. F. Mak and J. Shan, *Nat. Nanotechnol.*, 2016, **11**, 421–425.

91 Y. Li, J. Ludwig, T. Low, A. Chernikov, X. Cui, G. Arefe, Y. D. Kim, A. M. Van Der Zande, A. Rigosi, H. M. Hill, S. H. Kim, J. Hone, Z. Li, D. Smirnov and T. F. Heinz, *Phys. Rev. Lett.*, 2014, **113**, 266804.

92 J. Choi, H. Y. Zhang, H. D. Du and J. H. Choi, *ACS Appl. Mater. Interfaces*, 2016, **8**, 8864–8869.

93 A. Molina-Sánchez and L. Wirtz, *Phys. Rev. B*, 2011, **84**, 155413.

94 P. Tonndorf, R. Schmidt, P. Böttger, X. Zhang, J. Börner, A. Liebig, M. Albrecht, C. Kloc, O. Gordan, D. R. T. Zahn, S. Michaelis de Vasconcellos and R. Bratschitsch, *Opt. Express*, 2013, **21**, 4908–4916.

95 H. Li, Q. Zhang, C. C. R. Yap, B. K. Tay, T. H. T. Edwin, A. Olivier and D. Baillargeat, *Adv. Funct. Mater.*, 2012, **22**, 1385–1390.

96 B. Chakraborty, H. S. S. R. Matte, A. K. Sood and C. N. R. Rao, *J. Raman Spectrosc.*, 2013, **44**, 92–96.

97 J. Suh, T. E. Park, D. Y. Lin, D. Fu, J. Park, H. J. Jung, Y. Chen, C. Ko, C. Jang, Y. Sun, R. Sinclair, J. Chang, S. Tongay and J. Wu, *Nano Lett.*, 2014, **14**, 6976–6982.

98 H. Nan, Z. Wang, W. Wang, Z. Liang, Y. Lu, Q. Chen, D. He, P. Tan, F. Miao, X. Wang, J. Wang and Z. Ni, *ACS Nano*, 2014, **8**, 5738–5745.

99 S. F. Wang, W. J. Zhao, F. Giustiniano and G. Eda, *Phys. Chem. Chem. Phys.*, 2016, **18**, 4304–4309.

100 D. Kiriya, M. Tosun, P. Zhao, J. S. Kang and A. Javey, *J. Am. Chem. Soc.*, 2014, **136**, 7853–7856.

101 T. L. Atallah, J. Wang, M. Bosch, D. Seo, R. A. Burke, O. Moneer, J. Zhu, M. Theibault, L. E. Brus, J. Hone and X.-Y. Zhu, *J. Phys. Chem. Lett.*, 2017, 2148–2152.

102 B. Liu, L. Chen, G. Liu, A. N. Abbas, M. Fathi and C. Zhou, *ACS Nano*, 2014, **8**, 5304–5314.

103 Y. Homma, S. Chiashi, T. Yamamoto, K. Kono, D. Matsumoto, J. Shitaba and S. Sato, *Phys. Rev. Lett.*, 2013, **110**, 157402.

104 G. Levita, P. Restuccia and M. C. Righi, *Carbon N. Y.*, 2016, **107**, 878–884.

105 W. Zhang, K. Matsuda and Y. Miyauchi, *J. Phys. Chem. C*, 2018, **122**, 13175–13181.

106 A. J. Bard, *ELECTROCHEMICAL METHODS Fundamentals and Applications*, John Wiley & Sons, Inc., New York, 2nd ed., 2000.

107 J. Ristein, M. Riedel and L. Ley, *J. Electrochem. Soc.*, 2004, **151**, E315–E321.

108 V. Chakrapani, J. C. Angus, A. B. Anderson, S. D. Wolter, B. R. Stoner and G. U. Sumanasekera, *Science*, 2007, **318**, 1424–1430.

109 C. M. Aguirre, P. L. Levesque, M. Paillet, F. Lapointe, B. C. St-Antoine, P. Desjardins and R. Martel, *Adv. Mater.*, 2009, **21**, 3087–3091.

110 P. L. Levesque, S. S. Sabri, C. M. Aguirre, J. Guillemette, M. Siaj, P. Desjardins, T. Szkopek and R. Martel, *Nano Lett.*, 2011, **11**, 132–137.

111 P. Atkins and J. de Paula, *Physical Chemistry*, Oxford University Press, New York, 8th edn., 2006.

112 H. L. Zhuang and R. G. Hennig, *Chem. Mater.*, 2013, **25**, 3232–3238.

113 C. Zhang, C. Gong, Y. Nie, K.-A. Min, C. Liang, Y. J. Oh, H. Zhang, W. Wang, S. Hong, L. Colombo, R. M. Wallace and K. Cho, *2D Mater.*, 2016, **4**, 015026.

114 H. Wang, C. Zhang and F. Rana, *Nano Lett.*, 2015, **15**, 339–345.

115 D. Liu, Y. Guo, L. Fang and J. Robertson, *Appl. Phys. Lett.*, 2013, **103**, 183113.

116 S. KC, R. C. Longo, R. Addou, R. M. Wallace and K. Cho, *Nanotechnology*, 2014, **25**, 375703.

117 J. H. Park, A. Sanne, Y. Guo, M. Amani, K. Zhang, H. C. P. Movva, J. A. Robinson, A. Javey, J. Robertson, S. K. Banerjee and A. C. Kummel, *Sci. Adv.*, 2017, **3**, e1701661.

118 K. Sunamura, T. R. Page, K. Yoshida, T. A. Yano and Y. Hayamizu, *J. Mater. Chem. C*, 2016, **4**, 3268–3273.

119 H. M. Oh, G. H. Han, H. Kim, J. J. Bae, M. S. Jeong and Y. H. Lee, *ACS Nano*, 2016, **10**, 5230–5236.

120 M. Yamamoto, S. Dutta, S. Aikawa, S. Nakaharai, K. Wakabayashi, M. S. Fuhrer, K. Ueno and K. Tsukagoshi, *Nano Lett.*, 2015, **15**, 2067–2073.

121 P. Budania, P. Baine, J. Montgomery, C. McGeough, T. Cafolla, M. Modreanu, D. McNeill, N. Mitchell, G. Hughes and P. Hurley, *MRS Commun.*, 2017, **7**, 813–818.

122 B. Radisavljevic, A. Radenovic, J. Brivio, V. Giacometti and A. Kis, *Nat. Nanotechnol.*, 2011, **6**, 147–150.

123 Z. Yin, H. Li, H. Li, L. Jiang, Y. Shi, Y. Sun, G. Lu, Q. Zhang, X. Chen and H. Zhang, *ACS Nano*, 2012, **6**, 74–80.

124 S. Tongay, J. Zhou, C. Ataca, J. Liu, J. S. Kang, T. S. Matthews, L. You, J. Li, J. C. Grossman and J. Wu, *Nano Lett.*, 2013, **13**, 2831–2836.

125 W. Zhang, K. Matsuda and Y. Miyauchi, *ACS Omega*, 2019, **4**, 10322–10327.

126 H. L. Liu, C. C. Shen, S. H. Su, C. L. Hsu, M. Y. Li and L. J. Li, *Appl. Phys. Lett.*, 2014, **105**, 201905.

127 A. Arora, M. Koperski, K. Nogajewski, J. Marcus, C. Faugeras and M. Potemski, *Nanoscale*, 2015, **7**, 10421–10429.

128 S. Chen and L.-W. Wang, *Chem. Mater.*, 2012, **24**, 3659–3666.

129 V. Chakrapani, J. C. Angus, A. B. Anderson, S. D. Wolter, B. R. Stoner and G. U. Sumanasekera, *Science*, 2007, **318**, 1424–1430.

130 T. F. Jaramillo, K. P. Jørgensen, J. Bonde, J. H. Nielsen, S. Horch and I. Chorkendorff, *Science*, 2007, **317**, 100–102.

131 R. K. Joshi, S. Shukla, S. Saxena, G.-H. Lee, V. Sahajwalla and S. Alwarappan, *AIP Adv.*, 2016, **6**, 015315.

132 F. A. Rasmussen, K. S. Thygesen, F. Anselm, K. Sommer, F. A. Rasmussen and K. S. Thygesen, *J. Phys. Chem. C*, 2015, **119**, 13169–13183.

133 K. Fujii, *in Photoelectrochemical Solar Fuel Production*, Eds. S. Giménez and J. Bisquert, Springer International Publishing, 1st edn., 2016.

134 M. Böhmisch, F. Burmeister, J. Boneberg and P. Leiderer, *Appl. Phys. Lett.*, 1996, **69**, 1882–1884.

135 Y. T. Huang, A. Dodda, D. S. Schulman, A. Sebastian, F. Zhang, D. Buzzell, M. Terrones, S. P. Feng and S. Das, *ACS Appl. Mater. Interfaces*, 2017, **9**, 39059–39068.

136 A. Y. S. Eng, A. Ambrosi, Z. Sofer, P. Šimek and M. Pumera, *ACS Nano*, 2014, **8**, 12185–12198.

137 X. Liu, T. Xu, X. Wu, Z. Zhang, J. Yu, H. Qiu, J. H. Hong, C. H. Jin, J. X. Li, X. R. Wang, L. T. Sun and W. Guo, *Nat. Commun.*, 2013, **4**, 1776.

138 J. Nozaki, M. Fukumura, T. Aoki, Y. Maniwa, Y. Yomogida and K. Yanagi, *Sci. Rep.*, 2017, **7**, 46004.

139 Y. Ryu, W. Kim, S. Koo, H. Kang, K. Watanabe, T. Taniguchi and S. Ryu, *Nano Lett.*, 2017, **17**, 7267–7273.

140 S. R. Das, K. Wakabayashi, M. Yamamoto, K. Tsukagoshi and S. Dutta, *J. Phys. Chem. C*, 2018, **122**, 17001–17007.

141 A. K. Singh, L. Zhou, A. Shinde, S. K. Suram, J. H. Montoya, D. Winston, J. M. Gregoire and K. A. Persson, *Chem. Mater.*, 2017, **29**, 10159–10167.

142 T. Cai, S. A. Yang, X. Li, F. Zhang, J. Shi, W. Yao and Q. Niu, *Phys. Rev. B*, 2013, **88**, 115140.

143 A. M. Jones, H. Yu, J. R. Schaibley, J. Yan, D. G. Mandrus, T. Taniguchi, K. Watanabe, H. Dery, W. Yao and X. Xu, *Nat. Phys.*, 2016, **12**, 323–327.

144 M. Manca, M. M. Glazov, C. Robert, F. Cadiz, T. Taniguchi, K. Watanabe, E. Courtade, T. Amand, P. Renucci, X. Marie, G. Wang and B. Urbaszek, *Nat. Commun.*, 2017, **8**, 14927.

145 A. M. Jones, H. Yu, N. J. Ghimire, S. Wu, G. Aivazian, J. S. Ross, B. Zhao, J. Yan, D. G. Mandrus, D. Xiao, W. Yao and X. Xu, *Nat. Nanotechnol.*, 2013, **8**, 634–638.

146 D. Lagarde, L. Bouet, X. Marie, C. R. Zhu, B. L. Liu, T. Amand, P. H. Tan and B. Urbaszek, *Phys. Rev. Lett.*, 2014, **112**, 047401.

147 Z. Li, R. Ye, R. Feng, Y. Kang, X. Zhu, J. M. Tour and Z. Fang, *Adv. Mater.*, 2015, **27**, 5235–5240.

148 S. Konabe, *Appl. Phys. Lett.*, 2016, **109**, 073104.

149 Y. Miyauchi, S. Konabe, F. Wang, W. Zhang, A. Hwang, Y. Hasegawa, L. Zhou, S. Mouri, M. Toh, G. Eda and K. Matsuda, *Nat. Commun.*, 2018, **9**, 2598.

150 K. Shinokita, X. Wang, Y. Miyauchi, K. Watanabe, T. Taniguchi and K. Matsuda, *Adv. Funct. Mater.*, 2019, **29**, 1900260.

151 P. Rivera, K. L. Seyler, H. Yu, J. R. Schaibley, J. Yan, D. G. Mandrus, W. Yao and X. Xu, *Science*, 2016, **351**, 688–691.

152 O. L. Sanchez, D. Ovchinnikov, S. Misra, A. Allain and A. Kis, *Nano Lett.*, 2016, **16**, 5792–5797.

153 D. Zhong, K. L. Seyler, X. Linpeng, R. Cheng, N. Sivadas, B. Huang, E. Schmidgall, T. Taniguchi, K. Watanabe, M. A. McGuire, W. Yao, D. Xiao, K.-M. C. Fu and X. Xu, *Sci. Adv.*, 2017, **3**, e1603113.

154 W.-T. Hsu, L.-S. Lu, P.-H. Wu, M.-H. Lee, P.-J. Chen, P.-Y. Wu, Y.-C. Chou, H.-T. Jeng, L.-J. Li, M.-W. Chu and W.-H. Chang, *Nat. Commun.*, 2018, **9**, 1356.

155 C. Mai, A. Barrette, Y. Yu, Y. G. Semenov, K. W. Kim, L. Cao and K. Gundogdu, *Nano Lett.*, 2014, **14**, 202–206.

156 C. Mai, Y. G. Semenov, A. Barrette, Y. Yu, Z. Jin, L. Cao, K. W. Kim and K. Gundogdu, *Phys. Rev. B*, 2014, **90**, 041414.

157 C. R. Zhu, K. Zhang, M. Glazov, B. Urbaszek, T. Amand, Z. W. Ji, B. L. Liu and X. Marie, *Phys. Rev. B*, 2014, **90**, 161302.

158 A. Singh, K. Tran, M. Kolarczik, J. Seifert, Y. Wang, K. Hao, D. Pleskot, N. M. Gabor, S. Helmrich, N. Owschimikow, U. Woggon and X. Li, *Phys. Rev. Lett.*, 2016, **117**, 257402.

159 G. Wang, L. Bouet, D. Lagarde, M. Vidal, A. Balocchi, T. Amand, X. Marie and B. Urbaszek, *Phys. Rev. B*, 2014, **90**, 075413.

160 K. Shinokita, X. Wang, Y. Miyauchi, K. Watanabe, T. Taniguchi, S. Konabe and K. Matsuda, *Phys. Rev. B*, 2019, **99**, 245307.

161 Y. Hoshi, T. Kuroda, M. Okada, R. Moriya, S. Masubuchi, K. Watanabe, T. Taniguchi, R. Kitaura and T. Machida, *Phys. Rev. B*, 2017, **95**, 241403.

162 X. Zhang, F. Zhang, Y. Wang, D. S. Schulman, T. Zhang, A. Bansal, N. Alem, S. Das, V. H. Crespi, M. Terrones and J. M. Redwing, *ACS Nano*, 2019, **13**, 3341–3352.

163 P. Rivera, J. R. Schaibley, A. M. Jones, J. S. Ross, S. Wu, G. Aivazian, P. Klement, K. Seyler, G. Clark, N. J. Ghimire, J. Yan, D. G. Mandrus, W. Yao and X. Xu, *Nat. Commun.*, 2015, **6**, 6242.

164 J. Kim, C. Jin, B. Chen, H. Cai, T. Zhao, P. Lee, S. Kahn, K. Watanabe, T. Taniguchi, S. Tongay, M. F. Crommie and F. Wang, *Sci. Adv.*, 2017, **3**, e1700518.

165 Z. Hu, Z. Wu, C. Han, J. He, Z. Ni and W. Chen, *Chem. Soc. Rev.*, 2018, **47**, 3100–3128.

166 J. Wierzbowski, J. Klein, F. Sigger, C. Straubinger, M. Kremser, T. Taniguchi, K. Watanabe, U. Wurstbauer, A. W. Holleitner, M. Kaniber, K. Müller and J. J. Finley, *Sci. Rep.*, 2017, **7**, 12383.

167 A. Castellanos-Gomez, R. Roldán, E. Cappelluti, M. Buscema, F. Guinea, H. S. J. Van Der Zant and G. A. Steele, *Nano Lett.*, 2013, **13**, 5361–5366.

168 C. R. Zhu, G. Wang, B. L. Liu, X. Marie, X. F. Qiao, X. Zhang, X. X. Wu, H. Fan, P. H. Tan, T. Amand and B. Urbaszek, *Phys. Rev. B*, 2013, **88**, 121301.

169 N. D. Kay, B. J. Robinson, V. I. Fal'Ko, K. S. Novoselov and O. V. Kolosov, *Nano Lett.*, 2014, **14**, 3400–3404.

170 M. Buscema, G. A. Steele, H. S. J. van der Zant and A. Castellanos-Gomez, *Nano Res.*, 2014, **7**, 561–571.

171 Y. Kwon, K. Kim, W. Kim, S. Ryu and H. Cheong, *Curr. Appl. Phys.*, 2018, **18**, 941–945.

172 T. Cao, G. Wang, W. Han, H. Ye, C. Zhu, J. Shi, Q. Niu, P. Tan, E. Wang, B. Liu and J. Feng, *Nat. Commun.*, 2012, **3**, 887.

173 L. Yang, N. a. Sinitsyn, W. Chen, J. Yuan, J. Zhang, J. Lou and S. a. Crooker, *Nat. Phys.*, 2015, **11**, 830–835.

174 G. Plechinger, P. Nagler, A. Arora, R. Schmidt, A. Chernikov, A. G. Del Águila, P. C. M. Christianen, R. Bratschitsch, C. Schüller and T. Korn, *Nat. Commun.*, 2016, **7**, 12715.

175 B. T. Jonker and R. K. Kawakami, *2D Mater.*, 2018, **5**, 0110110.

176 Y. Li, C.-Y. Xu, J.-K. Qin, W. Feng, J.-Y. Wang, S. Zhang, L.-P. Ma, J. Cao, P. A. Hu, W. Ren and L. Zhen, *Adv. Funct. Mater.*, 2016, **26**, 293–302.

177 N. B. Mohamed, F. Wang, H. E. Lim, W. Zhang, S. Koirala, S. Mouri, Y. Miyauchi and K. Matsuda, *Phys. Status Solidi Basic Res.*, , DOI:10.1002/pssb.201600563.

178 J. D. Wood, S. A. Wells, D. Jariwala, K. S. Chen, E. Cho, V. K. Sangwan, X. Liu, L. J. Lauhon, T. J. Marks and M. C. Hersam, *Nano Lett.*, 2014, **14**, 6964–6970.

179 A. Avsar, I. J. Vera-Marun, J. Y. Tan, K. Watanabe, T. Taniguchi, A. H. Castro Neto and B. Özyilmaz, *ACS Nano*, 2015, **9**, 4138–4145.

180 L. Viti, J. Hu, D. Coquillat, A. Politano, C. Consejo, W. Knap and M. S. Vitiello, *Adv. Mater.*, 2016, **28**, 7390–7396.

181 F. Cadiz, E. Courtade, C. Robert, G. Wang, Y. Shen, H. Cai, T. Taniguchi, K. Watanabe, H. Carrere, D. Lagarde, M. Manca, T. Amand, P. Renucci, S. Tongay, X. Marie and B. Urbaszek, *Phys. Rev. X*, 2017, **7**, 021026.

Scientific Contributions

The name of the author is bold and underlined.

Peer Reviewed Articles

1. **W. Zhang**, et al. Bright and highly valley polarized trions in chemically treated monolayer MoS_2. To be published.
2. **W. Zhang**, K. Matsuda, and Y. Miyauchi, Photostability of Monolayer Transition-Metal Dichalcogenides in Ambient Air and Acidic/Basic Aqueous Solutions. ACS Omega 4.6 (2019): 10322-10327.
3. **W. Zhang**, K. Matsuda, and Y. Miyauchi, pH-Dependent photoluminescence properties of monolayer transition-metal dichalcogenides immersed in an aqueous solution. J. Phys. Chem. C 122.24 (2018): 13175-13181.
4. D. Tan, X. Wang, **W. Zhang**, H. E. Lim, K. Shinokita, Y. Miyauchi, M. Maruyama, S. Okada, and K. Matsuda, Carrier transport and photoresponse in GeSe/MoS_2 heterojunction p-n diodes. Small 14, (2018): 1704559.
5. Y. Miyauchi, S. Konabe, F. Wang, **W. Zhang,** A. Hwang, Y. Hasegawa, L. Zhou, S. Mouri, M. Toh, G. Eda and K. Matsuda, Evidence for line width and carrier screening effects on excitonic valley relaxation in 2D semiconductors. Nature communications 9.1 (2018): 2598.
6. D. Tan, **W. Zhang**, X. Wang, K. Sandhaya, Y. Miyauchi, and K. Matsuda, Polarization-sensitive and broadband germanium sulfide photodetectors with excellent high-temperature performance. Nanoscale 9.34 (2017): 12425-12431.
7. S. Mouri, **W. Zhang**, D. Kozawa, Y. Miyauchi, G. Eda and K. Matsuda, Thermal dissociation of inter-layer excitons in MoS_2/$MoSe_2$ hetero-bilayers. Nanoscale 9.20 (2017): 6674-6679.
8. D. Tan, H. En Lim, N. Baizura Mohamed, S. Mouri, S. Koirala, **W. Zhang,** Y. Miyauchi, M. Ohfuchi, and K. Matsuda, Anisotropic optical and electronic properties of two-dimensional layered germanium sulfide. Nano Research 10.2 (2017): 546-555.

Conference Presentations

International Conferences

1. **Wenjin Zhang**, Yuhei Miyauchi, and Kazunari Matsuda, "Photoluminescence properties of monolayer monolayer transition metal dichalcogenides in an aqueous solution". *Graphene Korea 2019.* (Oral).
2. **Wenjin Zhang**, Yuhei Miyauchi, and Kazunari Matsuda, "Optical properties of monolayer MoS_2 in an aqueous solution". *APS March 2018.* (Oral).

Domestic Conferences

1. **Wenjin Zhang**, Yuhei Miyauchi, and Kazunari Matsuda, "Stability of monolayer WSe_2 and MoS_2 in an aqueous solution under light irradiation". *The 66th Japan Society Applied Physics (JSAP) Spring Meeting, 2019* (Oral).
2. **Wenjin Zhang**, Yuhei Miyauchi, and Kazunari Matsuda, "pH-dependent photoluminescence of monolayer transition-metal dichalcogenides in an aqueous solution". *55th Fullerences-Nanotubes-Graphene General Symposium (FNTG),* 2018 (Oral).
3. **Wenjin Zhang**, Alexander Hwang, Tetsuki Saito, Yu Kobayashi, Takashi Taniguchi, Kenji Watanabe, Yasumitsu Miyata, Kazunari Matsuda, and Yuhei Miyauchi, "Substrate and sample dependent exciton transport properties in monolayer transition metal dichalcogenides". *53rd Fullerences-Nanotubes-Graphene General Symposium (FNTG),* 2017 (Poster).
4. **Wenjin Zhang**, Yuhei Miyauchi, and Kazunari Matsuda, "Optical properties of transition metal dichalcogenide monolayers under carrier density modulation".*14th optical matter science discussion group,* 2017 (Oral).
5. **Wenjin Zhang**, Yusuke Hasegawa, Kazunari Matsuda, and Yuhei Miyauchi, "Optical spectroscopy on monolayer transition metal dichalcogenides immersed in an aqueous solution". *52th Fullerences-Nanotubes-Graphene General Symposium (FNTG),* 2017 (Poster).
6. **Wenjin Zhang**, Yusuke Hasegawa, Shinichiro Mouri, Kazunari Matsuda, and Yuhei Miyauchi, "Plarization-resolved photoluminescence spectroscopy on monolayer

transition metal dichalcogenides under electrostatic gating". *51th Fullerences-Nanotubes-Graphene General Symposium (FNTG)*, 2016 (Poster).